MEASUREMENT OF THE $t\bar{t}$, WW AND $Z \to \tau\tau$ PRODUCTION CROSS SECTIONS IN $p\bar{p}$ COLLISIONS AT $\sqrt{s} = 1.96$ TeV

by

Sebastian Carron Montero

Department of Physics
Duke University

Date: _____

Approved:

_____
Mark Kruse, Supervisor

_____
Alfred Goshaw

_____
Calvin Howell

_____
Roxanne Springer

_____
John Thomas

Dissertation submitted in partial fulfillment of the
requirements for the degree of Doctor of Philosophy
in the Department of Physics
in the Graduate School of
Duke University

2006

ABSTRACT

(Physics)

MEASUREMENT OF THE $t\bar{t}$, WW AND $Z \to \tau\tau$ PRODUCTION CROSS SECTIONS IN $p\bar{p}$ COLLISIONS AT $\sqrt{s} = 1.96$ TeV

by

Sebastian Carron Montero

Department of Physics
Duke University

Date: _____

Approved:

_____
Mark Kruse, Supervisor

_____
Alfred Goshaw

_____
Calvin Howell

_____
Roxanne Springer

_____
John Thomas

An abstract of a dissertation submitted in partial fulfillment of the requirements for the degree of Doctor of Philosophy in the Department of Physics in the Graduate School of Duke University

2006

Abstract

In this thesis we present a new technique to analyze events containing two highly energetic leptons, as a probe of the Standard Model. The philosophy is to consider the data in a more global way, as opposed to the more traditional process dependent approach of extracting a given signal over the expected backgrounds by using various kinematical requirements. We use our global technique to simultaneously measure the cross sections of the main Standard Model processes; the $t\bar{t}$, WW and $Z \rightarrow \tau\tau$ production from $p\bar{p}$ collisions at $\sqrt{s}$ =1.96 TeV in the CDF detector at Fermilab.

We select events by requiring they contain two highly energetic leptons ($e\mu$, ee, or $\mu\mu$), and make no other kinematic requirements, except for the ee and $\mu\mu$ channels. We then use a likelihood fit of the data in the two-dimensional phase space defined by the missing transverse energy ($\not\!\!E_T$) and the number of jets in the event (N_{jet}), to the expected Standard Model distributions, to simultaneously extract the production cross-sections of the main process contributing to our dilepton sample. Our results, using about 360 pb^{-1} of data, are:

$$\begin{aligned}
\sigma(p\bar{p} \rightarrow t\bar{t}) &= 8.5^{+2.6}_{-2.2}(fit)^{+0.7}_{-0.3}(shape) \text{ pb} \\
\sigma(p\bar{p} \rightarrow WW) &= 16.3^{-4.4}_{+5.1}(fit)^{0.8}_{-0.2}(shape) \text{ pb} \\
\sigma(p\bar{p} \rightarrow Z \rightarrow \tau\tau) &= 291.4^{+49.5}_{-46.0}(fit)^{+5.8}_{-2.9}(shape) \text{ pb}
\end{aligned}$$

where the first error comes from the likelihood fit and includes the statistical error, all acceptance systematic errors, and the uncertainty in the integrated luminosity, and the second error is from systematic uncertainties associated with the modelling of the $\not\!\!E_T$-N_{jet} distribution. By requiring a minimum of selection criteria we are optimally using the statistical power of the data for given lepton definitions. We used this global method to successfully extract cross-section measurements.

To my wife, Rafaela.

When it was proclaimed that the Library contained all books, the first impression was one of extravagant happiness. All men felt themselves to be the masters of an intact and secret treasure. There was no personal or world problem whose eloquent solution did not exist in some hexagon...As was natural, this inordinate hope was followed by an excessive depression. The certitude that some shelf in some hexagon held precious books and that these precious books were inaccessible seemed almost intolerable.

"The Library of Babel" (1941) Jorge Luis Borges.

Contents

Abstract **iv**

List of Tables **xi**

List of Figures **xvi**

Acknowledgements **xxi**

1 Introduction **1**

1.1 Analysis Overview 1

1.2 The Standard Model 4

1.2.1 Leptons 5

1.2.2 Quarks 10

1.2.3 Gauge Bosons 12

1.2.4 Hadronization of High Energy Quarks and Gluons 13

1.2.5 The Standard Model Lagrangian Formulation 15

2 High Momentum Dilepton Physics at the Tevatron **24**

2.1 Parton Distribution Functions (PDF) in Hadron Colliders 24

2.2 Standard Model Phenomenology 25

2.2.1 The $t\bar{t}$ Production and Decay 26

2.2.2 The WW Production and Decay 31

2.2.3 Drell-Yan Processes 34

2.3 Experimental Cross Section Results to Date 36

3 The Experimental Setup **39**

3.1 The Fermilab Tevatron 39

3.1.1 The Proton Source . . . 40
3.1.2 The Main Injector . . . 41
3.1.3 The Anti Proton Source . . . 42
3.1.4 The Tevatron . . . 43
3.1.5 Measuring The Luminosity . . . 44
3.2 The CDF Run II Detector . . . 45
3.2.1 Geometrical Coordinate System . . . 46
3.2.2 The Tracking System . . . 48
3.2.3 Calorimetry . . . 55
3.2.4 The Muon Detection System . . . 60
3.3 Trigger and Data Taking . . . 62
3.3.1 Level 1 . . . 62
3.3.2 Level 2 . . . 63
3.3.3 Level 3 . . . 63
3.3.4 Offline Data Processing and Datasets . . . 63
3.4 The Detector Simulation . . . 65

4 Particle Identification **66**

4.1 The Particle Traces in the Detector . . . 66
4.2 Central Electron Identification . . . 67
4.3 Forward Electron Identification . . . 70
4.4 Muon Identification . . . 72
4.5 What About τ Identification? . . . 74
4.6 Hadronic Jets . . . 75
4.7 Neutrinos (Missing Transverse Energy) . . . 76

4.8 Variable Corrections 77
4.8.1 Jet Corrections 77
4.8.2 Missing Transverse Energy ($\not\!\!E_T$) Correction 79
4.9 The Cosmic Event Filter 79
4.10 The Conversion Electron Filter 80

5 Analysis Strategy **81**
5.1 Motivation and Analysis Introduction 81
5.2 Event Selection 85
5.2.1 Dilepton Categories 85
5.2.2 The Missing Energy Significance 86
5.2.3 Event Triggers 87

6 Global Method for Measuring Standard Model Cross Section **89**
6.1 Monte Carlo Simulated Datasets 89
6.2 Signal Acceptances 90
6.2.1 Scale Factors 91
6.2.2 Signal Acceptance Table 91
6.3 Background Expectations 93
6.4 The Fake Lepton Background 93
6.4.1 The Fake Rate Estimation Methodology. 93
6.4.2 The Fake Rate Probabilities 96
6.4.3 Applying the Fake Rates to the W+jets Fakeable Data 99
6.4.4 Fake Background Expectation and $\not\!\!E_T$-N_{jet} Phase Space Templates 103
6.5 Systematic Uncertainties 106

6.5.1 The Signal Acceptance Systematic Uncertanties. 106
6.5.2 Background Systematic Uncertainties 114
6.6 The Data Events and Grand Summary of the Standard Model Expectations 117
6.6.1 Grand Summary Table 119
6.6.2 $\not\!\!E_T$ vs N_{jet} Jets Distributions 120
6.7 Fitting Technique 120
6.7.1 Extracting the $t\bar{t}$ and WW Cross Sections from the eμ Data . 127
6.7.2 Pseudo Experiments in the $e\mu$ Final State Channel 128
6.7.3 Extracting the $Z \rightarrow \tau\tau$ Cross Section from the $e\mu$ Data Fit . . 133
6.7.4 Extracting the $t\bar{t}$ and WW Cross Sections from the ee+$\mu\mu$+$e\mu$ Data Fit 135
6.7.5 Pseudo Experiments in the $ee + e\mu + \mu\mu$ Fit 137
6.8 Shape Systematic Errors 138
6.8.1 The $e\mu$ Fit Shape Systematics 141
6.8.2 Shape Systematic Errors Summary. 148

7 Cross Section Results **149**

7.1 Fit Cross Section Results 149
7.2 Data Fit Contour Plots 149

8 Conclusions **152**

A WW production anomalous coupling interaction Lagrangian **154**

B Kinematic Distributions of the CDF 2 Data - 360 pb^{-1} **156**

C Missing Energy vs Number of Jets for CDF 2 Data - 360 pb^{-1} **165**

D Detailed Acceptance Tables **169**

Bibliography **177**

Biography **183**

List of Tables

1.1 The three generations of Standard Model fundamental fermions . . . 4

1.2 The Standard Model fundamental interactions 5

1.3 The lepton masses. The neutrino masses limits are from direct measurements, and exclude neutrino flavor mixing experiments. 8

1.4 The quarks and their masses. 11

2.1 The $t\bar{t}$ decay modes and branching ratios. 31

2.2 The Z^0 decay experimental branching ratios. 36

2.3 Some of the published $t\bar{t}$ production cross section results. 37

2.4 Some of the published WW production cross section results. . . . 38

3.1 Datasets used in this thesis project. 64

4.1 Baseline cuts for central high-P_T isolated electrons ($E_T > 20$ GeV) (CEM). 70

4.2 Baseline cuts for plug isolated electrons (PHX). 72

4.3 Baseline cuts for minimum ionizing isolated track. After passing these cuts the muon is classified as *CMUP*, *CMX* or *non-triggering* according to the definitions in the text. 74

5.1 Event selection cuts 85

5.2 Dilepton categories included in the current analysis. Shown in bold are the triggerable leptons in the data samples studied. Both lepton legs are required to be isolated. 86

5.3 $ELECTRON\_CENTRAL\_18$ trigger requirements 88

5.4 $MUON\_CMUP18$ and $MUON\_CMX18$ trigger requirements . . . 88

6.1 Monte Carlo datasets used for AIDA analysis. 90

6.2 Summary of trigger efficiencies. The CEM_18 trigger efficiency is run-dependent, number given above being an average over η. 91

6.3 Summary of lepton data/MC scale factors. 92

6.4 PHX charge mis-identification scale factors. 92

6.5 Signal acceptances (%) and expected number of events. 92

6.6 Standard Model background expected number of events in $\sim 360\,\mathrm{pb}^{-1}$ 93

6.7 The jet datasets and trigger requirement used for the lepton fake rate. 94

6.8 The CEM denominator cuts 94

6.9 The PHX denominator cuts 95

6.10 The muon denominator cuts 95

6.11 The CEM individual and weighted fake rates, with Z and W subtraction. 97

6.12 The PHX individual and weighted fake rates, with Z and W subtraction. 97

6.13 The CMUP individual and weighted fake rates, with Z and W subtraction. 97

6.14 The CMX individual and weighted fake rates, with Z and W subtraction. 98

6.15 The CMU individual and weighted fake rates, with Z and W subtraction. 98

6.16 The CMP individual and weighted fake rates, with Z and W subtraction. 98

6.17 The CMIO individual and weighted fake rates, with Z and W subtraction. 98

6.18 The samples used for extracting W+jets fakeable events. 99

6.19 The estimated fake lepton background by dilepton category, after each analysis cut. The errors shown are statistical only. Systematic errors are 100% of the expected values. 104

6.20 The Jet Energy Scale signal acceptance systematic error. The first number is the fractional variation in acceptance and the second the statistical error. 108

6.21 The initial state radiation systematic errors. The numbers are the percentile variation due to the addition and substraction of ISR, the error is statistical. 109

6.22 The final state radiation systematic errors. The numbers are the percentile variation due to the addition and substraction of FSR, the error is statistical. 109

6.23 The $t\bar{t}$ generator systematic errors. The values are the acceptances, the errors are statistical. 110

6.24 The $t\bar{t}$ multiple interaction systematic errors. The variations are in acceptance, the errors statistical. 111

6.25 The $Z \to \tau\tau$ multiple interaction systematic errors. Values represent number of expected events just before applying the $\not\!\!E_T$ significance cut. 112

6.26 The lepton scale factor systematic errors. Includes lepton ID, trigger efficiency, PHX charge miss-identification scale factors and Monte Carlo reconstruction scale factors. 112

6.27 Signal acceptance systematic summary. Note some errors are asymmetric, which result in an asymmetric total, however, we used the largest error (symmetrized) in our fit. 114

6.28 Systematic and statistical errors on the fixed backgrounds and the integrated luminosity. 116

6.29 Integrated luminosities of the different dilepton categories used in the analysis. 118

6.30 Number of events in about $360\,\mathrm{pb}^{-1}$ of Run II data, after the requirement of 2 opposite-sign isolated high-P_T leptons. The ee and $\mu\mu$ channels have an additional $\not\!\!E_T^{sig}$ requirement. 119

6.31 Grand summary of expected and observed numbers of events in $\sim 360\,\mathrm{pb}^{-1}$ of data 120

6.32 Minimization steps used in the fit. 126

6.33 Gaussian parameters of fit to pull distributions in the $e\mu$ pseudo experiments 133

6.34 Gaussian parameters of fit to pull distributions in the $ee + e\mu + \mu\mu$ pseudo experiments 138

6.35 The $t\bar{t}$ jet energy scale systematic error for the $e\mu$ fit 144

6.36 The WW jet energy scale systematic error for the $e\mu$ fit 144

6.37 The $Z \rightarrow \tau\tau$ jet energy scale systematic error for the $e\mu$ fit. The correction factor for Z$\rightarrow \tau\tau$ has not been applied yet for this table . . 144

6.38 The $t\bar{t}$ ISR systematic error for the $e\mu$ fit 146

6.39 The WW FSR error for the $e\mu$ fit 146

6.40 The $t\bar{t}$ FSR systematic error for the $e\mu$ fit 147

6.41 The shape systematic errors summary on the $e\mu$ and full fit. 148

7.1 The final results for the Standard Model cross sections measured with 360 pb^{-1} are shown. By *fit* we mean the error returned by the fit, which includes the statistical, acceptance systematic and error on the luminosity; *shape* refers to the template distribution shape systematic uncertainty. 150

D.1 Expected number of events breakdown for $t\bar{t}$, for each dilepton subcategory after each of the analysis cuts. The sample dataset ID is *ttopel*. 170

D.2 Expected number of events breakdown for WW for each dilepton subcategory after each of the analysis cuts. The sample dataset id is *wewk5d*. 171

D.3 Expected number of events breakdown for $Z \rightarrow \tau\tau$ for each dilepton subcategory after each analysis cut. The sample dataset ids are *ztop4i* and *ztop5i*, merged. 172

D.4 Expected number of events breakdown for $Z \rightarrow \mu\mu$ for each dilepton subcategory after each analysis cut. The sample dataset id is *zewk6m* 173

D.5 Expected number of events breakdown for $Z \rightarrow ee$ for each dilepton subcategory after each analysis cut. The sample dataset id is *zewk6d* 174

D.6 Expected number of events breakdown for WZ for each dilepton subcategory after each analysis cut. The sample dataset id is *wtop1z* . . 175

D.7 Expected number of events breakdown for ZZ for each dilepton subcategory after each analysis cut. The sample dataset id is *ztopcz* . . . 176

List of Figures

1.1 From the Run I $t\bar{t}$ dilepton analysis. Azimuthal angle between the $\not\!\!E_T$ and the nearest lepton or jet versus the $\not\!\!E_T$. The 10 candidate events and the $t\bar{t}$ Monte Carlo with $m_t = 175$ GeV are plotted. The 10 dilepton candidates are indicated by the larger symbols. The dashed lines represent the $\not\!\!E_T$ cuts. 2

1.2 The Standard Model Fundamental Particles. 14

2.1 The $t\bar{t}$ production leading-order Feynman diagrams. 27

2.2 Some NLO corrections to $\sigma_{t\bar{t}}$. 28

2.3 Feynman diagram for $t\bar{t}$ production followed by Standard Model decay. 30

2.4 Leading order WW production at the Tevatron. 32

2.5 Trilinear gauge couplings in electroweak theory. 32

2.6 Some next to leading order corrections to the WW production process, including initial state radiation and radiative corrections. 33

2.7 Leading order Z^0 production process, with the Z decaying to electron or muon pairs. 34

2.8 Some next to leading order (NLO) diagrams in the Z^0 production process. 35

2.9 The summary and world average of $t\bar{t}$ production cross sections. . . 37

2.10 The $t\bar{t}$ CDF production combined cross section as a function of $\sqrt{s}$. . 38

3.1 Schematic of accelerator components at Fermilab. Shown also are the locations of the main collider experiments, CDF and D0. 40

3.2 Total delivered and recorded luminosity at CDF, up until January 2006 45

3.3 A cut-away view of the CDF detector. Only half the calorimeters and muon detectors are shown. 46

3.4 CDF Coordinate System. 47

3.5 General Layout of the tracking volumes. 49

3.6 End view of the silicon tracking system. 50

3.7 End view of the layer and superlayers in the Central Outer Tracker. . 53

3.8 End view of the individual cell layout, of the Central Outer Tracker. . 54

3.9 Schematic view of a Central Calorimeter Wedge 57

3.10 Schematic side view of the Plug Calorimeter 59

3.11 The $\eta - \phi$ view of the components of the muon detection system. . . 60

4.1 Schematic of how different particles look like in the detector 67

5.1 Schematic of the Standard Model contributions in the $\not\!\!E_T$ vs. number of jets phase space. 84

6.1 The CEM (left) and PHX (right) fake ratios. 99

6.2 The CMUP (left) and CMU (right) fake ratios. 100

6.3 The CMP (top left), CMIO (bottom left) and CMX (bottom right) fake ratios. 101

6.4 The ee invariant mass from the fake background. We use the "true" lepton from a W decay and the "fake" lepton. 102

6.5 The $e\mu$ invariant mass from the fake background. We use the "true" lepton from a W decay and the "fake" lepton. 102

6.6 The $\mu\mu$ invariant mass from the fake background. We use the "true" lepton from a W decay and the "fake" lepton. 103

6.7 The ee fake background template. 104

6.8 The $e\mu$ fake background template. 105

6.9 The $\mu\mu$ fake background template. 105

6.10 Missing energy significance from varying the jet energy scale by $\pm 1\ \sigma$, for $t\bar{t}$ and WW. 108

6.11 The ee and $\mu\mu$ met significance inside the Z^0 window. The WW, $t\bar{t}$ and $Z \to \tau\tau$ contributions were subtracted from the data. 115

6.12 The ee and $\mu\mu$ ratio of the Monte Carlo to data $\not\!\!E_T$ significance cut efficiency as a function of the cut value 117

6.13 The ee 2-D $\not\!\!E_T$-N_{jet} distributions for the SM "signal" sources, "background" sources (summed together) and from 360 pb^{-1} of data. . . . 121

6.14 The $\mu\mu$ 2-D $\not\!\!E_T$-N_{jet} distributions for the SM "signal" sources, "background" sources (summed together) and from 360 pb^{-1} of data. . . . 122

6.15 The $e\mu$ 2-D $\not\!\!E_T$-N_{jet} distributions for the SM "signal" sources, "background" sources (summed together) and from 360 pb^{-1} of data. . . . 123

6.16 Fitted cross sections,the asymmetric errors and the pull distribution for $t\bar{t}$, from 10000 pseudo-experiments in the $e\mu$ channel, for 360 pb^{-1}, assuming totally correlated errors. 130

6.17 Fitted cross sections,the asymmetric errors and the pull distribution for WW, from 10000 pseudo-experiments in the $e\mu$ channel, for 360 pb^{-1}, assuming totally correlated errors. 131

6.18 Fitted cross sections,the asymmetric errors and the pull distribution for $Z \to \tau\tau$, from 10000 pseudo-experiments in the $e\mu$ channel, for 360 pb^{-1}, assuming totally correlated errors. 132

6.19 Likelihood values from 10000 pseudo-experiments in the $e\mu$ channel, for 360 pb^{-1}, assuming totally correlated errors. The red line shows the likelihood value for the data fit. 133

6.20 $M_{\tau\tau}$ invariant mass distribution, at the generator level, for events passing all the cuts, in eμ channel. 136

6.21 Fitted cross sections,the asymmetric errors and the pull distribution for $t\bar{t}$, from 10000 pseudo-experiments with the full fit, for 360 pb^{-1}, assuming totally correlated errors. 139

6.22 Fitted cross sections,the asymmetric errors and the pull distribution for WW, from 10000 pseudo-experiments with the full fit, for 360 pb^{-1}, assuming totally correlated errors. 140

6.23 Likelihood values from 10000 pseudo-experiments with the full fit, for 360 pb^{-1}, assuming totally correlated errors. The red line shows the likelihood value for the data fit. 141

6.24 Fitted cross sections,the asymmetric errors and the pull distribution for $t\bar{t}$, from 10000 pseudo-experiments with the full fit, for 3600pb^{-1}, assuming totally correlated errors. 142

6.25 Fitted cross sections,the asymmetric errors and the pull distribution for WW, from 10000 pseudo-experiments with the full fit, for 3600 pb^{-1}, assuming totally correlated errors. 143

6.26 Example of variation due to jet energy scale on the $e\mu$ fit $t\bar{t}$ and WW cross sections 145

6.27 Example of variation due to ISR on $e\mu$ fit cross sections 147

6.28 Example of variation due to FSR on $e\mu$ fit cross sections 148

7.1 The two dimensional data 1σ cross section contours from the $e\mu$ fit (a, b and c), and from the $ee + e\mu + \mu\mu$ fit (d). 151

B.1 The number of jets for ee, $e\mu$ and $\mu\mu$ channels. 157

B.2 The missing energy for ee, $e\mu$ and $\mu\mu$ channels. 158

B.3 The missing energy for 0 jet events, for ee, $e\mu$ and $\mu\mu$ channels. . . . 159

B.4 The missing energy for 1 jet events, for ee, $e\mu$ and $\mu\mu$ channels. . . . 160

B.5 The missing energy for 2 jet events, for ee, $e\mu$ and $\mu\mu$ channels. . . . 161

B.6 The invariant mass for ee, $e\mu$ and $\mu\mu$ channels. 162

B.7 The lepton transverse momentum for electrons and muons. 163

B.8 The leptons ϕ and η distributions, for electrons and muons. 164

C.1 The missing energy vs number of jets for ee channel. 166

C.2 The missing energy vs number of jets for $e\mu$ channel. 167

C.3 The missing energy vs number of jets for $\mu\mu$ channel. 168

Acknowledgements

First and foremost I want to acknowledge my wife, Rafaela, who has given me support and encouragement through this journey, but most of all has endured my long years of study from undergraduate years until now. Without her, it would not have been possible to reach this goal, I thank her immensely. I want to thank my parents, and the thanks extend to the rest of my family, but especially to my father, Juan Maria, for inciting in me the desire to search for knowledge since my early years. It was he who gave me my first book on science, and encouraged my early interest, in spite of the fact of himself being from the humanities fields. My parents have provided unending support for following a scientific career when in my native country, Paraguay, such ambitions could be considered even laughable, I will forever be in debt. I would also like to thank all of the great teachers I have had since my years in Paraguay, to my undergraduate years at the University of Sao Paulo, Brazil and finally at Duke University. I have also received help from many collaborators at the CDF experiment at Fermilab. Finally I want to acknowledge the guidance provided by my graduate advisor, Mark Kruse, which made possible the completion of this thesis.

Chapter 1

Introduction

In this chapter we introduce the main objectives of our analysis research project. We also take some time to give a basic overview of the Standard Model, particularly the aspects that are relevant to the processes we study.

1.1 Analysis Overview

In this thesis we study high momentum dilepton final state phenomena, with data collected in the CDF (Collider Detector at Fermilab) detector from $p\bar{p}$ collisions at 1.96 TeV center-of-mass energy in the Tevatron collider at Fermilab. We discuss the Tevatron and the CDF detector in Chapter 3. The current configuration of the detector and data taking period is known as "Run II". In Run I (1992-1996), the discovery of the top quark took place in 1995, which included a measurement of the $p + \bar{p} \rightarrow t + \bar{t} \rightarrow W^+bW^-\bar{b} \rightarrow \ell\ell\nu\nu b\bar{b}$ production cross section using events with two leptons in the final state (called the dilepton decay channel) [1], that used the 109.4 ± 7.2 pb^{-1} of Run I integrated luminosity. In Figure 1.1 we show the Run I data events after the $t\bar{t}$ selection for the dilepton decay channel (events lying inside the "L" shape are cut in the selection process),

In the Run I dilepton $t\bar{t}$ candidates, there were a few $e\mu$ events that had an unusually high missing energy, which is generally associated with neutrinos in Standard Model processes. This was interpreted by some as being a possible indication of new physics [2], and was one of the original motivations behind the current analysis. Events comprising of two final state leptons could provide a rich probing ground for new physics, because the Standard Model contributions are relatively well un-

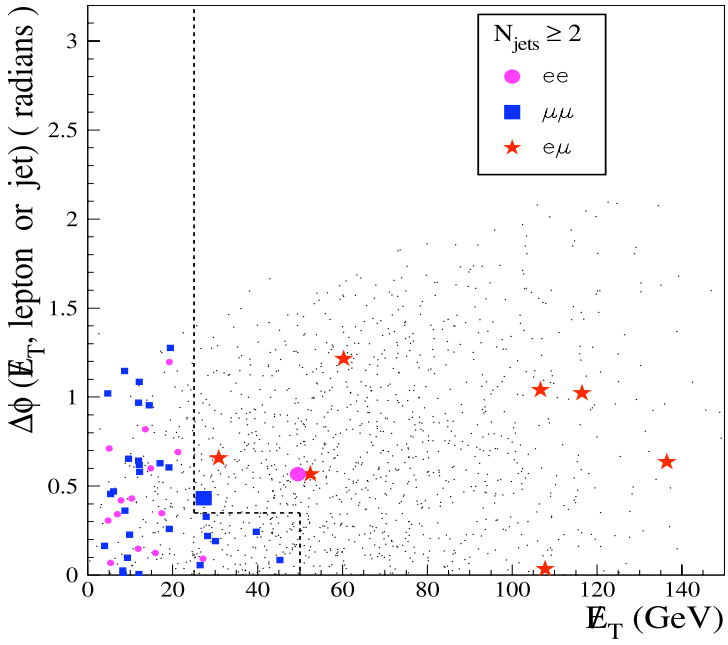

Figure 1.1: From the Run I $t\bar{t}$ dilepton analysis. Azimuthal angle between the $\not\!\!E_T$ and the nearest lepton or jet versus the $\not\!\!E_T$. The 10 candidate events and the $t\bar{t}$ Monte Carlo with $m_t = 175$ GeV are plotted. The 10 dilepton candidates are indicated by the larger symbols. The dashed lines represent the $\not\!\!E_T$ cuts.

derstood, which also lends itself to the possibility of performing precision Standard Model measurements.

This analysis uses a global approach for testing the Standard Model using high momentum dilepton events. It is global in the sense that the selection of the events used is as open as possible (has a minimum of selection criteria), with the aim of using the full statistical power of the data, and to be sensitive to as many new physics processes as possible. Our new methodology has been used to make precision measurements of the $t\bar{t}$, WW and $Z \to \tau\tau$ production cross sections simultaneously in a likelihood fit of the data. The details are given in chapter 5 and 6.

In this thesis we present the results of analyzing about 360 pb^{-1} of CDF Run II data. We are also submitting these results and the method for publication in Physical Review Letters. This analysis will continue to be updated as new data becomes available at the CDF detector, and is expected to yield the best CDF $t\bar{t}$ and WW cross sections in the dilepton channel,

The Run I method for measuring the $t\bar{t}$ and WW cross section was essentially a counting experiment involving a series of cuts in kinematical variables of the event that select preferentially signal events over background processes. In Run II this same method has been used and measurements of the $t\bar{t}$ and WW production cross section from dilepton events have been performed [3, 4]. The author of this thesis was also involved in these more traditional dilepton $t\bar{t}$ and WW analyses. The Run II WW measurement made the first conclusive observation of $p + \bar{p} \to WW$ at a hadron collider [4]. The method described in this thesis provides an improvement to the precision of those measurements due to its global nature.

1.2 The Standard Model

Virtually all experimental data from high energy experiments that has been collected so far can be accounted for by the so-called *Standard Model* of particles and their interactions. The theory, developed in the 1970's [5] combines various subcomponents that describe the different types of interactions. According to this model, all matter is built from a small number of fundamental spin-1/2 particles, or *fermions*. The fundamental fermions are six *quarks* and six *leptons*, which can be categorized into 3 distinct "generations". The interactions between these particles are mediated by integer-spin particles called *bosons*.

In subsequent subsections we will enter into more detail about the fundamental particles, but as a summary, in Table 1.1, we list the Standard Model lepton and quark flavors and the ratios of their charges to the electron charge e.

Particle	Flavor			Q/|e|
leptons	e(electron)	μ(muon)	τ(tau-lepton)	-1
	ν_e	ν_μ	ν_τ	0
quarks	u	c	t	+2/3
	d	s	b	-1/3

Table 1.1: The three generations of Standard Model fundamental fermions

There are four known forces governing the interactions of particles: the electromagnetic, weak, strong and gravitational forces. Historically, with the evolution of our understanding of nature at higher energy scales, the different forces have been progressively unified. James Clerk Maxwell, with his theory of electromagnetism [6] unified the electric and magnetic forces as two manifestations of the same fundamental underlying phenomena. The electromagnetic and weak forces are now understood as two expressions of the same electro-weak force [7]. This later unification is one of the greatest achievements in modern science and serves to explain the vast majority of physical behavior we see in Nature. In Table 1.2 we can see some of the properties

of the four known forces; their typical range, their relative strength which is proportional to their *coupling constant* and the associated bosons that mediate the forces. In succeeding sections we will delve into greater detail both on the fundamental constituents of matter, as well as in their interactions.

Interaction	Mediator	Coupling Constant	Range(m)
gravitational	G(graviton)	10^{-40}	∞
weak	$W^{\pm}$, Z^0	10^{-6}	10^{-18}
electromagnetic	γ(photon)	1/137	∞
strong	g(gluon)	≤ 1	10^{-15}

Table 1.2: The Standard Model fundamental interactions

The strong force, which is mediated by the exchange of gluons, acts only over very short ranges. Only quarks interact via this force and it is responsible for keeping the nuclei of atoms together. The electromagnetic force, mediated by photons, is felt by particles that posses electric charge, and its relative strength is about two orders of magnitude smaller than the strong force. The weak force, mediated by the $W^{\pm}$ and Z^0 gauge bosons, interacts with all particles with the exception of gluons. This force is responsible for neutron decay, for example. Finally the gravitational force is the weakest of all, and it is capable of interactions at any distance. It affects all known particles.

1.2.1 Leptons

The fundamental fermions listed in Table 1.1, with half integer spins, follow Fermi-Dirac statistics [8]. This postulates that if Ψ represents the wave function of a system of fermions, then under the exchange of two identical fermions we must have: $\Psi \rightarrow -\Psi$, or in other words, the wave function must be *anti-symmetric*. A consequence of this behavior is that two or more identical fermions cannot exist in the same quantum state, which is known as the *Pauli Exclusion Principle*.

From the expression of the relativistic energy of a particle: $E = \pm\sqrt{p^2c^2 + m^2c^4}$, Paul Dirac first postulated the existence of antimatter [9], justify the negative energy solution to the expression. Dirac's original picture of antimatter, developed in the context of electrons, was that vacuum actually consisted of an infinitely deep sea of completely filled negative energy levels. The positive electrons would be prevented from falling into negative energy states because of the Pauli principle. An electron with negative energy could be lifted into a positive energy state by a supply of energy, leaving a *hole* with a defect of positive electric charge (negative electric charge) , which represents the positron, thus describing the electron-positron pair creation. This picture however is not valid for boson pair creation. In our current picture of particle physics, all particles have a corresponding antiparticle with the same characteristics as the particle but with opposite electric charge, however for some particles with no charge, such as the photon, the antiparticle and particle are the same (called Majorana particles). Formally, from the solution of the free particle equation of motion, the wave function is given by $\Psi = Ae^{-i(Et-px)/\hbar}$, thus an antiparticle can be represented by a particle of negative energy $-E$ and momentum $-p$ traveling in the negative x direction and backwards in time (replacing Et with $(-E)(-t)$ and px with $(-p)(-x)$).

The electron was the first of the elementary particles to be clearly identified. It is also by far the lightest among the charged particles (with a mass of 0.511 MeV). The discovery of the electron is usually credited to Sir Joseph John Thompson, with the publication of a paper in 1897 [10]. In this paper, Thompson describes his investigations on the nature of discharges of electricity in rarefied gases, and in particular the type of discharge known as cathode rays. His conclusion was that the rays are a flow of particles that are known today as electrons. He would later also measure the mass of the electrons [11].

The positrons, postulated by Paul Dirac, were first observed by Carl D. Anderson in 1932 [12] in a cloud chamber placed in a magnetic field and exposed to cosmic rays. The discovery was confirmed in 1933 by Blacket and Occhialini under different cloud chamber conditions.

Every fermion and boson has an antiparticle, however, for fermions there is a conservation law: the difference between the number of fermions and anti-fermions is a constant. Formally one defines the fermion number as +1 and the anti-fermion number as -1, where the total fermion number is conserved in all interactions. Thus fermions can only be created and destroyed in pairs.

The discovery of muons ($\mu^{\pm}$) resulted from observations of cosmic radiation in 1937 by Carl D. Anderson [13]. In cosmic rays, muons are decay products of short lived pi-mesons (pions), which are integer-spin composite particles produced in the upper atmosphere by primary cosmic ray protons from outer space. Muons were originally though to be associated with the nuclear forces holding protons and neutrons together. This conclusion was derived from the realization by Hidekei Yukawa in 1935 that there is a simple relationship between the range of any force and the mass of the particle whose exchange produces the force [14]: the distance at which the force drops rapidly to zero is inversely proportional to the mass of the mediator particle. This theoretical advance, together with the fact that the mass of the muon is about 200 times that of the electron, lead to the conclusion that muons were ideally suited for mediating forces in the range of atomic nuclei ($10^{-15}\ m$). It was later shown that such forces are mediated mostly by pions ($\pi^{\pm},\ \pi^{0}$), which are composite particles (of u and d quarks) discovered in 1947 by the University of Sao Paulo physicist Cesar Lattes [15]. With the use of photographic emulsions exposed to cosmic rays, he observed decays of the type $\pi^{+} \rightarrow \mu^{+} + \nu_{\mu}$, with the muon in turn decaying $\mu_{+} \rightarrow e_{+} + \nu_{e} + \bar{\nu}_{\mu}$. (We will talk about the neutrinos (ν) soon). Muons,

it turns out, are not stable particles and typically decay to electrons as in the decay just cited. The muon mean lifetime is $(2.19703 \pm 0.00004) \times 10^{-6}\ s$ [16].

The τ leptons are much more massive than the muons, which in turn are more massive than the electrons. See Table 1.3 for the rest masses of the leptons. The τ leptons were first observed in particle accelerator experiments at the Stanford Linear accelerator in 1975 [17]. The τ's were not observed directly, but rather from e^+e^- collisions were events of the type $e^+ + e^- \rightarrow e^\pm + \mu^\pm +$ *missing energy* were detected. No other objects such as photons or hadrons were found in these events. The conclusion was that the final state electrons and muons were results of τ decays in a process of the type: $e^+ + e^- \rightarrow \tau^+ + \tau^- \rightarrow e^\pm + \mu^\pm +$ four neutrinos.

Flavor	Charged lepton mass	Neutral lepton mass
e	$m_e = 0.511$ MeV	$m_{\nu_e} \leq 10$ eV
μ	$m_\mu = 105.66$ MeV	$m_{\nu_\mu} \leq 0.16$ MeV
τ	$m_\tau = 1777$ MeV	$m_{\nu_\tau} \leq 18$ MeV

Table 1.3: The lepton masses. The neutrino masses limits are from direct measurements, and exclude neutrino flavor mixing experiments.

The idea of the existence of neutrinos dates back to the observation by Chadwick in 1914 that the electron emitted in the beta decay of a radioactive nucleus does not emerge with a definite kinetic energy, but rather with a continuous spectrum of energies ranging from zero up to a maximum value characteristic of the nucleus that emits it. In 1930, Wolfgang Pauli proposed in a letter that another particle besides the electron is emitted in the beta decay and shares the available energy, and that this particle, of neutral electrical charge, is not a photon but it is so penetrating in matter that its energy is not converted to heat with any great efficiency. This particle came to be known as the neutrino. Enrico Fermi, in 1933, incorporated the neutrinos into his quantum field theory of beta radioactivity [18] . By comparing the distribution of electron energies predicted by Fermi's theory with what was experimentally observed, it was possible to conclude that the mass of the neutrino must be very small, much less

than the mass of the electron. It is now known that there are three different flavors of neutrinos corresponding to each flavor of charged lepton. From experiments in Japan by the Kamiokande collaboration in 1999, it was deduced that at least one of the neutrino species must have a mass of at least 10^{-8} the electron mass [19].

The fact that neutrinos come in different flavors (ν_e, ν_μ, ν_τ), as do the charged leptons, was established in experiments with high energy neutrinos from accelerators in 1962. The neutrino beams were produced, just as they are in cosmic rays, by the decay in flight of pions created in high energy proton collisions, the decay products being muons and neutrinos. These neutrinos, in their weak interactions with matter, were found to produce muons, but never electrons. This behavior leads to the concept of *Lepton Flavor Conservation*. If we have the lepton flavor numbers L_e, L_μ and L_τ equal to +1 for each lepton and -1 for each anti-lepton, each lepton flavor number must be conserved.

Neutrinos, if massless, are observed to be only *left handed*, while anti-neutrinos only *right handed*. To explain this concept lets first introduce *helicity*. The helicity (H) is a measure of the sign of the component of spin of the particle in the direction of motion. When the component is in the same direction as the momentum, $H = +1$ and the particle is right handed, when the component is in the opposite direction as the momentum $H = -1$ and the particle is left handed. Helicity is conserved in the relativistic limit. For particles with masses, to flip the helicity it is just a matter of boosting the reference system faster than the particle, and thus the helicity is reversed in the boosted reference frame. In the electroweak theory, which we will briefly describe in section 1.2.5, we will see how the helicity states of particles play a vital role in the interactions. In contrast with the charged leptons which undergo electromagnetic and weak interactions, neutrinos only interact via the weak force. If neutrinos have mass, which appears they do, this interaction would be altered since

both helicity states would be possible for the neutrino. As we can see neutrinos still hold many mysteries and are a rich area of current research.

1.2.2 Quarks

From the very stable nature of protons (there is no evidence for proton decay so far), protons, and neutrons, were considered fundamental particles until the 1960's. However as the number of particles discovered in accelerators proliferated to great numbers, the idea began to emerge that a greater number of these particles (hadrons) could be explained as composites of more fundamental particles. In the 1960's several theorists independently proposed the existence of the fundamental constituents of hadrons; *quarks* and *anti-quarks* (named by Murray Gell-Man, one of the early proponents of the idea [20]). Originally there were expected to be just three kinds of quarks, as they seemed sufficient to explain the hadron zoo of particles; the up quark (u) with a charge of $2e/3$ where e is the magnitude of the electron charge, and the down (d) and strange (s) quarks with a charge of $-e/3$. The proton, for example, consists of two up and a down quark, the neutron of two down and an up quark. With the discovery of further hadrons (charmonium states for example), the number of quarks had to be expanded. Furthermore a third generation of quark became necessary when Kobayashi and Maskawa realized that the observation of CP violation by neutral Kaons, could not be accommodated in the Standard Model with just two generations of quarks [21]. Now the Standard Model has six quarks, as listed in Table 1.4, with their respective antiparticles.

Quarks do not exist as free particles, and thus the definition of mass is not trivial, as it depends on the magnitude of the potential binding the quarks together. The masses given in Table 1.4 are indicative only (for all but the top quark), specifically, the u and d mass values are derived thanks to a property of bound quark states

Flavor	Rest mass (GeV)
u or d (up or down)	$m_u \simeq m_d \simeq 0.31$
s (strange)	$m_s \simeq 0.50$
c (charm)	$m_c \simeq 1.6$
b (bottom)	$m_b \simeq 4.6$
t (top)	$m_t \simeq 176$

Table 1.4: The quarks and their masses.

called asymptotic freedom. In nature only two types of combinations of quarks are observed, *baryons* composed of three quarks and *mesons* composed of a quark-anti-quark pair. These are held together by the gluon mediated strong force. The baryons and mesons are known collectively as hadrons.

The strange quark (s) is a component of so called strange particles, discovered in cosmic rays in the 1950's, whose behavior was resolved with the realization that these particles were produced in pairs of opposite "strangeness". The discovery of the c quark resulted from the observation of very massive meson states in 1974 of type $\Psi = c\bar{c}$ [22]. The b quark was discovered following the detection of heavier mesons (upsilons) $Y = b\bar{b}$ in 1977 at Fermilab [23]. The last quark to be discovered was the very heavy top (t) in 1995 at the Tevatron accelerator at Fermilab, by the CDF and D0 collaborations. The study of the production process of the top quark is one of the objectives of this thesis project. In fact the advisor of this thesis was actively involved in those first top measurements [24, 25], and the author of this thesis was actively involved in the first CDF-Run II top quark measurements [3], which were the first measurements of the top quark made after its Run I discovery.

The hadrons can be arranged in octuplet, decuplet, etc. families. In the decuplet state, which consists of baryons of spin 3/2, we have a particle that has three u quarks in a completely symmetric spin state $\Delta^{++} = u \uparrow u \uparrow u \uparrow$. This clearly violates the Pauli exclusion principle. To mend such a problem a new degree of freedom was proposed called *color* [26]. The theory of Quantum Chromodynamics (QCD)

postulates three colors (red (r), green (g) and blue (b)). The baryons and mesons are colorless, that is, they have zero net color. For example, in the case of the Δ^{++} each of the quarks has a different color. The sum of the 3 color quantum numbers sums to a net zero color state. Anti-quarks carry anti-color, so that a $q\bar{q}$ meson state is also colorless, and the strong interaction is assumed to be invariant under color exchange.

1.2.3 Gauge Bosons

As was outlined previously, gauge bosons are responsible for mediating the fundamental forces in the Standard Model. The photon, responsible for the electromagnetic force, is a massless spin 1 particle. It is a so-called *Majorana* particle because it is its own antiparticle. Photons are the propagators of the electromagnetic force between particles that posses electric charge. As bosons, photons are not bound by the Pauli exclusion principle and obey Bose-Einstein statistics.

The $W^{\pm}$ and Z^0 gauge bosons are responsible for mediating the weak force. The weak force interacts with all particles except gluons. The first observation of W and Z bosons was made in the Super Proton Synchrotron at CERN in 1983 by the UA1 and UA2 collaborations [27]. The Super Proton Synchrotron was used as a proton-anti-proton collider, with each beam colliding at 400 GeV. Z's were produced through the Drell-Yan process, which we will describe in section 2.2.3. The W's were observed first in W+hadronic-jet events. The precision measurement of the production cross section for $p + \bar{p} \rightarrow W^+ + W^-$ and the process $p + \bar{p} \rightarrow Z^0 \rightarrow \tau + \tau$ are another part of the topic of research presented in this thesis. The WW pair production was first observed from $e^+ + e^-$ collisions in the LEP collaboration at CERN. As previously mentioned, the first observation of $p + \bar{p} \rightarrow W^+ + W^-$ production was by the CDF collaboration at the Tevatron [4]. The W's and Z's can decay both leptonically (to leptons) and hadronically (to quarks). Their lifetime is very short, of the order of

2.6×10^{-25} s for the three particles. Unlike the photon, the W and Z bosons are massive, with the W having a mass of about 80.4 GeV and the Z of about 91.2 GeV.

The gluons are responsible for the strong quark-quark interaction. In the same way that the electromagnetic interaction is felt by particles with electric charge, the strong interaction is felt by particles with colour. Each gluon carries a colour-anticolour pair. These color-anticolour pairs belong to an octet of states: $r\bar{b},\ r\bar{g},\ b\bar{g},$ $b\bar{r},\ g\bar{r},\ g\bar{b}, 1/\sqrt{2}(r\bar{r}-b\bar{b}),\ 1/\sqrt{6}(r\bar{r}+b\bar{b}-2g\bar{g})$. The gluon has no mass (experiments have placed limits on the gluon mass to less than a few MeV) and is a spin 1 particle. The strong interaction, as opposed to from the other forces, increases with distance, resulting in the impossibility of observing free quarks. Also differently to the force carriers of the electroweak interactions, the gluon can interact with itself, with gluon-gluon interactions playing a role in the properties of the strong force. In section 1.2.5 we will describe in more detail the theory (QCD) that describes the gluon mediated strong force, but first we discuss briefly the so called Hadronization Process of high energy quarks and gluons in the next section.

We summarize our picture of the Standard Model fundamental particles in Figure 1.2.

1.2.4 Hadronization of High Energy Quarks and Gluons

As we mentioned, quarks do not exist in a free state because the force binding them increases with distance, and as the energy used to separate them increases, a new quark-anti-quark pair can be created and we end up with two quark pairs. However at close range, confined inside hadrons, quarks exhibit "asymptotic freedom" [28].

The high energy quarks and gluons that result from the events we study in our detector, quickly go through the so called *hadronization* process. We end up with a multitude of hadrons (called a "jet") in a cone around the direction of the originally

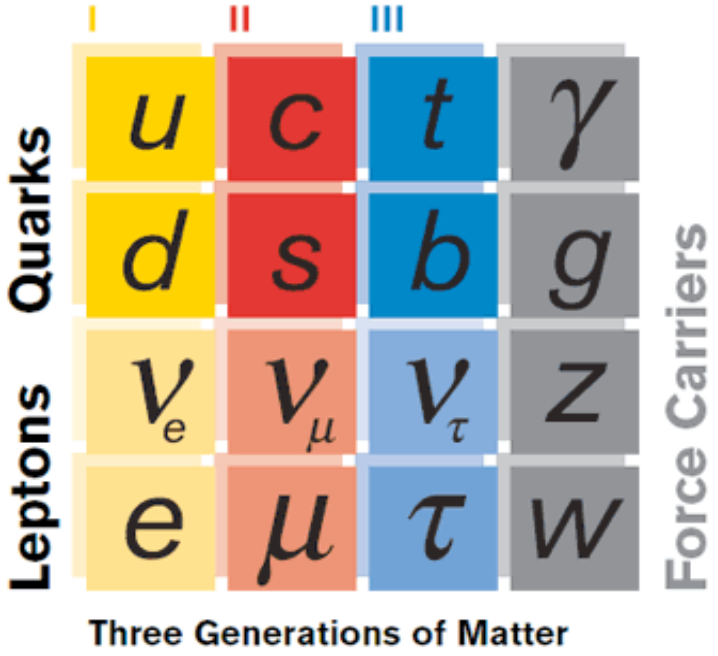

Figure 1.2: The Standard Model Fundamental Particles.

produced high energy quark or gluon. The hadronization process in not yet fully understood, but there are several models that describe its general behavior. One such model is the Lund String model [29].

In the Lund String Model, the interaction between quarks is idealized as a straight, uniform field tube, with the field stored in this color field tube increasing linearly with the distance between the charged particles. As the q and $\bar{q}$ move apart, the potential energy stored in the string increases, and the string eventually breaks producing a new $q'\bar{q}'$ pair with each quark combining with one of the quarks of the original pair. If the invariant mass of either of the pairs is large enough, further breaks occur. In the Lund model, the break-up process is assumed to proceed until only on-mass-shell hadrons remain. In the progressive fragmentation into hadrons, in this model, heavy quark production tends to be suppressed.

1.2.5 The Standard Model Lagrangian Formulation

In the Gauge Quantum Field Theory description of nature, particles are represented by quantized fields and their behavior and interaction is expressed by the Lagrangian density $\mathcal{L}$. One clear benefit of this formulation is the fact that any transformation on the field Ψ that leaves unchanged the action of the Lagrangian $S = \int \mathcal{L}(\Psi, \delta\Psi)dx$ can be associated with conserved quantities rather easily with the use of Noethers Theorem [30].

In the following sections we will give a brief description of the Lagrangian formulation of the theories of the electromagnetic, the unified electroweak, and the strong forces.

Quantum Electrodynamics (QED)

A free fermion is described by the Dirac spinnorfField Ψ Lagrangian:

$$\mathcal{L} = \bar{\Psi}(i\gamma^\mu \partial_\mu - m)\Psi \tag{1.1}$$

where γ^μ are the SU(2) four dimensional representations of the Pauli σ matrices (called the Weil representation) , and μ runs through the three spacial and the time coordinates. The action is given by $S = \int d^4x\mathcal{L}$. The equations of motion are obtained from the action as follows;

$$\delta S = 0 = \int d^4x(\frac{\delta\mathcal{L}}{\delta\Psi}\delta\Psi + \frac{\delta\mathcal{L}}{\delta\partial_\mu\Psi}\delta\Psi) \tag{1.2}$$

which yields the Dirac equation:

$$(i\gamma^\mu\partial_\mu - m)\Psi = 0 \tag{1.3}$$

In Quantum Electrodynamics (QED) [31], the Lagrangian must have a term that

yields the Maxwell equations. If we have $F_{\mu\nu} = \partial_\mu A_\nu - \partial_\nu A_\mu$, with A^μ the 4-vector for the photon field, and if we express the electric and magnetic fields as $\vec{E} = -\nabla A^0 - \frac{\partial \vec{A}}{\partial t}$, and $\vec{B} = \nabla \times \vec{A}$, then the Lagrangian term;

$$\mathcal{L} = -\frac{1}{4} F_{\mu\nu} F^{\mu\nu} \tag{1.4}$$

yields the Maxwell equation with a zero source when considering the stationary values of the action. Now, to reach the full QED Lagrangian we must add a term for the motion of the free electrons, such as the Lagrangian of the free fermions, and a coupling term between electrons and photons. In QED the interaction term can be assumed to be of the form $eA_\mu \bar{\Psi} \gamma^\mu \Psi$, with Ψ being the electron field and e the electron charge (this term describes an interaction vertex with two electron or positron legs, and a photon leg). Then the full QED Lagrangian is given by;

$$\mathcal{L}_{QED} = \bar{\Psi}(i\gamma^\mu \partial_\mu - m)\Psi + eA_\mu \bar{\Psi} \gamma^\mu \Psi - \frac{1}{4} F_{\mu\nu} F^{\mu\nu} \tag{1.5}$$

The association with the Maxwell equations is furthered when taking the charge density to be $J_\mu = e(\Psi \bar{\gamma_\mu} \Psi)$.

From the QED Lagrangian a series of so called Feynman rules can be derived that serve to describe the interaction between the different particles and calculate the amplitude for such processes. These rules are associated with a graphic representation of the processes called Feynman diagrams. In such diagrams, terms in the amplitudes are associated with the electron and photon legs, the interaction vertices (couplings) and the off-shell virtual particles mediating the interactions (propagators).

QED is a gauge invariant theory; in order to build a photon propagator a specific gauge choice must be made. By gauge invariance we mean that the equations of motion are unaltered under the change $A_\mu \rightarrow A_\mu + \partial_\mu \Lambda(x)$, with $\Lambda(x)$ a function

of the local coordinates x. There are many constraints on the field A_μ that can be placed to lift the invariance, or simply a term can be added to the Lagrangian of the form:

$$-\frac{1}{2\alpha}(\partial_\mu A^\mu)^2 \tag{1.6}$$

where α is an arbitrary constant. With a gauge in place we can build our Feynman diagrams and calculate the amplitude of our processes.

The theory of Quantum Electrodynamics, first proposed by Feynman, Tomonaga and Schwinger [31] describes successfully the electromagnetic interactions observed in nature, which constitute the majority of phenomena we experience in everyday life.

Electroweak Theory

In nature a variety of symmetries exist. There are also examples of symmetries that seem to hold in certain circumstances but nonetheless break in others. The mechanism known as *spontaneous symmetry breaking* describes such behavior. In this case the Hamiltonian is invariant under some symmetry, but the vacuum state of the Hamiltonian is not invariant, thus breaking the symmetry. The original proponents of the weak interaction formulation had to deal with this issue. The early attempts to write down a theory of massive mesons (massive vector meson theory) would yield a non-renormalizable theory. When computing physics process amplitudes, there are cases where a Feynman diagram would yield an infinite amplitude (in QED for example in some of the radiative corrections). These can be canceled in renormalizable theories in a systematic way with the use of the renormalization group. In QED, this involves adding to the Lagrangian counter-terms, rescaling the fields, and specifying physical conditions such as physical masses and coupling constants. In some theories, it is not possible to fix the divergences to all orders of the perturbative

expansion (non renormalizable theories). It was found that a renormalizable theory of electroweak forces was possible if the concept of spontaneous symmetry breaking was incorporated.

A simple example of spontaneous symmetry breaking is a scalar theory with a $-\lambda/4!\Psi^4$ interaction term. Such a theory would have the Hamiltonian invariant under a $\Psi \rightarrow -\Psi$ transformation. In this theory we can define a potential from the mass and the interaction term as $V(\psi) = -1/2m^2\Psi^2 + \lambda/4!\Psi^4$. This potential has two minimum values. If we redefine the field by choosing, lets say, the positive minimum v to write $\Psi = v + \Phi$ and replace this in the Lagrangian, we end up with a term with Φ^3. The $\Phi \rightarrow -\Phi$ invariance is gone. This is an example of a symmetry breaking by choosing one of the vacuum expectation values of Ψ (in this case v).

In the Weinberg-Salam theory of weak interactions, we begin with a theory with SU(2) gauge symmetry. To break the symmetry a scalar field in the spinor representation of SU(2) is introduced. Also U(1) invariance is required, and two different coupling constants g and g' for the SU(2) and U(1) interactions are postulated.

An isospin triplet of weak currents can be defined as:

$$J^i_\mu(x) = \bar{\chi}_L \gamma_\mu \frac{1}{2} \sigma_i \chi_L \tag{1.7}$$

where σ_i are the Pauli matrices and the isospin left handed lepton fields are given by:

$$\chi_L = \begin{pmatrix} \nu_e \\ e \end{pmatrix}_L \tag{1.8}$$

The J^3_μ current represents the neutral current and the J^1_μ and J^2_μ are linear combinations of the positive and negative charged currents. The current we defined reminds us that the weak isospin current couples only to left handed fermions. The right handed lepton sector χ_R is only a singlet (there exist no right handed neutrinos if

they are massless);

$$\chi_R = (e)_R \tag{1.9}$$

To include the right handed component the electromagnetic current J_μ^{em} that couples to both left and right handed fermions is introduced;

$$J_\mu^{em} = J_\mu^3 + \frac{1}{2} j_\mu^Y \tag{1.10}$$

with;

$$j_\mu^Y = \bar{\Psi} \gamma_\mu Y \Psi \tag{1.11}$$

where Ψ is the fermion field (containing leptons and quarks). If T^3 is the isospin of the fermions, $\pm 1/2$ for leptons, 0 for the quarks, and the charge is given by Q, then the hyper-charge Y above is given by the equation: $Q = T^3 + Y/2$.

Below are the isospin components that make up Ψ for the first generation of leptons and quarks. Including the other two generations is done in an identical way.

T=1/2	T=0
$\begin{pmatrix} \nu_e \\ e \end{pmatrix}_L$	e_R
$\begin{pmatrix} u \\ d \end{pmatrix}_L$	u_R, d_R

The electroweak Lagrangian density is written in terms of the weak fields W_μ and B_μ as given below.

$$\mathcal{L} = g J_\mu W^\mu + \frac{g'}{2} j_\mu^Y B^\mu \tag{1.12}$$

The symmetry is broken by selecting a vacuum expectation value on Ψ components, for example for the lepton doublet;

$$< \Psi >= \begin{pmatrix} 0 \\ v/\sqrt{2} \end{pmatrix} \tag{1.13}$$

After the symmetry breaking, the W_μ and B_μ fields are recombined and emerge as the physical photon field A_μ, the massive vector particle Z_μ, and a charged doublet of vector particles $W_\mu^\pm$ given by:

$$\begin{aligned} W_\mu^\pm &= \frac{1}{2}(W_\mu^1 \pm W_\mu^2) \\ Z_\mu &= W_\mu^3 cos(\theta_W) - B_\mu sin(\theta_W) \\ A_\mu &= W_\mu^3 sin(\theta_W) + B_\mu cos(\theta_W) \end{aligned} \tag{1.14}$$

Here the so called Weinberg angle θ_W is defined by:

$$\begin{aligned} cos(\theta_W) &= \frac{g}{\sqrt{g^2 + g'^2}} \\ tan(\theta_W) &= \frac{g'}{g} \end{aligned} \tag{1.15}$$

The Electroweak Lagrangian in terms of these recombined fields has the form;

$$\begin{aligned} \mathcal{L}_{EWK} &= \frac{g}{\sqrt{2}}(J_\mu^- W^{\mu+} + J_\mu^+ W^{\mu+} \\ &+ \frac{g}{cos(\theta_W)}(J_\mu^3 - sin^2(\theta_W) J_\mu^{em}) Z^\mu + g sin(\theta_W) J_\mu^{em} A^\mu \end{aligned} \tag{1.16}$$

with the currents given explicitly by;

$$\begin{aligned} J_\mu^\pm &= \bar{\Psi}_L \gamma_\mu \sigma^\pm \Psi_L \\ J_\mu^3 &= \bar{\Psi}_L \gamma_\mu \sigma^3 \Psi_L \\ J_\mu^{em} &= \bar{\Psi}_L \gamma_\mu Q \Psi_L \end{aligned} \tag{1.17}$$

By examining the mass sector of the Lagrangian we can conclude for the bosonic field masses:

$$M_{W^+} = M_{W^-}$$

$$M_Z^2 = \frac{M_W^2}{cos(\theta_W)}$$

$$M_A = 0 \tag{1.18}$$

Experimentally, the value of $sin^2(\theta_W) = 0.2325 \pm 0.008$ places a relationship between the W and Z masses. The Weinberg-Salam electroweak model has been tested in experiment extensively and so far no discrepancies have been observed. This has been one of the most outstanding successes of field theory in the last century. However, the new experimental lower limits on neutrino masses point to the need of a possible reformulation of this theory.

Weak Decay of Quarks. The CKM Matrix

In Electroweak theory, flavor changing currents are observed that couple to left handed fermions. The flavor mixing weak interactions are parametrized by the CKM (Cabibbo, Kobayashi and Maskawa) matrix [21, 32].

$$V_{CKM} = \begin{pmatrix} V_{ud} & V_{us} & V_{ub} \\ V_{cd} & V_{cs} & V_{cb} \\ V_{td} & V_{ts} & V_{tb} \end{pmatrix} \tag{1.19}$$

This matrix is required to be unitary. The various elements of the matrix have been determined in a range of experiments. The quantity V_{ud} is determined by comparing nuclear β decay and μ decay rates. The V_{us} is determined from semi-leptonic decays of strange particles such as kaons. The V_{ub} quantity can be measured by selecting semi-leptonic decays of B mesons to non charmed particles. In the next row the quantity V_{cb} is determined from the semi-leptonic B meson decay $B \rightarrow D\ell\nu$. The quantity V_{cd} is found from the rate of single charmed particle production in high energy neutrino interactions such as $\nu_\mu + d \rightarrow \mu^- + c$ with $c \rightarrow s + \mu^+ + \nu_\mu$. The last element in the row V_{cs} can be found indirectly from the unitarity condition

$V_{cd}^2 + V_{cs}^2 + V_{cb}^2 = 1$. The top quark effects are comparatively rare, currently there are experimental efforts to better determine the mixing elements involving the top quark. The elements V_{td} and V_{ts} can also be calculated theoretically from virtual top quark effects in box diagrams from $B^0 - \bar{B}^0$ mixing. The CKM matrix elements today are given approximately by:

$$V_{CKM} = \begin{pmatrix} V_{ud} = 0.975 & V_{us} = 0.221 & V_{ub} = 0.005 \\ V_{cd} = 0.221 & V_{cs} = 0.974 & V_{cb} = 0.04 \\ V_{td} = 0.01 & V_{ts} = 0.041 & V_{tb} = 0.999 \end{pmatrix} \tag{1.20}$$

Quantum Chromodynamics (QCD)

Quantum chromodynamics is a SU(3) gauge field theory that formalizes the interactions between quarks and gluons. It introduces the new color charge to the gluon and quark fields. The quark wave function is a color SU(3) triplet;

$$\Psi(x) = \begin{pmatrix} \Psi_r(x) \\ \Psi_b(x) \\ \Psi_g(x) \end{pmatrix} \tag{1.21}$$

The QCD Lagrangian is given by:

$$\mathcal{L} = -\frac{1}{2} tr(\bar{F}_{\mu\nu}\bar{F}^{\mu\nu}) + \bar{\Psi}(p_m u + g\bar{A}_\mu)\gamma^\mu\Psi \tag{1.22}$$

where the tensor of the gluon field strength ($\bar{F}_{\mu\nu}$) is given by;

$$\bar{F}_{\mu\nu} = \partial_\mu \bar{A}_\nu - \partial_\nu \bar{A}_\mu - ig[\bar{A}_\mu, \bar{A}_\nu] \tag{1.23}$$

and the gluon field is a sum over the gluon color octet of fields;

$$\bar{A}_\nu(x) = \sum_{i=1\to 8} \frac{1}{2}\hat{\lambda}_a A_\nu^a(x) \tag{1.24}$$

where the $\hat{\lambda}_a$ are the 8 SU(3) matrices. From the QCD Lagrangian we can see that not only are there gluon-quark interaction terms, but also gluon only vertices with three or four legs.

In spite of the fact that the use of perturbative methods, that lead to Feynman diagrams of decreasing amplitude in the perturbation expansion, has been very successful for the QED and Electroweak theories, for QCD the perturbative expansion has to be applied with care. The essential problem is; under which circumstances does a perturbative expansion in the coupling constant in QCD converge. Given the running nature (dependent on momentum) of the coupling constant, it has been found that convergence in the perturbative treatment can be achieved for high momentum processes, while for small momenta the perturbative treatment breaks down. This is in contrast with QED for example were the perturbative treatment converges for small and large momenta as long as it is not in nonphysically high scales such as 10^{20} GeV where it breaks down. The QCD perturbative behavior, however, fits quite well into the general experimental picture, where high momenta phenomena agree quite well with perturbative predictions, and where the observed quark confinement is treated in a non perturbative way.

Chapter 2

High Momentum Dilepton Physics at the Tevatron

In this chapter we describe the main Standard Model physics processes that play a role in our analysis. More specifically the production processes from $p\bar{p}$ collisions that can result in final states with two high energy leptons. We describe the "signal" processes in our analysis, the $t\bar{t} \to WbWb \to \ell\nu b\ell\nu b$, $WW \to \ell\nu\ell\nu$ and $Z \to \tau\tau \to \ell\nu\ell\nu$ ($\ell = e$ or μ) production. There are other processes that also contribute to our dataset, such as $W\gamma$, WZ, ZZ, W+jets and $Z \to ee/\mu\mu$, which we consider as "backgrounds". We also review the state of previous experimental measurements relevant to our results.

2.1 Parton Distribution Functions (PDF) in Hadron Colliders

We first discuss in more detail the nature of $p\bar{p}$ collisions.

The constituent quarks confined inside hadrons sometimes are called partons, in the context of the quark-parton model [33]. In the $p\bar{p}$ colliding beam at the Tevatron, the energies of the individual constituent quarks in the proton and antiprotons follow a distribution, hence there is an uncertainty in the center of mass energies at which individual parton collisions take place. To describe these momenta distributions, we use so-called Parton Distribution Functions (PDF's). Given the asymptotic freedom of the quark constituents in hadrons, perturbative methods can be used in evaluating PDF's.

In order to determine the partonic structure of the proton, high energy lepton

nucleon deep inelastic scattering events are analyzed, events of the form $l+N \rightarrow l'+X$ where N and X are hadrons. From these collisions it is found that the cross sections are large in contrast with the elastic cross sections, and they depend weakly on the square of the momentum transfered (Q^2). This is a sign of elastic scattering by point like constituents inside the hadrons in these types of collisions. In such elastic scattering of the constituent partons, the scattered parton later recombines into a hadron. It is possible then to study the distribution of the fraction of the momentum carried by the partons, sometimes also called the structure functions. This information is used for the Parton Distribution functions when colliding proton-anti proton beams, and to obtain a distribution of the center of mass energies of the individual parton collisions. These distributions introduce a level of uncertainty in the total momentum of a quark-quark collision along the beam direction.

When generating Monte Carlo simulations of the data events, the PDF distributions have to be incorporated. There are many possible parameterizations of such functions. We use the CTEQ6 set of PDF's [34], where the authors provide both the parametrization and computer source code for calculating the momenta distributions.

2.2 Standard Model Phenomenology

In this analysis we study Standard Model processes which result in two high momentum final state leptons, where the leptons are electrons or muons. In the case of processes involving tau leptons, they enter our analysis only through the possible decay to electrons or muons.

The main processes we study, that constitute the cross sections we measure, are:

- $p\bar{p} \rightarrow t\bar{t} \rightarrow WbWb \rightarrow \ell\nu b\ell\nu b$, which results in a signal of 2 leptons + hadron jets + missing energy.

- $p\bar{p} \to WW \to \ell\nu\ell\nu$, which result in a signal of 2 leptons + missing energy.
- $p\bar{p} \to Z \to \tau\tau \to \ell\nu\ell\nu$, which result in a signal of 2 leptons + missing energy.

In the following sections we will describe some of the phenomenology of these processes, including one of our most important backgrounds, the Drell-Yan ($Z/\gamma* \to ee/\mu\mu$) contribution.

2.2.1 The $t\bar{t}$ Production and Decay

In hadronic collisions which involve large momentum transfer (high Q^2 as compared to the QCD energy scale), the processes contributing to the $t\bar{t}$ cross section are short distance interactions with can be described by the parton model. The heavy top quark mass requires a large Q^2, and thus ensures a small value of the QCD coupling, which makes the use of perturbation theory possible. The total inclusive cross section for heavy quark production in perturbative QCD is given by;

$$\sigma(s) = \sum_{i,j} \int_0^1 dx_1 \int_0^1 dx_2 f_i(x_1, \mu) f_j(x_2, \mu) \sigma_{ij}(\hat{s}, m_t, \alpha_s(\mu)) \tag{2.1}$$

where i and j go over all the initial parton states, and the integration is over the two interacting parton momentum fractions. We also have that;

- $f_i(x_1, \mu)$: The structure function for parton i. This represents the probability that the parton i is carrying a fraction of the hadron momentum between x_1 and $x_1 + dx$.
- μ^2: The renormalization scale.
- $\hat{\sigma_{ij}}$: The short distance cross section for $t\bar{t}$ production from the incident partons i and j.

- α_s: The strong running coupling constant, which decreases as a function of $\hat{s}$.
- $\hat{s}$: The square of the center of mass energy in the i-j parton system.
- m_t: The top quark mass.

The $t\bar{t}$ production, to the leading order, can be due to quark-quark annihilation, or gluon-gluon fusion. In Figure 2.1 we can see the leading order Feynman diagrams associated with such processes. From the Feynman diagrams, the cross sections can be calculated, where we have;

- $q\bar{q}$ annihilation:

$$\hat{\sigma}_{q\bar{q}} = \frac{8\pi\alpha_s^2}{27\hat{s}}\sqrt{1-\frac{4m_q^2}{\hat{s}}}(1+\frac{2m_q^2}{\hat{s}}) \tag{2.2}$$

- gg fusion:

$$\hat{\sigma}_{gg} = \frac{\pi\alpha_s^2}{12\hat{s}}[(\frac{4m_q^4}{\hat{s}^2}+\frac{16m_q^2}{\hat{s}}+4)ln\ y-(7+\frac{31m_q^2}{\hat{s}})\sqrt{1-\frac{4m_q^2}{\hat{s}}}] \tag{2.3}$$

where;

$$y = \frac{1+\sqrt{1-\frac{4m_q^2}{\hat{s}}}}{1-\sqrt{1-\frac{4m_q^2}{\hat{s}}}} \tag{2.4}$$

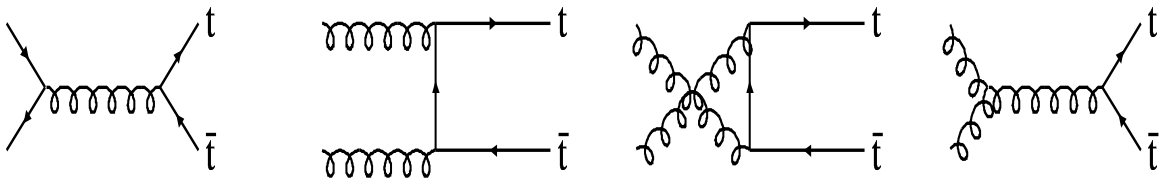

Figure 2.1: The $t\bar{t}$ production leading-order Feynman diagrams.

When $\hat{s}$ is close to the threshold ($\hat{s} \sim 4m_t^2$), if we take the expressions above, the ratio of the gluon fusion to the $q\bar{q}$ annihilation is 3:1. However, the cross sections also depend on the structure functions that determine the parton luminosities. The gg fusion luminosity decreases with respect to the $q\bar{q}$ luminosity for increasing values of the top mass. At a mass of 175 GeV the ratio falls to 1:5 (gg:$t\bar{t}$). The top mass is now actually measured to about 2% precision to be $172 \pm 1.3 \pm 1.9$ GeV [35].

The leading order $t\bar{t}$ cross section is is increased by about 25% due to next to leading order terms ($O(\alpha_s^3)$). In Figure 2.2 we can see some of the diagrams that contribute to the $q\bar{q}$ next to leading order (NLO) cross section corrections. In gluon fusion we also have similar NLO diagrams, and at this order contributions from quark-gluon fusion are also present. The initial state gluon bremsstrahlung dominates the NLO corrections. There are electroweak corrections with couplings to the H, Z, γ, W, but these are very small for $\hat{s}$ close to the threshold.

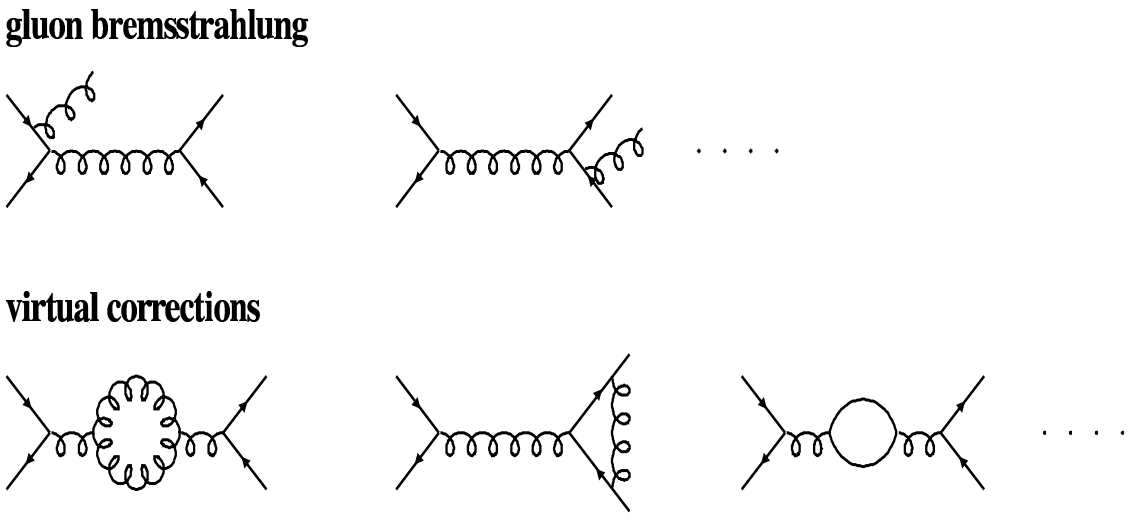

Figure 2.2: Some NLO corrections to $\sigma_{t\bar{t}}$.

The theoretical cross section of the $p\bar{p} \rightarrow t\bar{t}$ production is dependent on the top mass, and the energy of collisions. At the Tevatron Run II center of mass energy of

1.96 TeV and at a top mass of $m_t = 178$ GeV, the theoretical cross section is about $\sigma_{t\bar{t}} = 6.1 \pm 0.3$ pb [36].

The top quark in the Standard Model decays by the charged weak current into a real W and a b with branching ratio close to unity. If we assume a V-A coupling, with a CKM parameter V_{tb} in the $t \rightarrow bW$ decay vertex, we obtain for the partial width [37];

$$\Gamma(t \rightarrow bW) = \frac{G_F M_W^2}{8\pi\sqrt{2}m_i^2} \mid V_{tb} \mid^2 [\frac{(m_t^2 - m_b^2)^2}{M_W^2} + m_t^2 + m_b^2 - 2M_W^2 \times 2k] \tag{2.5}$$

with

$$k = \frac{\sqrt{(m_t^2) - (M_W + m_b)^2(m_t^2 - (M_W - m_b)^2)}}{2m_t} \tag{2.6}$$

where m_t, m_b and M_W are the masses of the top quark, bottom quark and the W boson respectively, and G_F is the Fermi constant.

If we assume $\mid V_{tb} \mid = 1$ and use the current experimental values for m_t, M_W and m_b, and use the relation $\tau_t = 1/\Gamma_t$ then we have;

$$\Gamma(t \rightarrow bW) \approx 1.55 \text{ GeV} \;\Rightarrow\; \tau_t \sim 4 \times 10^{-25}\text{s} \tag{2.7}$$

If the QCD radiative corrections are included, the width as determined by equation 2.5 is reduced by approximately 10%. Also a 1% to 2% effect is derived from electroweak corrections. The value of 1.55 GeV for the width means the top quark is so short lived that there is no time for it to go through the hadronization process before decaying, as the hadronization process is characterized by a time scale about ten times bigger than the top lifetime. This also means the top quark is produced and decays as a *free* quark.

The $t\bar{t}$ events decay to $W^+bW^-\bar{b}$. The W's further decay hadronically or leptonically, as represented in Figure 2.3. The different analyses of the $t\bar{t}$ events naturally

fall into three categories;

- Lepton + jets channel: Events which include one measurable lepton and hadronic jets when one of the W's decaying leptonically and the other hadronically.
- Dilepton channel: Events with two measurable leptons and hadronic jets from the b's and initial and final state QCD radiation when both W's decay leptonically.
- All hadronic channel: Events with a number of hadronic jets when both W's decay hadronically.

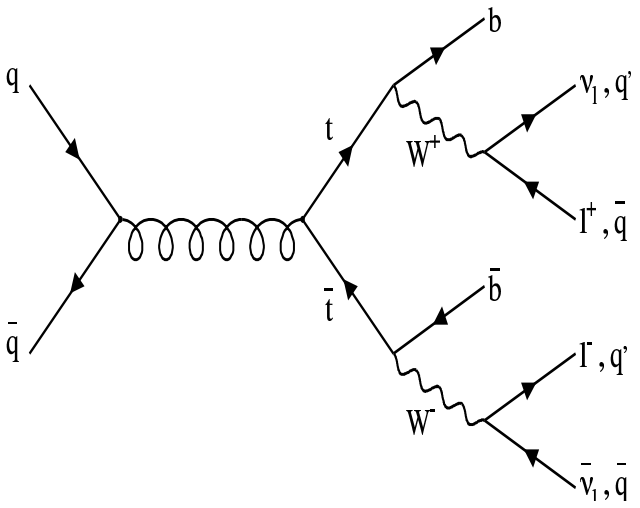

Figure 2.3: Feynman diagram for $t\bar{t}$ production followed by Standard Model decay.

In Table 2.1 we list all the decay modes of the $t\bar{t}$ events, with their respective branching ratios. In this analysis we restrict ourselves to the dilepton decay channels. It should be noted that we only identify electrons and muons in our analysis and not explicitly taus. Thus our events represent a fraction of 4/81 or about 5% of the total events. In spite of this low percentage, the dilepton channel is the cleanest for measuring the $t\bar{t}$ cross section (and WW cross section) with a relatively low

contribution from background processes. This is specially true in the $e\mu$ channel where the $Z \to ee$ and $Z \to \mu\mu$ processes do not contribute significantly resulting in a very clean sample. In fact, it is the relatively clean nature of the dilepton sample that makes it possible for our global fit analysis methodology to give good results. We will talk more about the analysis methodology in Chapters 5 and 6.

Type	Rest Decay mode	Branching Ratio
Dilepton	$t\bar{t} \to e\nu be\nu b$	1/81
	$t\bar{t} \to e\nu b\mu\nu\bar{b}$	2/81
	$t\bar{t} \to \mu\nu b\mu\nu\bar{b}$	1/81
	$t\bar{t} \to e\nu b\tau\nu\bar{b}$	2/81
	$t\bar{t} \to \mu\nu b\tau\nu\bar{b}$	2/81
	$t\bar{t} \to \tau\nu b\tau\nu\bar{b}$	1/81
Lepton + jets	$t\bar{t} \to q\bar{q}be\nu b$	12/81
	$t\bar{t} \to q\bar{q}b\mu\nu\bar{b}$	12/81
	$t\bar{t} \to q\bar{q}b\tau\nu\bar{b}$	12/81
All hadronic	$t\bar{t} \to q\bar{q}bq\bar{q}b$	36/81

Table 2.1: The $t\bar{t}$ decay modes and branching ratios.

2.2.2 The WW Production and Decay

Another significant process in our analysis is the $W^+ + W^-$ production. Just as in the case of $t\bar{t}$ production, the cross section is a convolution of the production cross section from $q\bar{q}$ collisions, with the structure functions of the proton and anti proton.

The leading order $p\bar{p} \to WW$ production process at the tevatron is shown in Figure 2.4. The so called t and u channel diagrams (labeled in the figure) contribute about 90% of the leading order cross section at the Tevatron, and can be fully described by the coupling of quarks to a W boson. The s channel diagram contributes about 10% of the cross section and is the only leading order diagram to include trilinear gauge couplings (TGC). It is worth discussing TGC's in more detail in the context of $p\bar{p} \to WW$ production, for they open an interesting window for searches of deviations to the Standard Model through anomalous couplings.

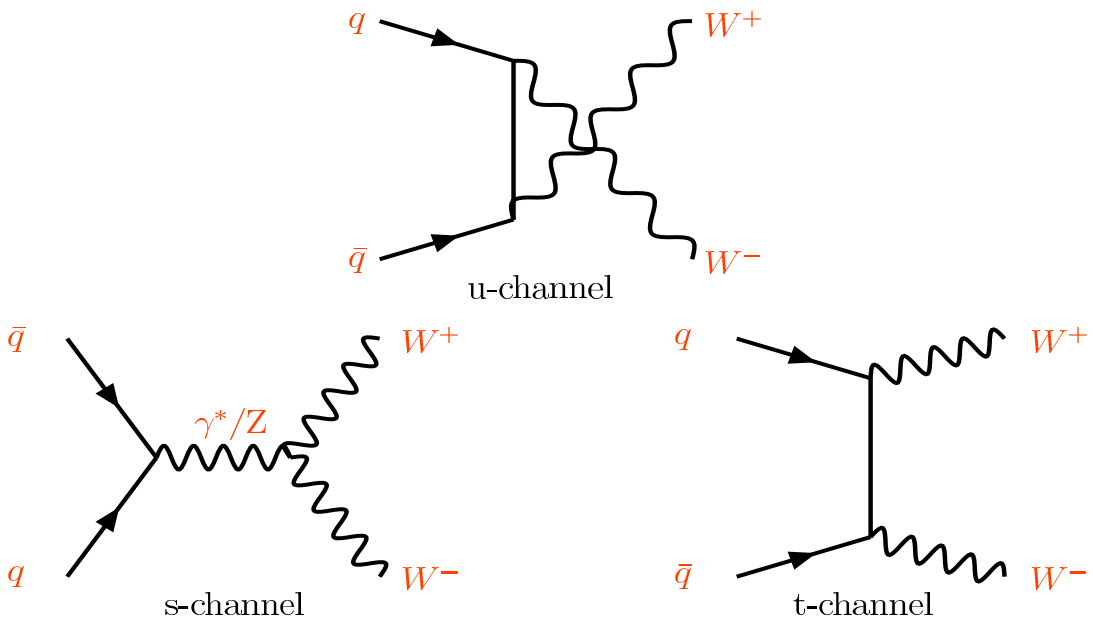

Figure 2.4: Leading order WW production at the Tevatron.

In the Standard Model Electroweak theory, there are only two possibilities for interactions between three gauge bosons; the W^+ and W^- coupling to either a Z^0 or to a photon (γ). In Figure 2.5 we illustrate such interactions. Deviations from the Standard Model such as composite Z's and W's or new Z-like bosons would alter the coupling for such vector boson interactions.

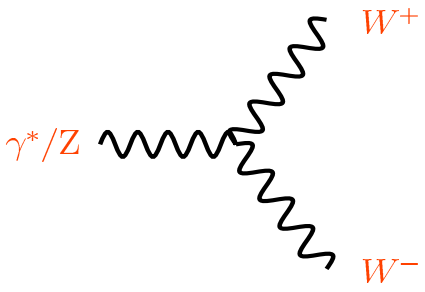

Figure 2.5: Trilinear gauge couplings in electroweak theory.

In Appendix A we describe the most general effective Lagrangian describing the

WWZ and $WW\gamma$ interaction. Such a Lagrangian is written in terms of 7 coupling constants. The coupling constants are directly related to the properties of the bosons, such as charge, magnetic dipole moment, magnetic quadrupole moment, electric dipole moment, electric quadrupole moment, etc. The Standard Model interaction is obtained by setting the κ_γ, κ_Z, g_1^γ and g_1^Z to 1 and the rest to zero (See appendix A for these couplings constants). Deviations from the Standard Model can be parametrized by the values of these constants. In this analysis we do not try to set limits on anomalous couplings, but our methodology opens the possibility of searching for deviations in the future.

In Figure 2.6 we show some of the next to leading order diagrams contributing to the WW production process. There are initial state quark and gluon radiation and radiative corrections.

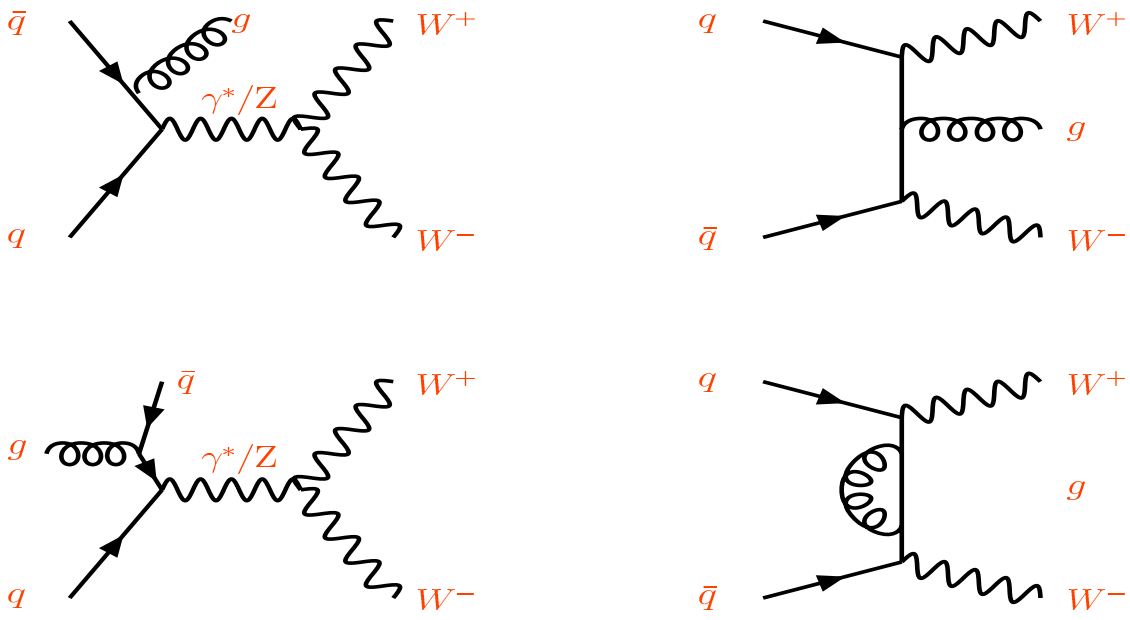

Figure 2.6: Some next to leading order corrections to the WW production process, including initial state radiation and radiative corrections.

The WW decay channels are similar to those for the $t\bar{t}$ production, given that the

$t\bar{t}$ decay is characterized by the W decays. The theoretical branching ratios are also the same as those listed in Table 2.1. Because we restrict ourselves to the leptonic decays of the W, and we measure only e and μ leptons, we end up with a branching ratio of about 5%.

The next-to-leading order (NLO) prediction for the WW production cross section at $\sqrt{s} = 1.96$ TeV, using CTEQ6 PDF's [34] is 12.4±0.8 pb, obtained with the MCFM Monte Carlo generator [38].

2.2.3 Drell-Yan Processes

The Drell-Yan process, $p\bar{p} \rightarrow Z/\gamma* \rightarrow ee/\mu\mu$, at leading order via $q\bar{q}$ annihilation is shown in Figure 2.7, and at higher orders with contributions from qg, qq and gg interactions, in Figure 2.8. Next to leading order diagrams also involve radiative corrections and initial state radiation. Processes that can be described by a Z exchange can also be described by a γ^* exchange, and the two processes interfere. In this thesis we mostly consider events in the region of the Z^0 pole, where the Z^0 exchange is dominating.

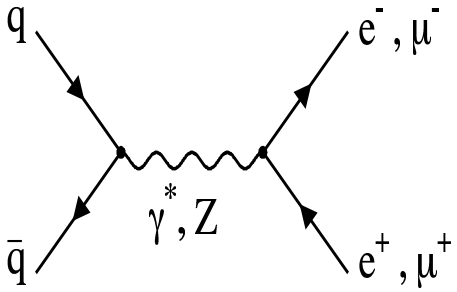

Figure 2.7: Leading order Z^0 production process, with the Z decaying to electron or muon pairs.

Just as in the case of $t\bar{t}$ and WW production, the cross section is dependent on the parton distribution functions of the protons and antiprotons in the Tevatron beam.

The use of the parton distributions functions is possible given that for Z production the momentum exchanged (Q^2) is very high, and thus the partons inside the protons and antiprotons can be considered asymptotically free. This in turn means that we can use a perturbative calculation at tree level for the short-distance cross section of the process.

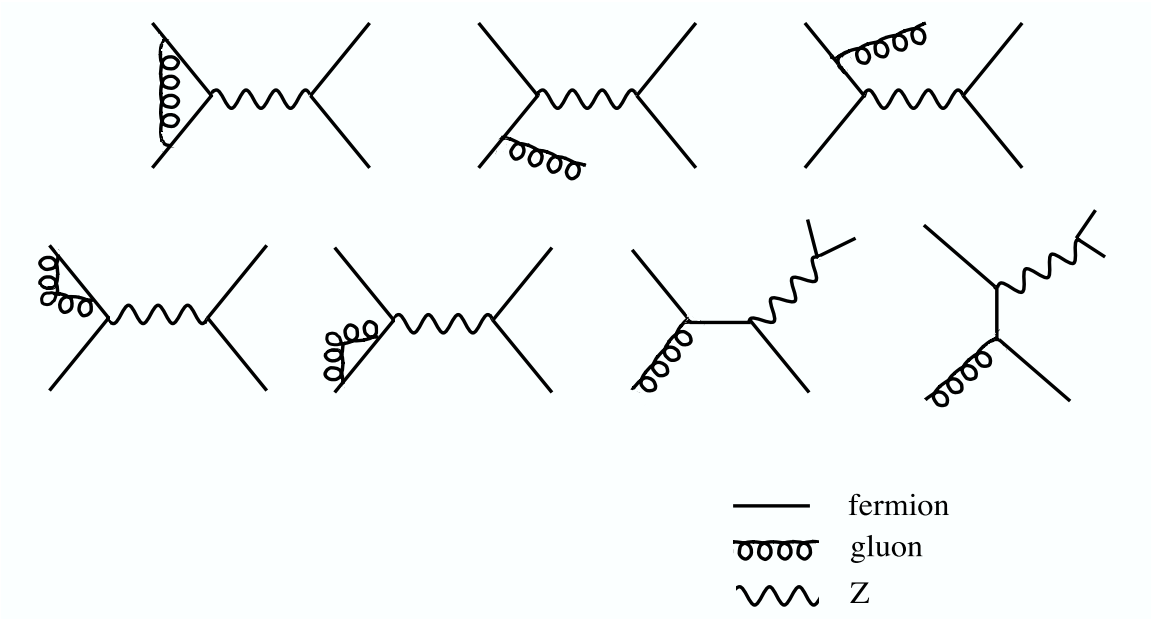

Figure 2.8: Some next to leading order (NLO) diagrams in the Z^0 production process.

The QCD perturbation expansion for Z^0 production is found to converge quickly. The next to leading order (NLO) and next to next to leading order (NNLO) contributions are about 16% and 2% respectively of the leading order (LO) cross section. The theoretical cross section for Z^0 production times the branching ratio to leptons, at the Tevatron center of mass energy, is $\sigma(p\bar{p} \rightarrow)BR(Z \rightarrow \ell\ell) = 250.4 \pm 5.0$ pb [39] for any lepton flavor ℓ. The latest experimental value for the mass of the Z is $m_Z = 91.1876 \pm 0.0021$ GeV [16].

The Z^0 boson can decay leptonically or hadronically. In Table 2.2 [16] we list the

main decay modes, where invisible decays means decays into neutrinos of any flavor.

Decay mode	Branching Ratio(experimental)
e^+e^-	$(3.363 \pm 0.004)\%$
$\mu^+\mu^-$	$(3.366 \pm 0.007)\%$
$\tau^+\tau^-$	$(3.370 \pm 0.008)\%$
hadrons	$(69.91 \pm 0.06)\%$
invisible	$(20.00 \pm 0.06)\%$

Table 2.2: The Z^0 decay experimental branching ratios.

In this analysis, Z^0 production enters our sample through its leptonic decays, with the $p\bar{p} \to Z^0 \to ee$ and $p\bar{p} \to Z^0 \to \mu\mu$ important backgrounds that we strive to cut through our event selection process. Since we do not identify τ leptons directly, the $p\bar{p} \to Z^0 \to \tau\tau$ process enters our sample only through the τ decays into electrons and muons, and is one of our main processes. In fact, as we will see, in this analysis, we measure $\sigma(p\bar{p} \to)BR(Z \to \tau\tau)$ in the channel where we observe one electron and one muon from the tau decays.

2.3 Experimental Cross Section Results to Date

As mentioned already, the top quark was discovered in the Tevatron Run I [24]. In Table 2.3 we summarize some of the published results from Run I and Run II for the $t\bar{t}$ cross section. The results of this analysis should be compared with the dilepton channel measurements, with similar luminosities. In Figure 2.9 we further summarize the $t\bar{t}$ cross section results, some of them yet to be published with about 750 pb^{-1} of integrated data luminosity. It should be noted that this analysis, which uses about 360 pb^{-1} of data, will be updated in the future with the full data available at CDF (about 1 fb^{-1} at the moment). In Figure 2.10 we further give the combined $t\bar{t}$ cross section results from each Run I and Run II as a function of the center of mass energy of proton-anti-proton collisions.

Experiment	Channel	$\sigma_{t\bar{t}}$	Int. Lum.
CDF-Run I [1]	dilepton	$8.2^{+3.8}_{-3.3}$ pb	109 pb^{-1}
CDF-Run I [40]	dilepton+lepton+jets	$7.6^{+1.8}_{-1.5}$ pb	109 pb^{-1}
CDF-Run II [3]	dilepton combined tight-tight and tight-track	$7.0^{+2.4}_{-2.1}(st)^{+1.6}_{-1.1}(sy) \pm 0.4$(lu) pb	184 pb^{-1}
CDF-Run II [41]	lepton+jets	$5.6^{+1.2}_{-1.1}(st+sy)^{+0.9}_{-0.6}(lu)$ pb	162 pb^{-1}
D0-Run II [42]	dilepton	$8.6^{+3.2}_{-2.7}(st) \pm 1.1(sy) \pm 0.6(lu)$ pb	230 pb^{-1}
D0-Run II [43]	lepton+jets	$8.6^{+1.6}_{-1.5}(st+sy) \pm 0.6(lu)$ pb	230 pb^{-1}

Table 2.3: Some of the published $t\bar{t}$ production cross section results.

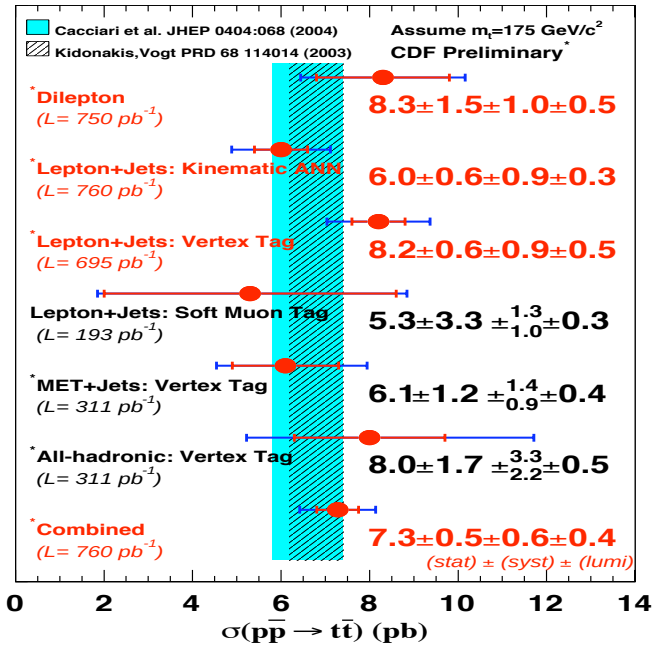

Figure 2.9: The summary and world average of $t\bar{t}$ production cross sections.

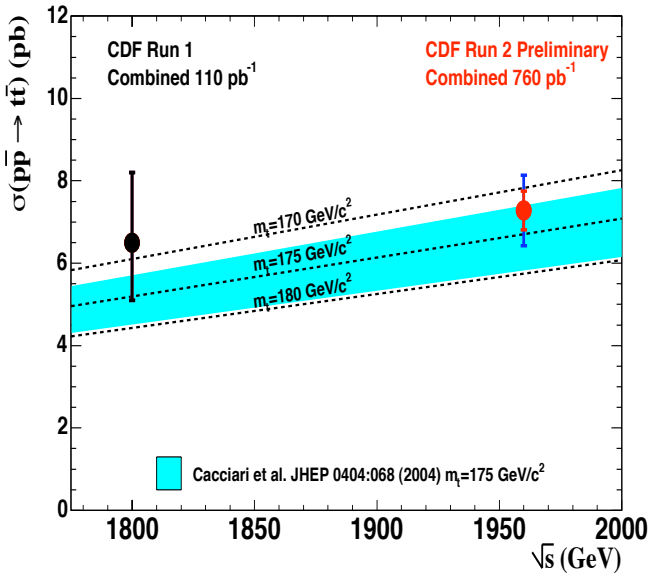

Figure 2.10: The $t\bar{t}$ CDF production combined cross section as a function of $\sqrt{s}$.

The $p\bar{p} \rightarrow WW$ cross section was first measured in CDF-run II [4], with the participation of the author of this thesis, in the dilepton decay channel. In Table 2.4 we summarize some of the WW cross section published results.

Experiment	Channel	σ_{WW}	Int. Lum.
CDF-Run II [4]	dilepton	$14.6^{+5.8}_{-5.1}(st)^{+1.8}_{-3.0}(sy) \pm 0.9(lu)$ pb	184 pb^{-1}
D0-Run II [44];	dilepton	$13.8^{+4.3}_{-3.8}(st)^{+1.2}_{-0.9}(sy) \pm 0.9(lu)$ pb.	230 pb^{-1}

Table 2.4: Some of the published WW production cross section results.

The best $p\bar{p} \rightarrow Z \rightarrow \tau\tau$ cross section, is the CDF Run II measurement to be published in the Physical Review D [45]; $263 \pm 23(stat) \pm 14(syst) \pm 15(lum)$ pb, with explicit tau-lepton identification being used. Our measurement represents a completely independent result, with a different methodology.

Chapter 3

The Experimental Setup

The experimental data for this research project was acquired at the Fermi National Accelerator Laboratory (Fermilab), located in Batavia, Illiois, just outside Chicago.

The instrument used was the Tevatron chain of particle accelerators, where protons and anti-protons collide at center of mass energies of $\sqrt{s} = 1.96$ TeV, which constitute the highest energy particle collisions achieved in any particle accelerator in the world. The detection device used was the collection of particle detectors known as the Collider Detector at Fermilab (CDF). In this chapter we will describe the most salient features of both the accelerator and the detection apparatus.

3.1 The Fermilab Tevatron

The Tevatron chain of particle accelerators is composed of several sub-components, which accelerate protons and anti-protons to higher and higher energies until reaching 1 TeV in the Tevatron ring, as is illustrated in Figure 3.1.

The Tevatron components are listed below:

1. The Proton Source
    - Cockcroft-Walton initial accelerator
    - The linac linear accelerator
    - Booster
2. The Anti-proton Source
    - Target

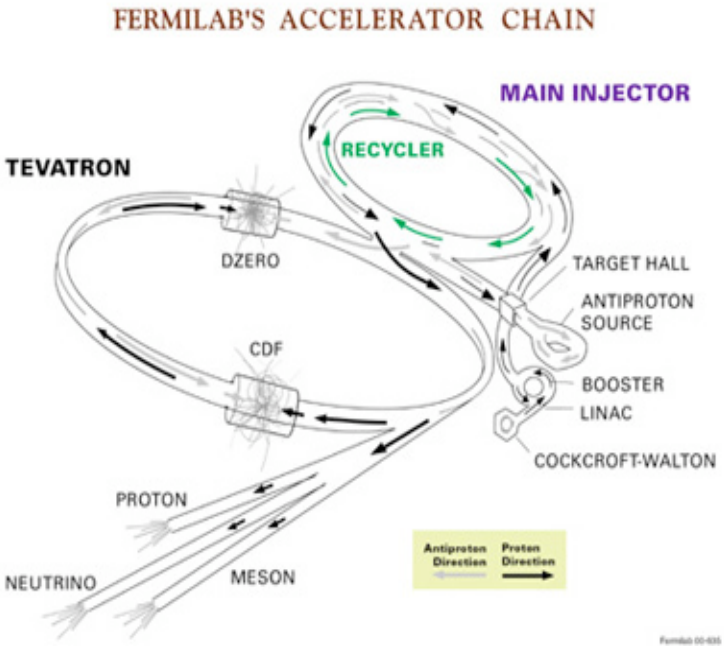

Figure 3.1: Schematic of accelerator components at Fermilab. Shown also are the locations of the main collider experiments, CDF and D0.

- Debuncher
- Accumulator
- Recycler

3. The Main Injector

4. The Tevatron Collider

We now briefly discuss each component.

3.1.1 The Proton Source

The initial source of protons for the accelerator chain is a container of hydrogen gas. The hydrogen atoms are negatively ionized, consisting of two electrons and one proton, then they are accelerated to 750 keV in the Cockcroft-Walton Pre-Accelerator.

This type of accelerator, first developed at the Cavendish Laboratory in Cambridge, England, is made of a series of capacitors that are charged in sequence, accelerating the charged ions in a straight vacuum pumped tube. Ionized hydrogen particles are produced every 66 milliseconds.

Then negatively charged hydrogen ions are injected in a linear accelerator (linac) approximately 500 feet long and their energy is boosted to 400 MeV. This type of accelerator, first developed by Ernest Lawrence, uses alternating electric fields and progressively longer sections of shielding conducting tubes to give a series of energy boosts to the charged ions. This operation is also done every 66 milliseconds, with an offset to catch the ions from the pre-accelerator. The particle beam is further focused using quadrupole magnets.

Before entering the third stage of acceleration, the hydrogen ions are made to pass through a carbon foil that strips the electrons, leaving only the positively charged protons. Then the protons are transfered to the Booster.

The Booster is a synchrotron (circular accelerator) composed of a series of 75 magnets arranged around a 75 meter radius circle. This synchrotron contains 18 RF cavities for providing the acceleration boost to the protons. The protons travel around the Booster approximately 20000 times until they reach energies of 8 GeV. This stage is also operated at 66 millisecond intervals with a phase offset to catch the ion bunches from the linac. After reaching 8 GeV energies, the protons are ready to be transfered to the Main Injector and then to the Tevatron for final acceleration and then collisions. The collected bunches of protons include about 6×10^{10} particles each.

3.1.2 The Main Injector

The Main Injector, has four functions;

1. Accelerates protons from 8 GeV to 150 GeV
2. Produces 120 GeV protons, which are used for anti-proton production
3. Receives anti-protons from the Anti-proton Source and increases their energy to 150 GeV
4. Injects protons and anti-protons into the Tevatron

Inside the Main Injector tunnel, also the Recycler is installed, which stores anti-protons that return from the Tevatron, and stores them to be re-injected into the Tevatron.

The Main Injector is a circular synchrotron of about half a kilometer in radius. It has 18 RF cavities that can accelerate proton bunches from 8 GeV to 150 GeV in 2.2 seconds. It also accelerates anti-protons from the Anti-proton Source to 150 GeV.

3.1.3 The Anti Proton Source

To produce anti-protons, 120 GeV protons incoming from the Main Injector are made to collide with a nickel target. The collisions produce a wide range of secondary particles including anti-protons. The particles created are sent through a magnetic field. Particles with different masses turn with different radii, and by using the radius expected for anti-proton masses, anti-protons are selected and separated. The resulting anti-protons have a wide range of momenta, with an average of 8 GeV, and are then transfered to the Debuncher.

The Debuncher is a triangular synchrotron with an mean radius of 90 meters. It can accept anti-protons with large momentum spread through the use of an RF manipulation technique called debunching and bunch rotation. Basically the RF voltage is reduced adiabatically over several synchrotron periods eventually turning off the voltage altogether, with the effect that the particles are distributed uniformly

over the whole path of the synchrotron (are debunched). Then the RF voltage is turned back on in a time much shorter than a synchrotron oscillation to its original value, this (bunch rotation) produces very narrow time spread bunches after just a quarter of a synchrotron period, however with a relatively wide transverse momentum spread. In order to reduce the transverse momentum spread, the so called Stochastic Cooling process is used. This 'cooling' process is done by reading the electromagnetic pulses generated in one end of the beam. This signal is shorted to a later point in the beam where the oscillation is in average opposite. With this signal, magnetic fields are adjusted with the effect of decreasing the transverse momentum of particles in the beam.

These 'cooled' anti-protons are then injected into the Accumulator at 8 GeV with small momentum spread. The Accumulator is a rounded triangular synchrotron in the same tunnel as the Debuncher, where anti-protons are collected until the desired number of anti-protons is stored, and then the particles are transfered back to the Main Injector and then the Tevatron.

3.1.4 The Tevatron

The Tevatron ring, with a radius of about 1 km, is where protons and anti-protons are accelerated from 150 GeV to the final 980 GeV and collided at two main locations. Thirty six bunches of both protons and anti-protons are inserted, accelerated with 8 RF cavities for approximately 85 seconds, and collided at both the CDF and D0 detector locations. The RF cavities are made with superconducting niobium/titanium alloy magnets and cryogenically cooled to 4K in order to maintain superconductivity and reach the desired magnetic fields. Other magnets contained in the ring are quadrupole magnets for focusing and dipole magnets for producing the approximately circular beam path.

In order to produce a high density beam for collisions, the beams are focused with quadrupole magnets into 32 μm in diameter at both the CDF and D0 locations. Once the Tevatron is loaded with the proton and anti-proton bunches it can sustain collisions for several hours, with the number of collisions decreasing with time. After dropping below an efficient number of collisions, the Tevatron is loaded with new bunches again.

The number of collisions per second is described by the luminosity. The quality and breath of the physics research attainable at both the CDF and D0 detectors is highly dependent on achieving high enough luminosities, so a lot of effort is directed to minimize losses of the beam, inserting bunches with a high number of protons and anti-protons, and focusing of the beams.

3.1.5 Measuring The Luminosity

The luminosity in collider experiments is a measure of the beam flux. In CDF a Cherenkov type detector serves to monitor the luminosity. Luminosity, given in units of 1/Area, is given by;

$$L = \frac{fBN_pN_{\bar{p}}}{2\pi(\sigma_p^2 + \sigma_{\bar{p}}^2)} \times F(\sigma_l/\beta^*) \tag{3.1}$$

where f is the revolution frequency in Hertz, B is the number of bunches, $N_{p/\bar{p}}$ is the number of protons/anti-protons per bunch and $\sigma_{p/\bar{p}}$ is the root mean square of the beam size at the interaction point. The multiplicative factor F is a form factor that depends on the ratio of the longitudinal bunch length to the transverse beam direction.

In Figure 3.2 we can see the total delivered and recorded integrated luminosity up to date at the CDF detector. For this analysis we use 360pb^{-1} of data.

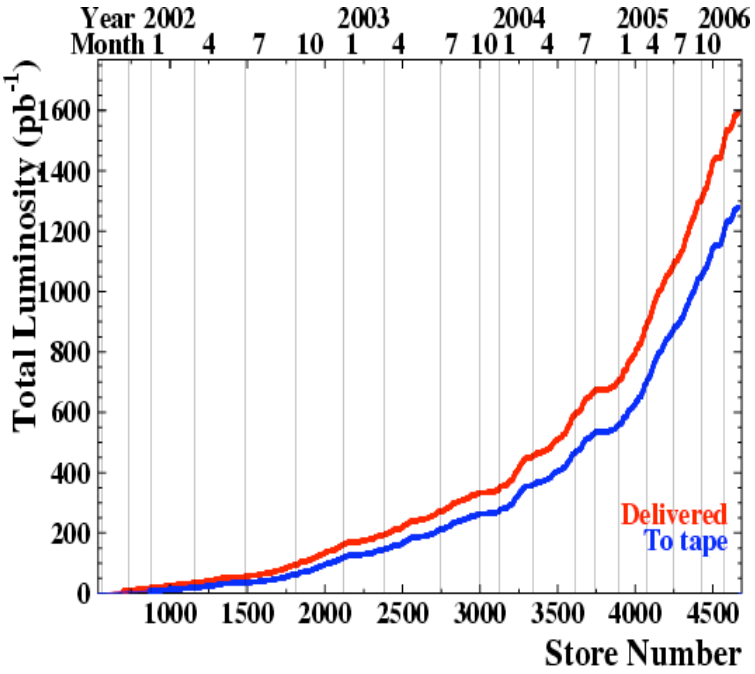

Figure 3.2: Total delivered and recorded luminosity at CDF, up until January 2006

3.2 The CDF Run II Detector

The Collider Detector at Fermilab (CDF), is a complex collection of apparatuses designed to detect the particles resultant from the collisions generated by the Tevatron accelerator. Most of these components were upgraded from Run I for the current Run II to handle the higher luminosity yield. The detector is designed with symmetrical components in the beam and azimuthal directions. In Figure 3.3 we show a schematic view of the CDF detector.

The components of the detector are grouped according to their function. Enveloping the beam is first the tracking system; innermost is the silicon detector and then a wire drift chamber, which are designed to track the path of charged particle and measure their momentum. The Tracking systen is inside a 1.4 T solenoidal magnetic field. Then outside the tracking volume lies the calorimeter, designed to measure the energy of particles brought to rest in its volume. Finally, the outermost detectors are

drift chambers for muon detection.

In the next few sections, we will briefly describe the main components of the detector in more detail, but first we introduce the CDF geometrical coordinate convention.

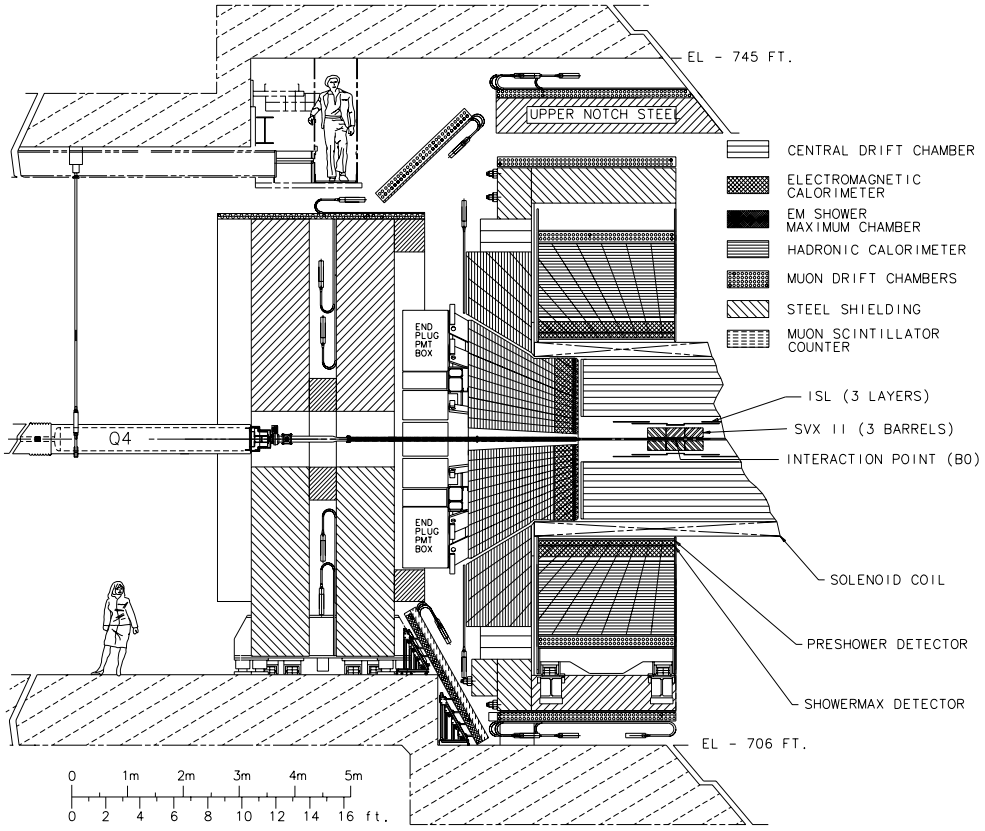

Figure 3.3: A cut-away view of the CDF detector. Only half the calorimeters and muon detectors are shown.

3.2.1 Geometrical Coordinate System

In Figure 3.4 we can see the coordinate convention adopted in the CDF detector. In the CDF cylindrical coordinates the z coordinate is taken in the direction of the proton beam, increasing in the east direction. The y coordinate lies in the vertical direction going up, and the x coordinate is oriented radially increasing in the outward

direction. The azimuthal angle ϕ is measured from the x direction, towards the y direction, and the polar angle θ is taken from the positive z axis. The r coordinate is defined as $r = z \times cos(\theta)$.

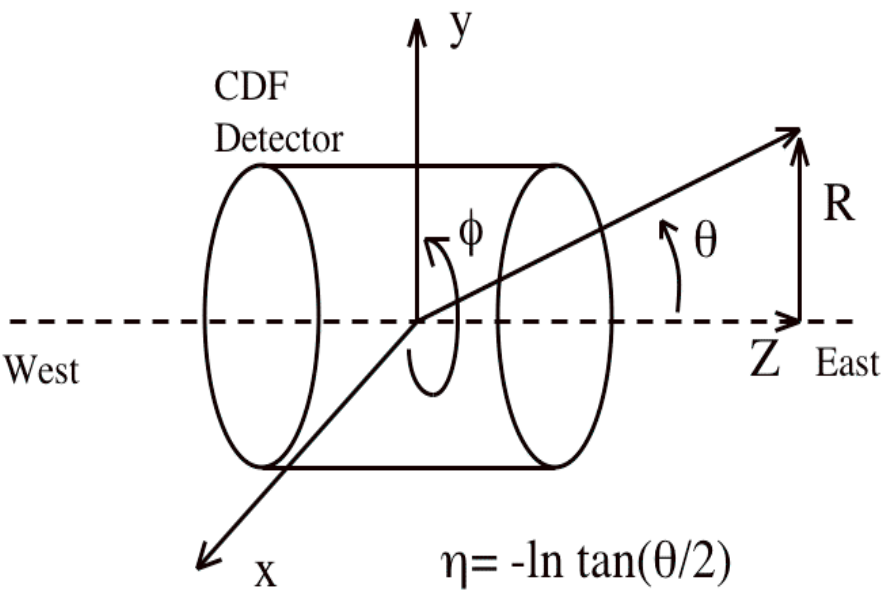

Figure 3.4: CDF Coordinate System.

The coordinate given by θ is not a Lorentz invariant. Then, the number of particles per unit angle will not be the same for particles with different velocity. Instead we define the rapidity as;

$$Y = \frac{1}{2} ln \frac{E + p_z}{E - p_z} \tag{3.2}$$

For a massless particle (or $p \gg m$), the rapidity can be approximated by the

pseudo-rapidity, given below;

$$\eta = -ln\ tan(\theta/2) \tag{3.3}$$

As a result the number of particles per unit rapidity is invariant under Lorentz transformations in the z direction.

3.2.2 The Tracking System

The trajectory of particles in the presence of a magnetic field gives information about the original kinematical quantities. Specifically the direction of the curvature of the trajectory gives particle charge information, and the radius of curvature gives momentum information. The magnetic field is provided by the CDF Solenoid. The process of reconstructing the trajectory of a particle is known as tracking. The detectors that provide the tracking information are the silicon detectors (SVX and ISL) and the Central Outer Tracker (COT). In Figure 3.5 we see a schematic view of the tracking volumes.

All tracking detector volumes are contained within the magnetic field provided by the Solenoid. The Solenoid produces a very homogeneous magnetic field of 1.4 Tesla inside a usable volume of 2.8 m in diameter and 3.5 m in the z direction.

The Silicon Vertex Detectors

The Silicon Vertex Detector is the innermost of all CDF particle detectors. It is actually composed of three groups, the L00, SVX [46] and ISL detectors [47]. The three groups differ in size, radius and number of active elements, but they all use the same silicon micro-strip technology. The main tracking detector is the COT, but the silicon detector provides precision position measurements that enable us to study secondary vertexes like those produced in the decay of long lived mesons with

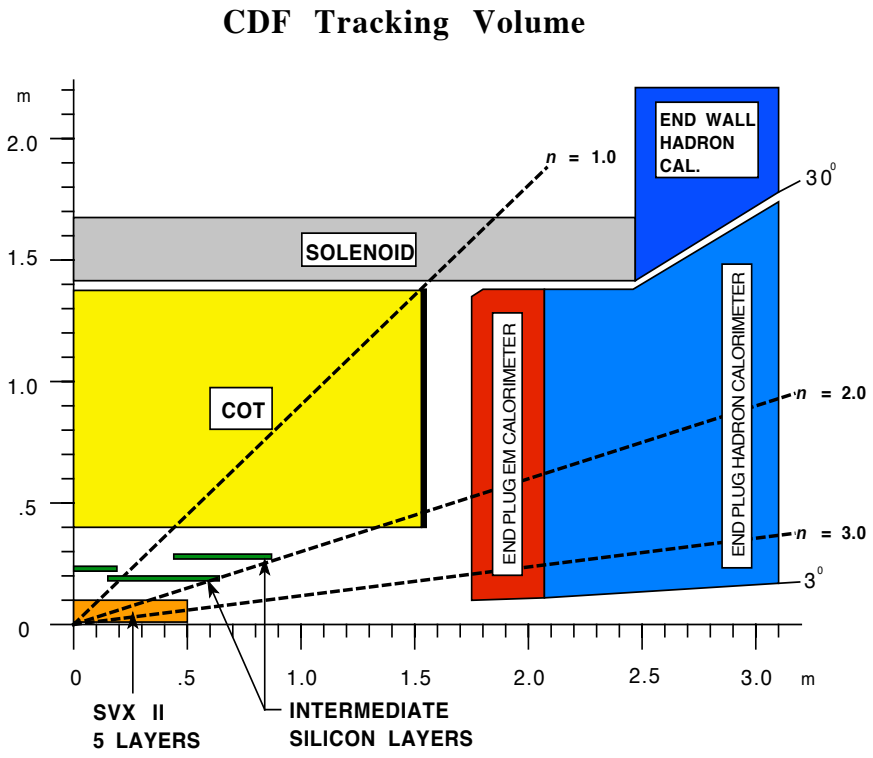

Figure 3.5: General Layout of the tracking volumes.

an excellent resolution. In fact, about 10 times more resolution is attainable in the silicon detectors than in the COT. In Figure 3.6 we can see a transverse view of the three groups of silicon detectors, from the L00, which is right on the beam pipe tube, with single sided silicon strips, to the SVX and the Intermediate Silicon Layers (ISL) both groups of double sided silicon strips. The detector is arranged in three barrels linearly placed along the beam axis which include these constituent components.

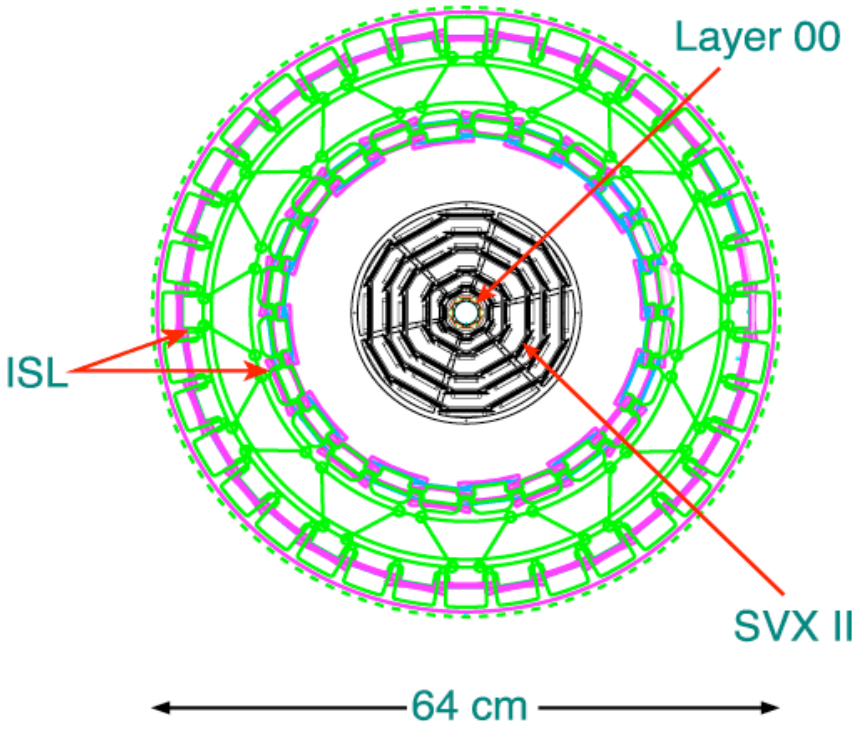

Figure 3.6: End view of the silicon tracking system.

The CDF silicon detectors rely on the electron hole pairs that are produced by the passage of charged particles through the silicon. These electron hole pairs drift under electric currents and are collected in conductor strips. However, in pure silicon the typical amounts of ionization charge produced by passing particles is about four orders of magnitude smaller than the natural charge carriers present in the silicon. This leads to the need to deplete the silicon of the native charge carriers with the use

of pn junctions. These junctions use contaminated samples of silicon.

The n type silicon is obtained through the addition of Phosphorous or Arsenic ions. These ions change the energy level so it is close the the conduction band, which results in the majority of carriers being electrons. In the case of the p type silicon, Boron ions are added, which change the energy level close to the valence band, leaving the majority of carriers as holes. In a pn junction, the majority charge carriers migrate out of the junction, leaving a net positive and negative charge on each side of the junction but also depleted of majority charge carriers. This is known as the depletion zone. In the depletion zone the electron hole pairs that are produced by passing particles, drift along the electric field lines generated by the net charges. The depletion zone is further enlarged with the application of a voltage difference across the junction.

The CDF silicon detectors use highly doped p type and lightly doped n type silicon. The bulk of the detectors is made of the n type silicon which is where the depletion zone mostly extends, allowing the electron hole pairs to drift and be collected in thin conducting strips. The innermost component is the layer 00 (L00) which is a single sided silicon strip detector mounted right on top of the beam pipe. Then the SVX detector just outside it, is composed of five layers arranged in wedges around the ϕ direction. The first second and fourth layers are double sided with the strips on each side at 90 degrees to each other, the distance between the strips is 60 μm on the side that has the strips aligned along the ϕ direction, and 141 μm on the side that has the strips aligned in the z direction. The third and fourth layers are also double sided but with one of the sides aligned with the z axis and the other side strips at a 1.2 degree angle to the z axis. The purpose of having these small angle configuration layers is to avoid possible fake hits that can be mis-identified with real particle hits when there are multiple strip signals in the 90 degree angle layers. The

distances between conducting charge collecting strips in this small angle layers is 65 μm in both sides. The SVX detector layers radii range from 2.4 to 10.7 cm from the beam. To hold the layers in place a low mass substrate is used to minimize interaction with the incoming particles. Finally, the Intermediate Silicon Layers (ISL) is situated enveloping the SVX detectors, and is composed of two layers of small angled double sided silicon strip detectors. In the ISL the distance between readout strips depends on the layer and the side, but goes from 55 μm to 146 μm. The three silicon detector groups are arranged in three barrels of a total length of 96 cm.

The silicon detector tracking system provides a more extended angular coverage than the Central Outer Tracker, while the COT reaches up to a pseudo rapidity (η) of 1.0, the silicon detectors extends up to an η of 2.0. As a result in the region $1 < \eta < 2$ the only source of tracking information are the silicon detectors.

The Central Outer Tracker

The COT [48] is the main tracking device at CDF, used to detect and reconstruct the three dimensional trajectories of centrally traveling particles. . It can track charged particles in the pseudo-rapidity range of $-1 < \eta < 1$. The detector is a cell drift chamber design. Drift chambers rely on the property of certain gasses under pressure to produce ions when charged particles pass through. Then the ions travel (drift) under the effect of electric fields produced by conducting wires and plates, and are collected in sensor wires.

The CDF drift chamber, known as the COT, is composed of cells of conducting wires and plates arranged into so called superlayers, see Figure 3.7. The detector extends from a radii or 44 to 132 cm from the beam axis, and with a length of 310 cm along the z axis.

The COT drift chamber cells contain each 12 sensor and 12 potential gold plated

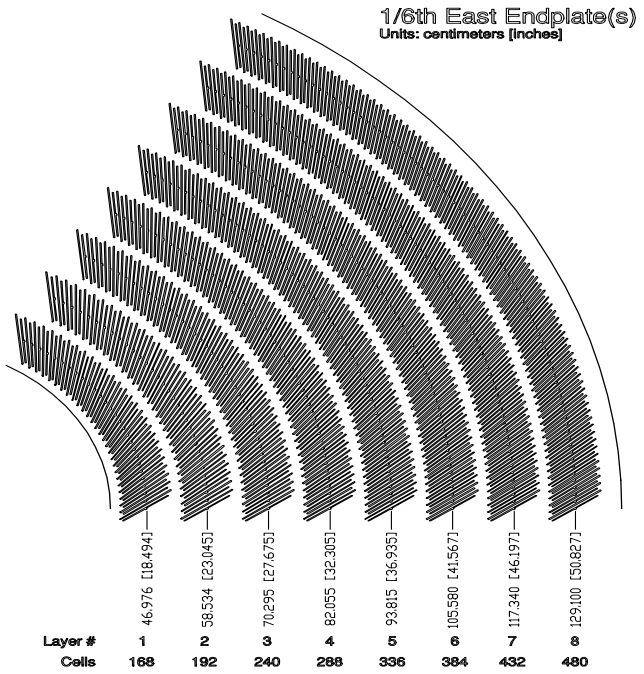

Figure 3.7: End view of the layer and superlayers in the Central Outer Tracker.

tungsten wires spaced 3.8 mm apart. These are placed between gold on mylar cathodes separated by 2 cm and end cell shaper wires, which shape the electric fields in such a way that no drift ions escape the cell, see Figure 3.8 for the cell schematic arrangement.

Four of the COT superlayers are placed so that the wires follow the z axis direction, and four superlayers have the wires at a ± 3 degree angle to the z axis. The superlayers are placed so that they alternate between wire orientation. The gas mixture used is $Ar - Ethane - CF_4$ at a 50:35:15 proportion. This gas mixture allows for fast drift times in the COT cell geometry of a maximum of 100 ns, which is faster than the time between proton anti-proton bunch collisions. The low material content and gas properties of the COT allow for a low ratio of particle trajectory length to radiation length, of about 1.69%.

Because of the effect of the 1.4 T magnetic field provided by the solenoid, the

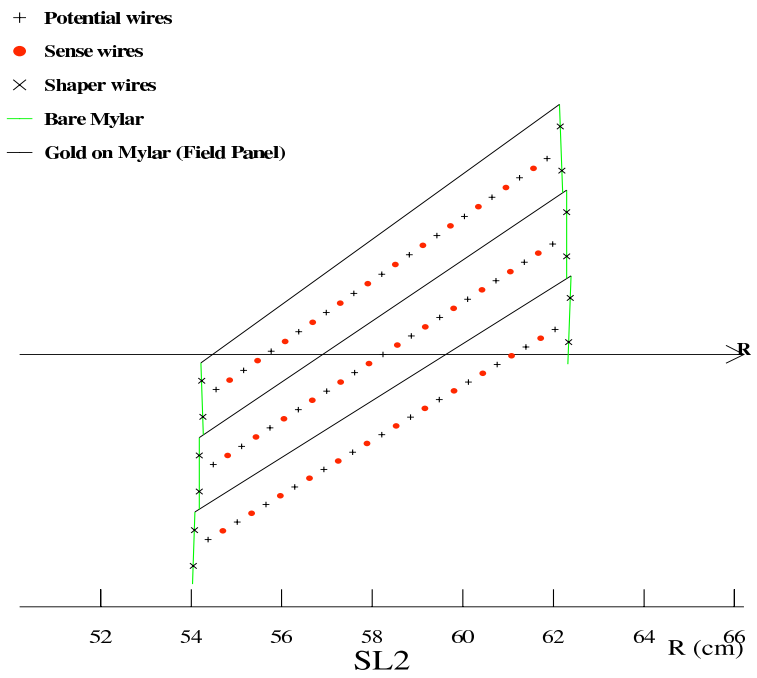

Figure 3.8: End view of the individual cell layout, of the Central Outer Tracker.

trajectories of particles detected in the COT allow for determining the charge and momentum of the particles. We discuss later how the transverse to the beam direction projection of the energy and momentum quantities is more relevant and accurate for our kinematical reconstruction of collision events. To define transverse projections of the helical particle trajectories we use five parameters, defined with respect to the track vertex, which is the track position closest to the z axis;

- Curvature; is defined as $(2 \times r)^{-1}$, where r is the radius of the track. The sign of curvature is determined by the path of the track in the x-y plane, with clockwise tracks denoted by negative curvature, while counter clockwise tracks are positive. The track transverse momentum, p_T is related to the curvature by $p_t = Bq/2c$, where B is the magnetic field, q is the charge of the particle and c is the track curvature.

- d_0; the impact parameter, is defined as the distance between the track vertex

and the z axis in the transverse direction. The sign of d_0 is defined as opposite the track angular momentum about the z axis.

- z_0 is the z position of the track vertex.
- $cot\theta$ is the cotangent of the angle the track makes with the z axis.
- ϕ_0 is the ϕ direction of the track in the x-y plane at the track vertex.

3.2.3 Calorimetry

The calorimeter system is designed to measure the energies of the particles produced in the proton-anti-proton collisions. It is divided in two sub-detectors; the Central Calorimeter, which covers the pseudorapidity range of $-1 < \eta < 1$, and the Plug Calorimeter, which covers both the positive and negative pseudo rapidity $1.1 < \eta < 3.6$ regions.

Both the central and plug calorimeters are composed of alternating layers of lead and sensing layers (scintillators). The lead layers have the effect of producing a particle shower from the interaction of the material with the incoming particles. The sensing layers are scintillators that produce a proportional number of photons to the particles that go through them. The light is collected through light guides and channeled to photomultipliers where it is counted. By analyzing the amount of light that reaches the photomultipliers tied to each scintillator layer it is possible to map the profile of the number of particles in the shower as a function of scintillator layer.

These calorimeter detectors have a different response depending on whether the incoming particles are electrons, photons or hadrons. In the case of photons and electrons a combination of the effects of bremsstrahlung and pair production results in the occurrence of a cascade of showers. A parent electron will radiate photons, which convert to e^+e^- pairs, which in turn radiate and produce pairs. This results

in an exponential increase in the number of particles in the cascade. The competing effects are from ionization loss and from the dependence of the pair production cross section on the particle's energy. As a result of these competing effects as the energy of individual cascade particles decreases and more energy is lost to ionization loss in the material, the cascade stops growing in number of particles and it eventually decreases and gets extinguished.

For electron and photon showers the maximum number of particles in the shower occurs at a distance that is proportional to the initial primary particle energy. In CDF, by identifying the distance to the point where the shower is at its maximum number of particles, the energy of the primary particle can be measured.

In the case of hadrons, a different type of process creates a shower. An incident hadron collides inelastically with the calorimeter material and creates secondary hadrons, which again interact inelastically and further produce more hadrons, creating a cascade. The scale for longitudinal development of the shower is set by the nuclear absorption length of the calorimeter material. In heavy elements such as iron, the nuclear absorption length is bigger than the radiation length which plays a role in electron and photon showers. As a result a hadron would produce a longer shower profile than electrons or photons. The process through which the hadron shower diminishes is also different from the electron and photon (Electromagnetic) showers. While the ionization loss also provides the biggest energy loss, about 30% of the primary hadron energy is lost by the breakup of nuclei, nuclear excitation and evaporation of neutrons and protons. Nevertheless the shower maximum distance for hadronic showers is proportional to the primary hadron energy.

Because of the different profiles of hadron and electromagnetic showers, both the central and plug calorimeters are composed of two sections. A section that measures electromagnetic showers and a much larger section outside that is optimized

for measuring hadronic showers.

The Central Calorimeter

The central calorimeter is a cylinder located outside the COT. The detector consists of two barrels which meet in the center at $z = 0$. Each barrel is made of 24 wedges. The central calorimeter provides full 2π azimuthal coverage, with the exception of the gaps between the wedges and the so called chimney, which is a gap where the cryogenic connections to the solenoid are channeled through. Each wedge spans 15 degrees and is segmented in 10 so called towers, each spanning an η of 0.11. In Figure 3.9 we can see a schematic view of the central calorimeter wedges.

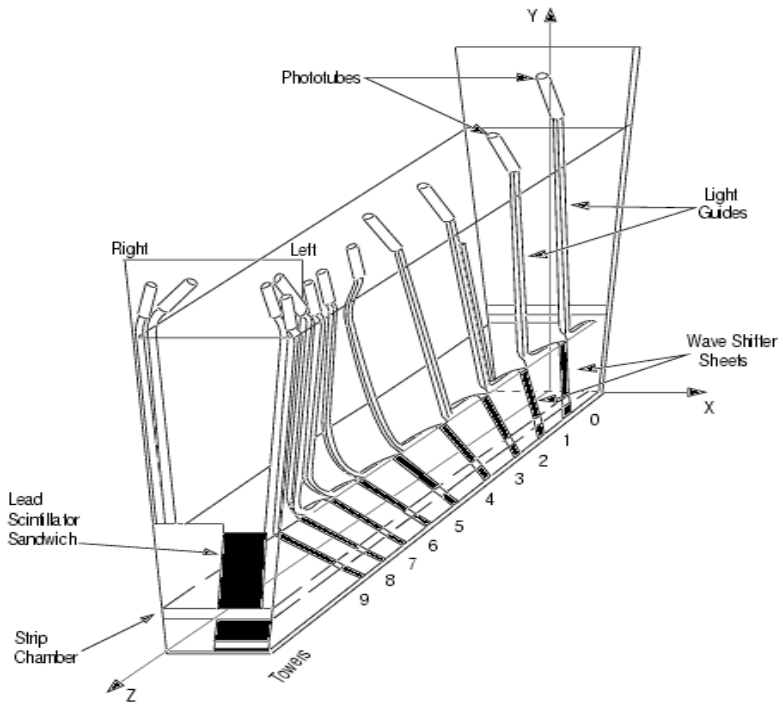

Figure 3.9: Schematic view of a Central Calorimeter Wedge

In the electromagnetic central calorimeter [49] lead is used as an absorbing material. There are 30 layers of 3.2 mm lead which are alternated with 31 layers of 5

mm scintillator. The electromagnetic system has a depth of 19 radiation lengths. At about the point of the maximum of the shower, is the Central Electromagnetic Shower max detector(CES). The purpose of the CES is to measure the position and shape of the electromagnetic shower maximum with a precision of 2 mm. The CES is a proportional drift chamber. The chamber gas used is 95 % argon and 5 % carbon dioxide. The CES is made of 64 anode wires in the z direction, and 128 cathode strips in a direction perpendicular to the beam. The wires measure the local detector x position and the strips the z position. The transverse shape of the shower further helps distinguish between the electromagnetic and hadronic showers. The CES positions are further useful for associating the showers with particle tracks from the COT.

On each wedge outside the electromagnetic calorimeter, the Hadronic Calorimeter is placed. It is composed of alternating layers of 2.5 cm iron and 1.0 cm thick scintillator. Just as the electromagnetic calorimeter, the hadronic calorimeter [50] measures the profile of the hadronic showers. There is additionally the Wall hadron calorimeter. With the same material components as the hadronic calorimeter and filling the gap between the central and the plug calorimeters.

The Forward Plug Calorimeter

In Figure 3.10 we have a schematic side view of the plug calorimeter. The plug calorimeter is also made of an electromagnetic and a hadronic shower detectors. The coverage area extends to both sides in a pseudorapidity window of $1.1 < \eta < 3.6$. The electromagnetic and hadronic detectors are housed in the same triangularly shaped wedge. The $\eta - \phi$ fragmentation is kept as much like the central detectors as possible. The electromagnetic type detector is composed of 23 4.5 mm layers of lead interposed with 4 mm thick scintillator. This design corresponds to 21 radiation

lengths of material. The scintillator light is collected in multi anode photomultiplier tubes. The hadron shower calorimeter is composed of 23 layers of 2 inch iron and 6 mm thick scintillator.

At a depth of about 6 radiation lengths, in the electromagnetic calorimeter, is situated the Shower Maximum Detector (SMD). This has the purpose of measuring the shape and position of the electromagnetic shower maximum and to distinguish further electromagnetic from hadronic showers. The SMD has a positioning resolution of about 1 mm, it is composed of two layers of sensing wires spaced 5 mm apart at 45 degrees to each other. The SMD is the forward calorimeter equivalent to the CES.

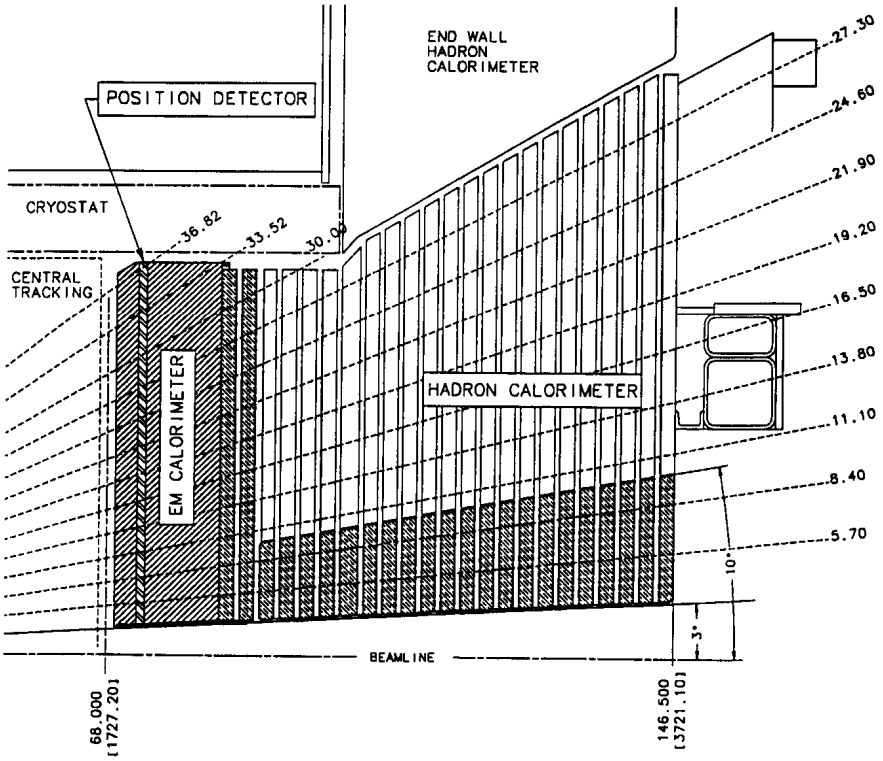

Figure 3.10: Schematic side view of the Plug Calorimeter

3.2.4 The Muon Detection System

In CDF, muons are identified thanks to their ability to penetrate large quantities of material better than the other charged particles, and their momentum is determined from the trajectories of their track under the solenoid field effect. The muon detectors [51] are placed outside all other detector components and hits in those are matched with tracks identified by the tracking devices. In Figure 3.11 we can see the $\eta - \phi$ coverage of the various components of the muon detector system, the CMP, CMX and CMU detectors.

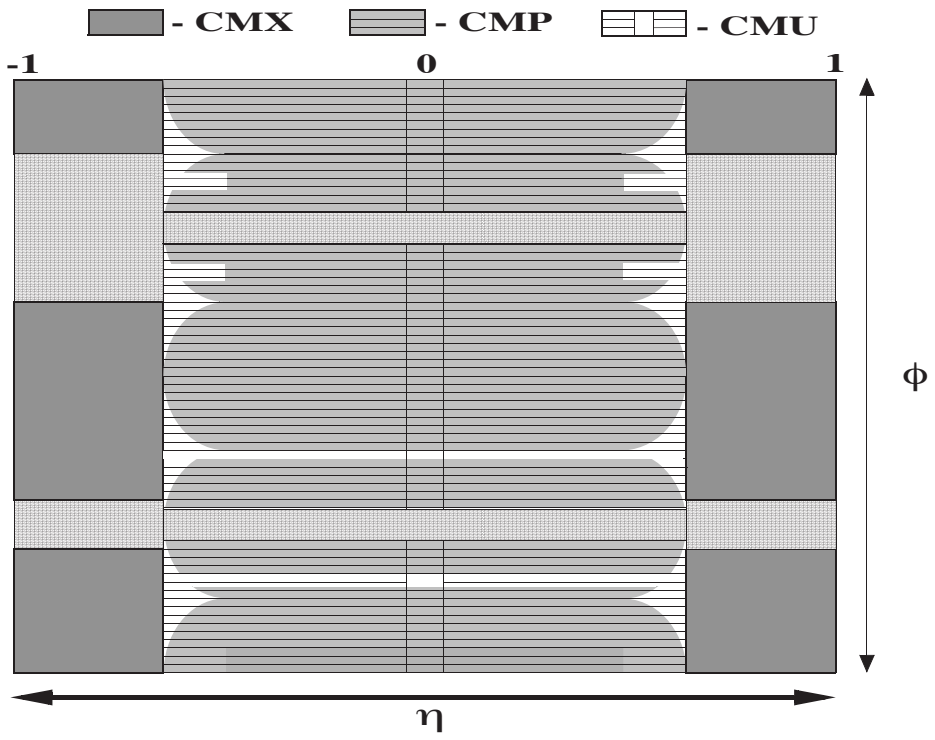

Figure 3.11: The $\eta - \phi$ view of the components of the muon detection system.

The Central Muon Detector (CMU) is a set of 144 modules with 16 rectangular cells per module, located behind a great deal of material, given that the particles

have to go through the central hadron calorimeter to reach it. The detector is made of drift chambers cells of $6.35 \times 2.68 \times 266\ cm$ in size and a single 50 μm stainless steel wire in the center. The ϕ and z muon locations are determined from each cell with the use of a charge counter that depends on the distance the particle passed from the wire and the cell end plates. The position determination is necessary to match the muons detected in the drift chamber with track from the main tracking detectors.

The Central Muon Upgrade (CMP) consists of a second set of muon chambers behind an additional 60 cm of steel in the region $55 < \theta < 90$ degrees. The chambers are of fixed length in z and form a box around the central detector. The pseudorapidity coverage varies with the azimuthal angle as shown in Figure 3.11. Components of the solenoid system provide enough steel above and below the central region, but steel was added to the two sides in the form of two non-magnetized retractable walls. The CMP chambers are rectangular, single wire drift tubes configured in four staggered layers. The tubes are made of aluminum, having a single sensing wire in the center, and field shaping cathode strips on the top and bottom. They are typically of dimensions given by $25 \times 15 \times 640\ cm$. A layer of scintillation counters (CSP) is installed on the outside surface of the wall of the drift chambers. Each scintillation counter covers two chambers in width and half in length.

The Central Muon Extension (CMX) consists of conical sections of drift tubes and scintillation counters (CSX) located at each end of the central detector and extending in θ from 42 to 55 degrees. At 55 degrees the CMX/CSX system slightly overlaps the coverage of the central muon system. With this system the pseudo rapidity coverage is extended to $\eta < 1$. There is no extra steel added for this detector, but because of the large angle of incidence on the hadron calorimeter, material of the solenoid system and the steel of the detector support structure, there is on average higher amount of

material in the way of muons to reach the CMX than central muon chambers. For each 15 degree ϕ sector, there are twelve tubes with four staggered layers, with each layer partially overlapping each other. The drift tubes of the CMX differ from those of the CMP only in length, being 180 cm long. The CSX scintillation counters are installed both on the inside and the outside surfaces of each 15 degree CMX sector.

3.3 Trigger and Data Taking

The rate of $p\bar{p}$ collisions is much higher than the rate with which the event data can be stored. However, most of these collisions are soft and result in uninteresting final particle states. As a result there is a need for selecting interesting events for storage and further studies on the fly. The system that performs this task is known as the trigger system. The trigger system is designed in three stages each, with the purpose of reducing the number of events with a minimum dead time from processing as possible. After the trigger selection, various collections of events are selected and labeled following criterion from the different physics groups in CDF.

3.3.1 Level 1

The first selection of events is done by the Level 1 trigger. This trigger filters out the vast majority of the events with uninteresting physics at a decision time of 5.5 μs. The level 1 hardware identifies physics objects with three parallel synchronous systems that feed the information to a decision unit. One stream looks at calorimeter objects such as electrons and photons, another uses muon information, and the third, the extra fast tracker (XFT), finds tracks in the central tracking system. The level 1 trigger elements are synchronized to 360 ns, with a level 1 trigger every 360 ns. Then the surviving events are fed into the Level 2 trigger. The accept rate of the level 1 trigger is about 25 kHz.

3.3.2 Level 2

The Level 2 trigger takes more time and adds more information to take a further decision on events. The Level 2 adds CES and SVX information to Level 1 objects, and increases the precision of Level 1 object cuts. The cuts applied are programmable and determined by the various physics groups. There are four buffers that analyze the events that pass the Level 1 trigger, each buffer can only examine one event at a time, if all four buffers are occupied dead time can occur. To avoid this problem the level 2 decision time is about 80 % that of the Level 1 accept rate.

3.3.3 Level 3

The Level 3 trigger uses the full detector resolution and reconstructs the events in a computer farm system. In the Level 1 and Level 2 triggers, pre-selected rough information is used to quickly reduce the number of events. In the level 3 the full event reconstruction is used, the same reconstruction as used in offline data that will be discussed in the next section. With the fully reconstructed event it is possible to make very precise qualitative and quantitative cuts on the events. The final accept rate of the level 3 trigger is about 50 Hz.

3.3.4 Offline Data Processing and Datasets

The process of obtaining data through Tevatron collisions is divided into three main steps from the CDF detector point of view;

- **Setup:** This embodies reading the hardware and electronics for data taking. Such as initializing the electronics settings, ramping up voltages, loading calibration parameters and so on.

- **Data Taking:** This is mostly an automatic process. In principle it can continue as long as the luminosity is deemed efficient for data taking or the accelerator store is interrupted. However many times other issues such as detector hardware or software problems interrupt the taking of data. One set of continuous data taking period is know as a run, which increases in unity every time the detector is setup for collection of data.

- **Production:** Once the data is filtered by the trigger and stored on tape, it must be processed with the CDF software package in a computing intensive process to unpack the data blocks and reconstruct physics objects such as leptons and hadronic jets. This can be repeated if improvements in the processing software are made.

In the production process the data is divided into various datasets, further filtering is applied, and the results are the primary datasets optimized for studies by each physics group. The list of datasets used by our analysis is listed in Table 3.1.

Dataset	Description
bhel08	at least 1 electron
bhel09	at least 1 electron
bhmu08	at least 1 muon
bhmu09	at least 1 muon

Table 3.1: Datasets used in this thesis project.

The so called tight electron sample, that passes very strict electron identification cuts, is obtained from the bhel08 and bhel09 datasets. These samples pass a number of cuts that in essence require at least one electron to be present.

In the same way, the tight muon sample is obtained from the bhmu08 and bhmu09 datasets, where very strict muon identification is required. This sample requires hits in the CMU, CMP or CMX detector systems, with the hits matching to a COT track with momentum greater than 18 GeV.

In the next chapter we will go in detail over the cuts applied to select tight electrons and muons. The total integrated luminosity of the samples used for the set of results presented in this thesis is about 360 pb^{-1}

3.4 The Detector Simulation

In order to simulate the effects of physics processes in the CDF detector a simulation procedure is followed. First a Monte Carlo program such as Pythia [52] and Herwig [53] is used to generate a chosen physics process and provide the resulting kinematics at all final-state particles. Particles are then propagated through a GEANT [54] based detector simulation. This simulation provides all the reconstructed variables seen in data and as a result we analyze the simulated data as if it was a real data sample that has gone through the production process. This includes detector component responses and resolutions. This allows us to make detailed comparisons of expectations with the data. The detector simulation program is an evolving piece of code with successive improvements made on various simulation aspects. One of the tasks the author of this thesis was assigned to in CDF, was the improvement and implementation of a fast simulation model for emulating the silicon detector response in Monte Carlo physics samples.

Chapter 4

Particle Identification

In this chapter the principles of particle identification will be presented. The main objects in this analysis are electrons, muons, hadronic jets and missing energy that is attributed mainly to neutrinos. The identification of the particles is done by applying a series of cuts on detector reconstructed variables.

4.1 The Particle Traces in the Detector

In Figure 4.1 we see how various particles look like in the detector. Electrons leave a track in the SVX and COT and a shower in the Electromagnetic Calorimeter. Photons, while creating also a shower in the electromagnetic calorimeter, leave no trace in the tracking system due to their lack of electric charge. Hadronic jets leave tracks in the SVX and COT, and deposit energy in both the Electromagnetic Calorimeter and Hadronic Calorimeter. Muons leave tracks in the COT and SVX, only a small fraction of their energy in the electromagnetic and hadronic calorimeters due to their minimum ionizing nature, and leave hits in the muon detector drift chambers. Finally neutrinos, being so weakly interacting, leave no traces at all and manifest themselves indirectly as missing energy in the event.

As was discussed in Chapter 2, the parton distribution functions (PDFs) play a role in making the momentum of collisions of the individual quark constituents of protons and anti-protons, along the direction of the beam, to be not precisely determined. As a result we use the transverse plane to the direction of the beam to describe most of our momentum quantities, where the initial total value is approximately zero, and so by using momentum conservation in the transverse plane we can

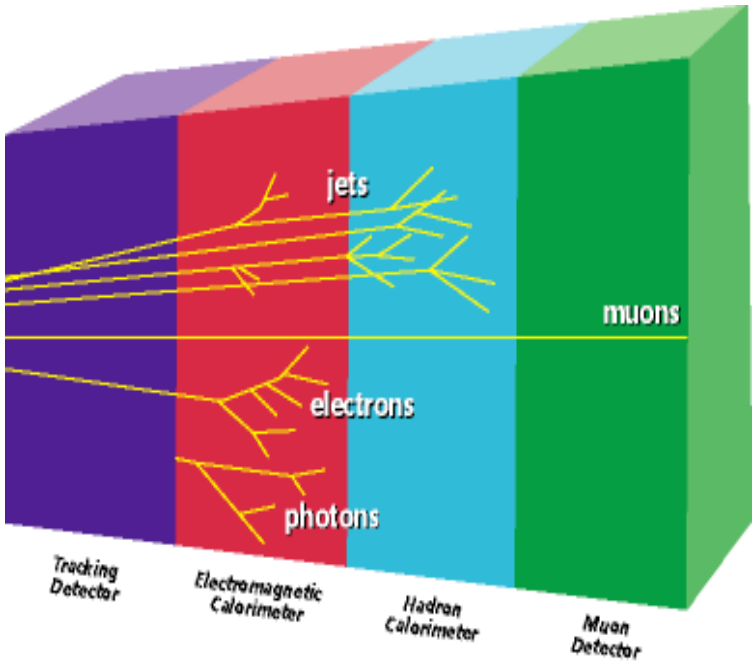

Figure 4.1: Schematic of how different particles look like in the detector

find the missing transverse energy due to neutrinos in the event. As a general rule the T subscript signifies the transverse plane: P_T is the momentum projection in the transverse plane of a particle (where $P_T = Pcos\theta$), E_T is the analogous quantity but measured in the calorimeter and $\not\!\!E_T$ is the missing energy in the transverse plane. It is important to note that all these quantities are vectors in the transverse plane.

4.2 Central Electron Identification

For central electron identification we use a series of cuts as described in Table 4.1. Central electrons are in the $-1 < \eta < 1$ region. We use relatively strict cuts to have very clean electron objects, and require they be of relatively high energy. There are a number of variables we use to identify electrons, the meaning of which are described below;

- **$\mathbf{E_T}$:** This is the transverse energy, using the total energy (E_{EM}) measured in the electromagnetic calorimeter: $E_T = E_{EM} sin\theta$. An electron would leave a signal in this detector component. We require relatively high energy electrons for our measurement.

- **$\mathbf{E_{HAD}/E_{EM}}$:** This is the ratio of the energy deposited in the hadronic calorimeter to that deposited in the electromagnetic calorimeter. Electrons leave most of their energy in the electromagnetic calorimeter, so we require the ratio to be very low.

- **$\mathbf{L_{shr}}$:** This is a variable obtained from the comparison of the lateral shower profile and the expected electromagnetic shower. It is defined as;

$$L_{shr} = 0.14 \sum \frac{E_i^{measured} - E_i^{expected}}{\sqrt{(0.14\sqrt{E})^2 + \sigma^2_{E_i^{expected}}}} \tag{4.1}$$

  where the index i runs over the calorimeter towers, $E_i^{measured}$ is the energy measured in tower i and $E_i^{expected}$ is the energy expected from test beam data. Typically L_{shr} is a two-tower sum. Any extra particles accompanying the one responsible for the main EM shower will tend to add to the energy of the adjacent towers and make L_{shr} a larger number.

- **Track $\mathbf{P_T}$:** This is the projection of the associated COT track momentum in the transverse plane.

- **E/P:** This is the ratio of the electromagnetic calorimeter energy to the momentum of the track as measured in the COT. Requiring a fraction lower than 2 helps reduce the number of hadronic jets that look like electrons.

- **$\mathbf{q \cdot \Delta x}$:** The distance between the COT track extrapolated to the CES and the best matching CES cluster is represented by Δx. By requiring a small difference we require a match between the two. The Δx is multiplied by the charge of the track Q and is asymmetric in $r - \phi$ to account for possible photon bremsstrahlung in the direction of the outside of the track.

- **$|\Delta \mathbf{z}|$:** This is the same type of variable as the Δx above, but in the z direction.

- **χ^2:** This variables compares the shower profile in the shower maximum detector, CES, with the shower profile obtained from test beam electrons. By requiring a number below 10 we demand a reasonable agreement.

- **Track quality:** To require a quality track for reconstruction in the COT, hits in a minimum number of superlayers is required and a minimum number of hits per superlayer.

- **Fiduciality:** This variable is simply a geometrical indicator. Where all of the central detector coverage is denoted by a value 1. When a particle goes into a detector gap or outside of the central detector range, the value of this variable differs from 1.

- **Isolation:** This variable serves to quantify how much activity is found around an object track. It is defined by the ratio of transverse energy in the electromagnetic and hadronic calorimeter in a cone of radius $\Delta R = \sqrt{(\Delta\eta)^2 + (\Delta\phi)^2} \leq 0.4$ excluding the electron cluster energy itself to the electron EM energy. For example if an electron is embedded in a jet from a b-quark decay, this variable will tend to be large

Careful studies were performed in CDF to optimize the cuts of the variables just described. In Table 4.1 [55] we give the values of the cuts applied for electron

selection. Additionally we require the electrons to have Isolation<0.1, both calculated from calorimeter and track quantities.

EM E_T	$>$ 20 GeV
E_{HAD}/E_{EM}	$<$ 0.055 + 0.00045·E
L_{shr}	$<$ 0.2
Track P_T	>10 GeV/c (if EM $E_T \leq$100 GeV) >50 GeV/c (if EM E_T >100 GeV)
E/p	$<$ 2 (if EM $E_T \leq$100 GeV)
$q \cdot \Delta x$	[-3.0, 1.5] cm
$\lvert\Delta z\rvert$	$<$ 3 cm
χ^2	$<$ 10
track $\lvert z_0\rvert$	$<$ 60 cm
Track quality	3 axial and 2 stereo SL with at least 5 hits out of 12 in each SL
Fiducial	*fidele*=1 (Ces $\lvert X\rvert$ <21 cm, 9< Ces $\lvert Z\rvert$ <230 cm Tower 9 excluded, most towers next to chimney included)

Table 4.1: Baseline cuts for central high-P_T isolated electrons (E_T > 20 GeV) (CEM).

4.3 Forward Electron Identification

Forward electrons are in a region of $\mid \eta \mid > 1.2$. For these electrons the COT cannot provide tracking information, so the SVX and ISL are used for tracking. Because the algorithm used in tracking is called the Phoenix Algorithm, these electrons are also called Phoenix Electrons. The algorithm starts by associating a track with energy observed in the PEM cluster. The track is constrained at the primary vertex and at the center of the cluster. Two tracks are constructed based on the two possible charges of the electron. The algorithm next looks for hits in the silicon that matches the tracks. If hits are matched the track is reconstructed. If both tracks are reconstructed the one with the best goodness of fit is taken. We use electrons up to $\mid \eta \mid < 2$, beyond which our ability to precisely identify electrons degrade. If the plug electron passes all requirements described in Table 4.2, it is classified as Phoenix, denoted *PHX*.

The variables that are used are similar to the ones described for central electrons. Variables not previously defined are described below;

- **PhxMatch:** This variable is true if there is a match between the Phoenix track and a PES shower.

- **PEM 3×3 Fit tower:** This variables describes whether there is a successful fit of shower position from the 3×3 PEM towers.

- **PEM 3×3 Fit χ^2:** This variable compares the position of the shower obtained from the 3×3 PEM towers around the seed tower to what was obtained from test beam electrons by means of a χ^2 test statistics.

- **PES 5×9 U and V:** The variables $U_{5x9} \geq 0.65$ and $V_{5x9} \geq 0.65$ are isolation variables for the shower maximum detector. The U and V layers are at a 45 degree angle to each other, as explained in chapter 3. The clustering in each layer is performed by ordering strips in decreasing energy with the highest energy strips used as seeds. These variables represent the ratios of the energy sum in the central 5 strips to the total energy in all of the nine strips.

- **Track $|\mathbf{z_0^{PHX}}|$:** This is the vertex of the Phoenix track coordinate in the z axis.

- **ΔR(Track,PES):** This variable compares the position of the shower obtained from the χ^2_{3x3} fit to the intersection of the centroids in the layers U and V of the PES. The difference in $\Delta\eta$ and $\Delta\phi$, determines $\Delta R^2(\text{Track}, \text{PES}) = (\Delta\eta)^2 + (\Delta\phi)^2$.

- **Track $\mathbf{Z_0}$:** This is the impact parameter along the z axis.

The Table 4.2 [55] shows the value of the cuts that were agreed upon after careful optimization at CDF for forward electrons. These electrons are also required to have both calorimeter and track based Isolation<0.1.

EM E_T	$>$ 20 GeV
PhxMatch	true
E_{HAD}/E_{EM}	$< 0.05 + 0.026 \cdot \ln(\frac{E_{EM}}{100})$ (if E_{EM} >100 GeV) $<$ 0.05 (if $E_{EM} \leq$100 GeV)
PEM 3×3 Fit tower	$\neq$0
PEM 3×3 Fit χ^2	<10
PES 5×9 U and V	>0.65
PES based Fiducial	1.2< $\|\eta\|$ <2.0
Silicon track	2D Phoenix track
Number of Silicon Hits	$\geq$3
Track $\|z_0^{PHX}\|$	$<$ 60 cm
ΔR(Track, PES)	<3

Table 4.2: Baseline cuts for plug isolated electrons (PHX).

4.4 Muon Identification

A muon is a minimum ionizing particle that leaves a track in the COT, which leaves very little energy deposited in the electromagnetic and hadronic calorimeters. We distinguish among different categories of muons depending upon which of the muon drift chambers register hits associated with the muon COT track. We can have then a CMU, CMP or CMX muon depending on hits in the drift chambers of their name, as well as CMUP muons (hits in the overlap region of CMU and CMP) and CMIO muons which are tracks that pass all of the minimum ionizing criteria but do not point to a muon drift chamber.

For minimum ionizing particles we require the cuts in Table 4.3. All these tracks must be *calorimeter isolated* and *track isolated* following the same definitions as for electrons. The geometrical coverage of our muon objects (exept for CMIO's) are $|\eta| < 1.0$. The variables used for these cuts that were not defined before are below:

- **$|\mathbf{d_0}|$:** The impact parameter d_0 is the distance of z_0 to the the closest point in the track. This selection is used for the default muon track. A cut on this variable forces the muon to originate from the nominal interaction point, and substantially reduces cosmic muons that entered the detector in the time window of the collision.

- **$|\Delta\mathbf{x_{CMU,CMP,CMX}}|$:** This is the distance in the $r-\phi$ plane between the COT track extrapolated to the muon hit segment, and the position of the reconstructed muon hit for the muons in different sub-detectors.

- **x-fid(CMP,CMX) and z-fid(CMP,CMX):** This is the maximum difference between the x and z extrapolation of the COT track and the muon detector fiducial region.

The minimum ionizing particle cuts are in Table 4.3 s[56]. In future sections we will describe corrections made to some of these variables.

A minimum ionizing high-P_T isolated track will be classified as:

- A *CMUP* muon, if there are hits in both the CMU and CMP detectors, with $|\Delta X|_{\rm CMU}$ <3 cm and $|\Delta X|_{\rm CMP} < 5$ cm respectively.

- A *CMX* muon, if there is one hit in the CMX detector, with $|\Delta X|_{\rm CMX} < 6$ cm.

- A *non-triggering muon*: A non-triggering muon can enter our analysis as the second leg of a dilepton event (we will describe dilepton events in more detail later), and can appear in the following ways:

    1. *CMU-only* with a hit in the CMU (CMP) detector and non fiducial in the CMP detector.

    2. *CMP-only* with a hit in the CMP detector and non fiducial in the CMU detector.

Track P_T	>20 GeV/c
Track $\|z_0\|$	< 60 cm
E_{EM}	< 2+Max(0,0.0115(P-100)) GeV
E_{HAD}	< 6+Max(0,0.028(P-100)) GeV
Track $\|d_0\|$	0.2 cm (if no silicon hits attached by OI) 0.02 cm (if silicon hits attached by OI)
$\|\Delta x_{CMU}\|$	< 3.0 cm (CMUP or CMU)
$\|\Delta x_{CMP}\|$	< 5.0 cm (CMUP or CMP)
$\|\Delta x_{CMX}\|$	< 6.0 cm (CMX)
Track quality	3 axial and 2 stereo SL with at least 5 out of 12 in each SL
Track $\|z_0\|$	< 60.0 cm
Fiducial Cuts ([56])	
For CMUP: For CMU-only: For CMP-only: For CMX	x-fid(CMP) < 0 cm, z-fid(CMP) < -3 cm - x-fid(CMP) < 0 cm, z-fid(CMP) < -3 cm x-fid(CMX) < 0 cm, z-fid(CMX) < -3 cm

Table 4.3: Baseline cuts for minimum ionizing isolated track. After passing these cuts the muon is classified as *CMUP*, *CMX* or *non-triggering* according to the definitions in the text.

3. If there are no muon detector hits, the minimum ionizing high P_t isolated track will be classified as a *CMIO*. Further details of the selection cuts are discussed below.

The CMIO muon category is designed to recover some acceptance lost from the muons which are non-fiducial in the central CDF detector region ($|\eta| < 1.1$), to any muon chamber (CMU, CMP or CMX). We additionally require that the extrapolated track be fiducial to the central calorimeter, to exclude the non-instrumented regions in the calorimeter (tower 7, 8 and 9). In this way we decrease the chance that an electron that goes through a crack in the EM calorimeter will look like a CMIO muon.

4.5 What About τ Identification?

Even though τ particles can be identified in CDF, for the purpose of having a simple and clean analysis we infer the existence of τ leptons in our events by their e or μ

decays and do not directly identify them.

4.6 Hadronic Jets

In $p\bar{p}$ collisions, quarks and gluons can result from various processes, both as initial and final state radiation, as well as a direct result from inelastic collisions. These quarks and jets are subject to the hadronization process. The hadronization process is the creation of hadrons out of quarks and gluons, as described in section 1.2.4. Quarks and gluons cannot exist individually, rather they combine with other quarks and gluons spontaneously created from quantum fluctuations in vacuum.

Hadronization and fragmentation models serve to describe the way quarks and gluons typically behave in the detector, with single quarks and gluons resulting in a jet of a multitude of particle pairs that leave tracks in the COT and SVX, and deposit energy mostly in the hadronic calorimeters.

The jets objects are reconstructed from the energy deposited in the calorimeter towers with an algorithm called jet clustering. The algorithm starts by identifying the seed tower as the one with the largest calorimeter energy. The cluster of towers within the cone $\Delta R = \sqrt{(\Delta\eta)^2 + (\Delta\phi)^2} = 0.4$ from the center of the seed tower are identified. The cone size $\Delta R = 0.4$ is chosen to include most of the jet energy without including a large contribution from other event activity. After the cluster is formed, the shower center in the (η, ϕ) space of the calorimeter is given by:

$$\eta_{centroid} = \frac{\sum_i E_T^i \eta^i}{\sum_i E_T^i} \tag{4.2}$$

$$\phi_{centroid} = \frac{\sum_i E_T^i \phi^i}{\sum_i E_T^i} \tag{4.3}$$

where the sum is over the towers in the cluster and $\eta^i(\phi^i)$ represents the $\eta(\phi)$ coordi-

nate of the center of the tower. After the position of the shower is calculated, a new cone is defined centered in the new coordinates and the calculation is repeated for the new cluster. This process is then iterated until the cluster remains unchanged. The transverse energy of the jet is given by:

$$E_T^{raw} = \sqrt{(\sum_i E_i sin(\theta_i) cos(\phi_i))^2 + (\sum_i E_i sin(\theta_i) sin(\phi_i))^2} \tag{4.4}$$

were E_i is the total energy in tower i. This quantity represents the energy deposited in the cluster, and does not include any corrections. We require the transverse energy of jets to be at least 15 GeV. We consider jets in the region $\mid \eta \mid < 2.5$.

4.7 Neutrinos (Missing Transverse Energy)

Neutrinos leave no direct trace in our detector. However their presence can be inferred by requiring a balance of transverse energy in the event. Given the fact that we don't know the total longitudinal energy due to the Parton Distribution Functions, as discussed in section 2.1, we restrict ourselves to the transverse plane. We call the transverse energy required to make the vector sum in the transverse plane zero,the Missing Transverse Energy ($\not\!\!E_T$). Other sources can contribute to the $\not\!\!E_T$ measurement, including mismeasured energies and particles tracks that go through uninstrumented regions of the detector. However, for the types of events we study, the largest contribution typically comes from neutrinos, especially in the WW and $t\bar{t}$ decay processes.

For calculating the $\not\!\!E_T$, the transverse energy (E_T) is summed from all calorimeter towers and projected in the transverse plane to the beam direction. The expression

for the E_T is given below:

$$\vec{E}_T^{raw} = \sum_{cal\ towers} E_i^{raw} sin(\theta_i)\vec{n}_i \tag{4.5}$$

where the sum is over all calorimeter towers, E_i^{raw} is the raw uncorrected energy of each tower, θ_i is the polar angle to the center of the tower, and $\vec{n}_i$ is a transverse unit vector pointing to the center of the tower.

The E_T has to be further corrected event by event to account for identified muons in the event since the muons leave very little of their energy in the calorimeter. In the next section we will see that jet energies also need to be corrected, and thus these corrections will also affect the total E_T.

Since the energy in the transverse plane is assumed to be balance, the missing transverse energy is then simply given by $\not\!\!E_T = -\vec{E}_T$.

4.8 Variable Corrections

A multitude of corrections are applied to both the data and the Monte Carlo to account for either deficiencies in the simulation or in the data reconstruction of measured variables. Of these, the most important are corrections made to the energy of the reconstructed jets, which then affect the estimation of the missing transverse energy. These variables are very important to our analysis. In this section we will describe the main corrections applied to the data. When we discuss our Monte Carlo samples in chapter 6, we will list a number of scale factors applied to the Monte Carlo samples.

4.8.1 Jet Corrections

In CDF there are 7 levels of jet corrections that can be applied to the jet energies. Depending on the use of the jet objects by the different analyses, different levels

of corrections are applied. In our project we use the first five levels of corrections. However when estimating the systematic error associated with the jet energies, we consider systematic sources associated with all seven levels of corrections.

Below we have the different levels of corrections that are applied to the jet energies;

- **Relative correction:** There are relative tower to tower differences in the response of the calorimeter, these must be corrected to achieve a uniform response across the calorimeter system,

- **Time dependent correction:** The calorimeter system has shown signs of aging and the response has been shown to decline with time. A correction that is dependent on the time the data was took is applied to normalize all the data taken to the same response.

- **Energy scale correction:** This correction takes into consideration some differences between Run I and Run II, and also some differences between data and Monte Carlo in photon+jets events.

- **Multiple interaction correction:** The energy from different $p\bar{p}$ interactions during the same bunch crossing falls inside the jet cluster, increasing the energy of the measured jet. This correction subtracts this contribution from the average.

- **Absolute energy correction:** Corrects the jet energy measured in the calorimeter for any non-linearity and energy loss in the uninstrumented regions of the calorimeter. The jet energy measured is corrected to the sum of the P_T of the particles within the cone of the same size around the parton direction which matched the jet direction with $\Delta R < 0.4$

- **Underlying event correction:** The underlying event is defined as the energy associated with non-participating partons in a hard collision event. Some analyses need this energy to be subtracted from the jet energy.

- **Out of cone correction:** This is a correction that deals with leakage of radiation outside the clustering cone used for the jet definition (in our case a cone of 0.4 solid angle).

4.8.2 Missing Transverse Energy ($\not\!\!E_T$) Correction

Given that the jet energies are a component of the $\not\!\!E_T$ calculation, the jet corrections also affect the $\not\!\!E_T$ and corrections are made accordingly. Additionally the energies of identified muons, that leave small calorimeter traces are added to the $\not\!\!E_T$ using the track measured energies. The position of the primary vertex of the event is also taken into account.

4.9 The Cosmic Event Filter

Cosmic rays are often identified as di-muon events with an angular separation close to 180 degrees in ϕ. Cosmic rays enter the detector at random times and locations. When a cosmic ray goes through the detector close to the interaction point, it is typically reconstructed as two back-to-back COT tracks. The time difference between the energy deposited in both ends of the hadronic calorimeter can be analyzed to identify cosmic rays. Additionally, a cut on the impact parameter of the track efficiently identifies cosmic rays. We use a cosmic ray filter that is based on these principles to reject such events.

4.10 The Conversion Electron Filter

Conversion electrons are electrons produced from the interactions of photons with the detector material, coming as electron-positron pairs. In order to avoid confusing these electrons with the electrons produced in the physics processes under study, we apply a filter to reject events with conversion electrons.

The conversion removal algorithm first searches for a pair of oppositely charged tracks with a common origin. At the origin these must be parallel (in the direction of the parent photon). The cuts applied are $|\Delta XY| \leq 0.2\ cm$ between the two tracks at the origin and $|\Delta cot\theta| \leq 0.04$ between the two tracks with θ the angle between the tracks at the origin.

Chapter 5

Analysis Strategy

In this chapter we describe the basic strategy we follow for carrying out our analysis, including the event selection, basic requirements of the datasets and the kinematic phase space we use to perform the Standard Model fit to the data.

5.1 Motivation and Analysis Introduction

As was discussed in the first chapter, this analysis was developed as a global way of understanding the content of the high-P_T dilepton final state events. After the requirement of 2 high-P_T leptons only ($P_T > 20$ GeV), we consider the processes that can make up this sample and ask the question what other objects can exist in these events. The answer is neutrinos (which give $\not\!\!E_T$) and jets (either from decays of final state objects, or from initial and/or final state QCD radiation). Therefore, a natural way to analyze the events is to consider the $\not\!\!E_T$ vs. N_{jet} (number of jets) 2-D distribution from the data and compare it to the expected Standard Model contributions.

By comparing the Standard Model to the data in the $\not\!\!E_T$ vs. N_{jets} phase space we can extract the cross sections of the main contributing processes, which include $t\bar{t}$, WW and $Z \to \tau\tau$. As will be shown, this works because of a very nice (fortuitous?) feature of this sample: the main contributions appear in very different regions of the $\not\!\!E_T$ vs. N_{jet} phase space because of their different sources of $\not\!\!E_T$ and jets.

Additionally, this new method we developed was intended as a first step towards having a global comparison of the Standard Model to the data in an experimental channel that has the potential of revealing new physics processes. It is the intentended

to further develop this method into a search for new physics. In this thesis we concentrate on its potential for giving precise measurements of Standard Model cross sections, which is the first step towards this endeavor. We consider only final states with two high P_T leptons, in the ee, $e\mu$ and $\mu\mu$ channels.

In the standard Run II dilepton $t\bar{t}$ and WW analyses, a series of cuts is placed on $\not\!\!E_T$, jet and lepton related variables, and the cross sections determined from the resulting event count N, total background estimation B, acceptance for the signal process ϵ, and the integrated luminosity $\mathcal{L}$ [57, 58, 59, 60], thus;

$$\sigma = \frac{N - B}{\epsilon \mathcal{L}} \tag{5.1}$$

This was also the philosophy for the corresponding Run I measurements [1, 61].

In the $e\mu$ channel, the main processes that contribute are WW, $Z \to \tau\tau$ and $t\bar{t}$, and it is for these processes we extract cross sections. Additionally we have a so called fake contribution (we will describe this source of background in detail in section 6.4) and to a lesser degree the standard model WZ, ZZ and $W\gamma$ contributions. Other Standard Model sources of background processes are very small in comparison. In chapter two we describe briefly the phenomenology of the main processes we consider.

In the ee and $\mu\mu$ channels we additionally have a large $Z/\gamma* \to ee$ and $Z/\gamma* \to \mu\mu$ Drell-Yan contribution. We found the need to reduce significantly this contribution in the ee and $\mu\mu$ channels, otherwise it would dominate over our other processes. By making a $\not\!\!E_T$ significance cut, which we define in section 5.2.2 we greatly reduce the Drell-Yan background in the ee and $\mu\mu$ channels, while maintaining most of our signal processes.

As mentioned, besides electrons and muons in all of these sources, the only other objects are jets and neutrinos. We maximally exploit this fact by not cutting on variables related to these objects, but rather fitting the data to the 2-D $\not\!\!E_T$-N_{jet}

phase space. The strength of this approach lies in the very different regions of the $\not\!\!E_T$-N_{jet} space occupied by the relatively few Standard Model processes contributing to the high-P_T dilepton sample. This is further illustrated in section 6.6. Specifically, for the $e\mu$ final state channel:

1. $t\bar{t}$:

   The jets in the event primarily come from b quarks from the top decay. There can also be a contribution from ISR and FSR. This gives a jet multiplicity peak around 2 jets. The $\not\!\!E_T$ in the event comes from leptonic W decay. The $\not\!\!E_T$ is not very correlated to the jet multiplicity.

2. WW:

   The jets in the event come from ISR and FSR only. This implies a steeply falling jet multiplicity spectrum. The $\not\!\!E_T$ comes from W decays and is typically much larger than for $Z \to \tau\tau$. Also the $\not\!\!E_T$ is somewhat correlated to the jet multiplicity.

3. $Z \to \tau\tau$:

   The jets in the event come from ISR and FSR only. This implies a steeply falling jet multiplicity spectrum. The $\not\!\!E_T$ comes from the τ decays, and is strongly correlated to the jet multiplicity: the $\not\!\!E_T$ tends to be close to zero with no jets in the events, but when the Z recoils off ISR the neutrino directions are more aligned and the $\not\!\!E_T$ increases significantly.

4. Background contributions:

   All the background contributions including WZ, ZZ, Drell-Yan, $W\gamma$ and the fake lepton background are expected to have a low number of jets, mostly driven by ISR and FSR contributions.

This is summarized in Figure 5.1, which shows schematically the regions of our phase space that these processes occupy.

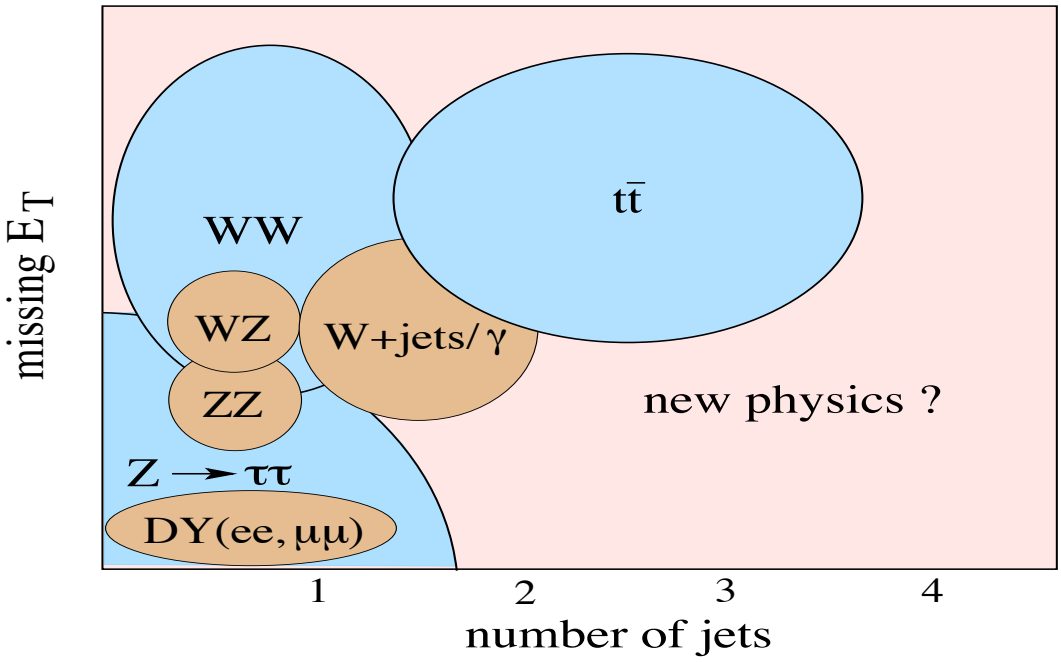

Figure 5.1: Schematic of the Standard Model contributions in the $\not\!\!E_T$ vs. number of jets phase space.

We obtain both the expected Monte Carlo distributions and the data distributions in this phase space. We then fit the data to the Standard Model as described in section 6.7 using a maximum likelihood technique.

From this likelihood fit of the data to the expected Standard Model processes we simultaneously measure the $t\bar{t}$, WW, and $Z \rightarrow \tau\tau$ cross sections, which are allowed to float in the fit, with all the other contributions fixed within their estimated uncertainties. The details of this procedure, and variations thereof, are given in section 6.7.

5.2 Event Selection

The sample we use consists of dilepton events containing isolated electrons and muons using the standard lepton cuts described in Chapter 4. We also apply the cosmic-ray and conversion filter that were introduced in the last chapter, and consider only opposite sign leptons. To reduce the Drell-Yan background in the ee and $\mu\mu$ channels we require an additional cut on $\not\!\!E_T$ significance defined by:

$$\not\!\!E_T^{sig} = \frac{\not\!\!E_T}{\sqrt{\sum E_T}}$$

where $\sum E_T$ is over all (raw) calorimeter towers. This variable is extremely effective at removing ee and $\mu\mu$ Drell-Yan events while preserving our signal processes in the ee and $\mu\mu$ channels. A more detailed description of the $\not\!\!E_T^{sig}$ is given in section 5.2.2. In Table 5.1 we summarize our event selection procedure.

Event Selection Cuts
2 high P_T isolated leptons
Apply cosmic filter
Apply conversion filter
In ee and $\mu\mu$ final states only, apply $\not\!\!E_T^{sig}$ cut
Require that the final 2 leptons be opposite sign

Table 5.1: Event selection cuts

5.2.1 Dilepton Categories

We classify our events according to where in the detector the two leptons are found. We build dilepton categories with the two high-P_T isolated leptons according to the categorizations in Table 5.2. Here at least one of the leptons has passed the electron or muon trigger. Our data samples are reconstructed using triggerable electrons only in the central calorimeter (TCE), and, CMUP and CMX triggerable muons. The

other muon types only enter our analysis when associated with a triggerable lepton. The same holds true for forward phoenix electrons (PHX).

ee		$\mu\mu$		$e\mu$	
1st leg	2nd leg	1st leg	2nd leg	1st leg	2nd leg
TCE	**TCE**	**CMUP**	**CMUP**	**TCE**	**CMUP**
	PHX		**CMX**		**CMX**
			CMU		CMU
			CMP		CMP
			CMIO		CMIO
		CMX	**CMX**	**CMUP**	PHX
			CMU	**CMX**	PHX
			CMP		
			CMIO		

Table 5.2: Dilepton categories included in the current analysis. Shown in bold are the triggerable leptons in the data samples studied. Both lepton legs are required to be isolated.

5.2.2 The Missing Energy Significance

As already mentioned, the $\not\!\!E_T^{sig}$ cut is used to reduce the Drell-Yan background in the ee and $\mu\mu$ final state events. Without such a cut the Drell-Yan background would completely dominate over the other processes and a measurement of other standard model processes would be impossible in the ee and $\mu\mu$ channels (recall that this is not an issue in the $e\mu$ channel). One consequence of this cut is that it is also quite effective in cutting the $Z \to \tau\tau$ contribution. As a result we can measure the $Z \to \tau\tau$ cross section only in the $e\mu$ channel, so that ee and $\mu\mu$ events contribute only to the $t\bar{t}$ and WW cross section measurements.

We used a variable as missing energy significance defined below;

$$\begin{aligned} \sum E_T &= \sum E_T(raw) \\ &+ \sum (P_T(muons) - (E_T(em) + E_T(had))(muons)) \end{aligned} \tag{5.2}$$

$$+ \quad \sum(E_T(jets)(-1 + f_{corr}(L5)))$$

We found also that the optimal value for the cut on this variable to separate our signal processes from the Drell-Yan is 2.5.

5.2.3 Event Triggers

In chapter 3 we cited the CDF data samples we use; the electron bhel0d and muon bhmu0d samples. In the electron samples, at least one electron has passed the $ELECTRON\_CENTRAL\_18$ trigger requirements, shown in Table 5.3. In the muon samples at least one muon has passed the $MUON\_CMUP18$ or $MUON\_CMX18$ trigger requirements, shown in Table 5.4. These samples were processed with version 5.3.1 of the CDF Production software. In CDF progressive improvements are made on the production software for reconstruction of physics objects and this version represents the most up to date version corresponding to the dates the data we used was collected. The data sample we use in this analysis corresponds to an integrated luminosity of about 360 pb^{-1}, but it depends on the dilepton category. We will give a more detailed description of the luminosity of our data sample as a function of the dilepton categories in section 6.6.1.

Level 1
At least one calorimeter tower must have $E_T > 8$ GeV $E_{had}/E_{em} < 0.125$ At least one COT track with $P_T > 8$ GeV pointing at tower
Level 2
Calorimeter cluster must have $E_T > 16$ GeV $E_{had}/E_{em} < 0.125¡0.125$ XFT track with $P_T > 8$ GeV matched to seed tower of cluster
Level 3
EM cluster reconstructed by offline algorithm must have $E_T > 18$ GeV $E_{had}/E_{em} < 0.125¡0.125$ Reconstructed 3D COT track with $P_T > 9$ GeV pointing at the cluster

Table 5.3: $ELECTRON\_CENTRAL\_18$ trigger requirements

Level 1
Hits in CMUP/CMX Matching COT track with $P_T > 8$ GEV (CMUP or CMX)
Level 2
No additional requirements
Level 3
Reconstructed 3D COT track with $P_T > 18$ GeV matched with CMUP or CMX hits

Table 5.4: $MUON\_CMUP18$ and $MUON\_CMX18$ trigger requirements

Chapter 6

Global Method for Measuring Standard Model Cross Section

In this chapter we describe the details of the analysis methodology. We start with the description of the simulation of the Standard Model physics processes by Monte Carlo samples. Then we study the way our signal and background processes behave under the selection criteria. We go into some detail about how to estimate our background expectations including our fake lepton background. We estimate systematic uncertanties in our calculated Standard Model expectations. We present our data events, describe the likelihood fit used to extract cross section measurements, and show our studies to validate the fit method and the systematic errors input into the fit. In the next chapter we will give the cross section results that follow from this analysis.

6.1 Monte Carlo Simulated Datasets

Our Monte Carlo simulated samples, were generated mostly with the Pythia or Herwig generators and interfaced with the CDF detector simulation and the production CDF software. We used the version 5.3.2 of the CDF simulation and production software, which was the most up to date version at the time.

In CDF the generated and processed samples get a unique identification code. In Table 6.1, we cite the samples used for estimating signal and backgrounds expectations, the Monte Carlo generator used, the dataset id and the theoretical cross section of the process. We use the signal Monte Carlo samples to estimate the signal acceptance, which is the probability a generated event survives the selection criteria.

In the case of the Background processes, we use the Monte Carlo sample to extract the expected number of events from that process normalized to our data integrated luminosity.

Process	Generator	Dataset ID	$\sigma(pb)$	Number of Events generated
Signal				
$t\bar{t}$	PYTHIA	ttopel($m_{top} = 178$ GeV)	6.7	1142339
WW	PYTHIA	wtop1w	12.5	419728
WW	PYTHIA	wewk5d	12.5	3295522
$Z/\gamma \rightarrow \tau\tau$	PYTHIA	ztop4i & ztop5i	$\times$ 1.4	2525739 (0.1367% filt.)
Backgrounds				
$Z/\gamma \rightarrow$ ee	PYTHIA	zewk6d	355.2 $\times$ 1.4	3108482
$Z/\gamma \rightarrow \mu\mu$	PYTHIA	zewk6m	355.2 $\times$ 1.4	3216951
$Z/\gamma \rightarrow \ell\ell$	PYTHIA	sexo8t	17354.0 $\times$ 1.4	3164279
WZ	PYTHIA	wtop1z	3.65	407438
ZZ	PYTHIA	ztopcz	1.39	397086
W $\gamma \rightarrow e^{+}\nu\ \gamma$	PYTHIA	ktop2e	22.35	68273
W $\gamma \rightarrow e^{+}\nu\ \gamma$	PYTHIA	ktop3e	22.35	102473
W $\gamma \rightarrow \mu^{+}\nu\gamma$	PYTHIA	ktop2m	22.35	93073
W $\gamma \rightarrow \mu^{+}\nu\ \gamma$	PYTHIA	ktop3m	22.35	103608
Samples used for cross-checks				
$Z/\gamma \rightarrow \tau\tau$	PYTHIA	zewk8t	355.2 $\times$ 1.4	3338836

Table 6.1: Monte Carlo datasets used for AIDA analysis.

6.2 Signal Acceptances

In order to measure the $p\bar{p} \rightarrow t\bar{t}$, $p\bar{p} \rightarrow WW$ and $p\bar{p} \rightarrow Z \rightarrow \tau\tau$ cross sections we must first understand how events from these samples look in our fit phase space, as well as estimate the probability that an event from those processes passes our selection cuts (its acceptance). As we mentioned already, we use Monte Carlo samples from

table 6.1 for this. For the background processes we estimate the expected number of events.

For each event we have to first take into account scale factors that correct for various differences between data and Monte Carlo. We also have to account for trigger efficiencies, lepton identification efficiencies, reconstruction efficiencies, etc. in such a way that we get the same response in Monte Carlo as we would expect in the data.

6.2.1 Scale Factors

We correct for trigger inefficiencies with the factors in Table 6.2. We also correct for the difference in lepton identification efficiencies between data and MC by applying the scale factors shown in Table 6.3. Furthermore we correct PHX electrons, whose charge has a probability of being mis-identified because of the high η of the associated silicon track, with the factors from Table 6.4 [62]. These factors were obtained from carefull study in collaborative work by CDF members, using data-Monte Carlo comparisons.

Lepton Type	Trigger Efficiency
TCE	0.962 ± 0.0066 [63]
PHX	0.955 ± 0.019 [63]
CMUP	0.908 ± 0.005 [56]
CMX	0.965 ± 0.004 [56]

Table 6.2: Summary of trigger efficiencies. The CEM_18 trigger efficiency is run-dependent, number given above being an average over η.

6.2.2 Signal Acceptance Table

In the Table 6.5 we summarize the signal acceptances, and expected number of events. Even though the $Z \rightarrow \tau\tau$ is listed as a signal process, in the ee and $\mu\mu$

Lepton Type	ID×Reconstruction Scale Factor $p_T > 20$ GeV
TCE	0.996 ± 0.005 [62]
PHX	0.948 ± 0.016 [62]
CMUP	0.892 ± 0.009 [56]
CMX	0.999 ± 0.006 [56]
CMU	0.889 ± 0.010 [56]
CMP	0.907 ± 0.009 [56]
CMIO	0.995 ± 0.003 [56]

Table 6.3: Summary of lepton data/MC scale factors.

$\lvert\eta_{\text{PHX PES}}\rvert$ Range	Data/MC Scale Factor
$1.2 < \lvert\eta\rvert < 1.4$	$(1 - 0.061)/(1 - 0.061)$
$1.4 < \lvert\eta\rvert < 1.6$	$(1 - 0.099)/(1 - 0.097)$
$1.6 < \lvert\eta\rvert < 1.8$	$(1 - 0.150)/(1 - 0.143)$
$1.8 < \lvert\eta\rvert < 2.0$	$(1 - 0.168)/(1 - 0.138)$

Table 6.4: PHX charge mis-identification scale factors.

final states this is taken to be a background process. In the table the acceptances are expressed in percentages, the errors shown are statistical in nature. In appendix D we further give tables with the number of events surviving each analysis cut per category for all signal and background processes, this in order to understand the relative contributions from each of the dilepton categories.

	$e\mu$	ee	$\mu\mu$	ll
$t\bar{t}$	$(0.40 \pm 0.006)\%$	$(0.14 \pm 0.003)\%$	$(0.14 \pm 0.003)\%$	$(0.68 \pm 0.013)\%$
	10.0 ± 0.7	3.6 ± 0.5	3.4 ± 0.4	17.0 ± 1.6
WW	$(0.30 \pm 0.001)\%$	$(0.11 \pm 0.0006)\%$	$(0.09 \pm 0.0005)\%$	$(0.50 \pm 0.002)\%$
	13.8 ± 0.8	5.2 ± 0.4	4.3 ± 0.3	23.5 ± 1.5
$Z \to \tau\tau$	$(0.046 \pm 0.0005)\%$	$(0.0008 \pm 0.00007)\%$	$(0.0005 \pm 0.00005)\%$	$(0.047 \pm 0.0006)\%$
	57.8 ± 4	1.1 ± 0.2	0.6 ± 0.1	59.9 ± 4.3

Table 6.5: Signal acceptances (%) and expected number of events.

6.3 Background Expectations

From our Monte Carlo samples, and considering the data integrated luminosity per category, as given in Table 6.29, we can estimate the expected number of events in our sample from the main backgrounds. In Table 6.6 we have such expectations, we exclude the fake lepton background which we describe in the next section. The description of the errors that enter the table is summarized in section 6.5.2.

	$e\mu$	ee	$\mu\mu$	$\ell\ell$
$DY \to ee$	0	15.38 ± 3.2	0	15.4 ± 3.2
$DY \to \mu\mu$	9.3 ± 0.8	0	11.6 ± 2.4	20.8 ± 3.2
WZ	0.70 ± 0.06	1.26 ± 0.09	1.11 ± 0.08	3.07 ± 2.3
ZZ	0.07 ± 0.01	0.47 ± 0.03	0.42 ± 0.03	0.96 ± 0.07
$W\gamma$	1.2 ± 0.5	1.8 ± 0.7	0	3.0 ± 1.2

Table 6.6: Standard Model background expected number of events in $\sim 360\,\mathrm{pb}^{-1}$

6.4 The Fake Lepton Background

We describe in this section the estimation of the contribution to our backgrounds from jets being mis-identified as one or more leptons and resulting in a dilepton event. This background is relatively minor when compared with the signal expectations, but given its unusual nature, we devote quite a bit of detail to its description.

We divide the estimation of this background in two parts. First we extract from the jet data the probability of a jet faking a lepton, then we apply this probability to the W+jets data in order to find its expected contribution.

6.4.1 The Fake Rate Estimation Methodology.

We used jet samples as described in Table 6.7 for estimating the fake ratios. We applied a selection on the runs were no relevant part of the detector was having

malfunctions, we call this the good run list. The total integrated luminosity after applying good run list was 360 pb^{-1}

dataset ID	trigger	trigger requirement
gjt10d	Jet 20	at least a raw jet with $E_T > 20\ GeV$
gjt20d	Jet 50	at least a raw jet with $E_T > 50\ GeV$
gjt30d	Jet 70	at least a raw jet with $E_T > 70\ GeV$
gjt40d	Jet 100	at least a raw jet with $E_T > 100\ GeV$

Table 6.7: The jet datasets and trigger requirement used for the lepton fake rate.

We define the *fake rate* as the probability that a *fakeable* object passes the tight lepton identification criteria. The value of the fake rate is dependent on the definition of fakeable objects. Given the fact that sample composition varies according to the jet sample, a good balance must be achieved between generalization of the fakeable object definition, and consistency across the different jet samples.

For *electrons*, fakeable objects are electromagnetic clusters loosely selected from CDF Electromagnetic Objects. Different from generic jets, these objects additionally must pass a series of so called *denominator cuts*. In Tables 6.8 and 6.9 we list the denominator cuts applied to fakeable central (CEM) and PHX electrons respectively. As can be seen in those tables, we differentiate uniquely between two classes of fakeable electrons, depending on the region of the detector they belong to; phoenix or central fakeable electrons.

Collection type = DefEm
region = 0 (Central)
$E_T >=$ 20.0 GeV
Track $P_T > 0$
$E_{had}/E_{em} < 0.125$
Track $Z0 < 60$
It is not a conversion electron
Calorimeter Isolation < 0.2

Table 6.8: The CEM denominator cuts

Collection type = Phoenix
region = 1 (Plug)
$E_T >= 20.0$ GeV
$E_{had}/E_{em} < 0.125$
object is matched to a PHX track
Track $Z_0 < 60$
Calorimeter Isolation < 0.2

Table 6.9: The PHX denominator cuts

For *muons*, the fakeable objects are minimum ionizing particles (MIP's), which are loosely selected from CDF muon objects. Here we make no distinction among different categories of fakeable muons depending on the region of the detector the muons belong to. The list of cuts applied to the muon fakeable objects is given in Table 6.10. Then, we have three possible classifications of fakeable objects, these objects cover all the real or fake lepton sources.

Collection type = DefMuon and has no BMU, or DefStublessMuon
($d_0 < 0.02$ and track Si hits> 0) or ($d_0 < 0.2$ and no track Si hits)
$P_T >= 20.0$ GeV
$E/P < 1$
object is matched to a PHX track
$Z_0 < 60$
Calorimeter Isolation < 0.2

Table 6.10: The muon denominator cuts

The *fake ratio* is mathematically defined as the number of fakeable objects that pass our analysis lepton cuts, separated by lepton category and parametrized as a function of transverse energy, divided by the total number of fakeable objects per transverse energy bin. Below, the fake ratio definitions are given:

$$FR_{TCE/PHX} = \frac{veto\ W/Z,\ veto\ jet^{leading},\ tight\,TCE/PHX\,electrons}{fakeable\,central/plug\,CdfEmObjects} \qquad (6.1)$$

$$FR_{Muons} = \frac{veto\ W/Z,\ veto\ jet^{leading},\ tight\, CMUP/X/U/P/IO\, muons}{fakeable\, MIPs} \qquad (6.2)$$

In the definitions above we remove certain jets to avoid W and Z contamination as well as to remove bias introduced by the triggers of the jet samples.

To reduce jet sample trigger bias, we removed the highest E_T jet (leading jet) and all of the numerator and denominator objects in a cone of $\Delta R < 0.4$ around it per event. This cut is based on the fact that most of the time the highest E_T jet is the one responsible for firing the trigger.

We also remove Z's with a dilepton invariant mass cut of $66 < M_{dil} < 116$ in ee and $\mu\mu$ events. For reducing the W contamination, in events where the dilepton transverse mass lies outside the 40-120 GeV window, a 20 GeV $\not\!\!E_T$ cut is applied when calculating the fake ratios.

The dilepton invariant mass is defined by;

$$Inv.\ mass = \sqrt{(\sum_i E_i)^2 - (\sum_i P_i)^2} \qquad (6.3)$$

where i goes over both leptons. The dilepton transverse mass is defined in the same way as the invariant mass, but using only the components of the constituent momentum transverse to the beam direction.

6.4.2 The Fake Rate Probabilities

The measured fake ratio as a function of jet E_T bins can be seen in Tables 6.11 to 6.17. The weighted average includes all of the jet samples. In the tables we can also see the fake rates per E_T bin per individual jet samples for central electrons, plug electrons and muon categories respectively. The errors are statistical only, and

derived mostly from the jet sample number of events.

We use 4 E_T ranges to bin the data and calculate the fake rates as follows:

- $20 < E_T < 30\ GeV$
- $30 < E_T < 40\ GeV$
- $40 < E_T < 60\ GeV$
- $60 < E_T < 250\ GeV$

Bin	Jet 100	Jet 70	Jet 50	Jet 20	Weig. Av.
20-30 GeV	$0.24 \pm 0.03\%$	$0.13 \pm 0.03\%$	$0.28 \pm 0.04\%$	$0.34 \pm 0.09\%$	$0.21 \pm 0.02\%$
30-40 GeV	$0.24 \pm 0.05\%$	$0.32 \pm 0.07\%$	$0.38 \pm 0.06\%$	$0.5 \pm 0.3\%$	$0.30 \pm 0.03\%$
40-60 GeV	$0.34 \pm 0.05\%$	$0.34 \pm 0.06\%$	$0.67 \pm 0.09\%$	$0.7 \pm 0.5\%$	$0.39 \pm 0.04\%$
60-250 GeV	$1.12 \pm 0.07\%$	$1.51 \pm 0.16\%$	$2.0 \pm 0.3\%$	$2.5 \pm 1.7\%$	$1.21 \pm 0.06\%$

Table 6.11: The CEM individual and weighted fake rates, with Z and W subtraction.

Bin	Jet 100	Jet 70	Jet 50	Jet 20	Weig. Av.
20-30 GeV	$2.6 \pm 0.3\%$	$5.6 \pm 0.5\%$	$2.3 \pm 0.2\%$	$3.0 \pm 0.3\%$	$2.72 \pm 0.13\%$
30-40 GeV	$2.0 \pm 0.3\%$	$4.6 \pm 0.5\%$	$1.97 \pm 0.17\%$	$3.3 \pm 0.7\%$	$2.24 \pm 0.14\%$
40-60 GeV	$2.6 \pm 0.2\%$	$3.5 \pm 0.3\%$	$3.2 \pm 0.2\%$	$5.1 \pm 01.5\%$	$3.09 \pm 0.14\%$
60-250 GeV	$4.52 \pm 0.19\%$	$4.8 \pm 0.4\%$	$6.8 \pm 0.7\%$	$6 \pm 4\%$	$4.73 \pm 0.17\%$

Table 6.12: The PHX individual and weighted fake rates, with Z and W subtraction.

Bin	Jet 100	Jet 70	Jet 50	Jet 20	Weig. Av.
20-30 GeV	$0.496 \pm 0.014\%$	$0.589 \pm 0.016\%$	$0.613 \pm 0.017\%$	$0.177 \pm 0.016\%$	$0.471 \pm 0.007\%$
30-40 GeV	$0.500 \pm 0.015\%$	$0.45 \pm 0.02\%$	$0.36 \pm 0.02\%$	$0.138 \pm 0.019\%$	$0.382 \pm 0.009\%$
40-60 GeV	$0.426 \pm 0.015\%$	$0.50 \pm 0.03\%$	$0.33 \pm 0.02\%$	$0.16 \pm 0.02\%$	$0.359 \pm 0.009\%$
60-250 GeV	$0.278 \pm 0.012\%$	$0.271 \pm 0.018\%$	$0.171 \pm 0.013\%$	$0.186 \pm 0.017\%$	$0.228 \pm 0.007\%$

Table 6.13: The CMUP individual and weighted fake rates, with Z and W subtraction.

In Figures 6.1, 6.2 and 6.3 we can see the individual jet sample fake ratios plotted against each other for comparison purposes. From the differences between the ratios derived from various jet samples, we extract the systematic error associated with the

Bin	Jet 100	Jet 70	Jet 50	Jet 20	Weig. Av.
20-30 GeV	$0.308 \pm 0.008\%$	$0.276 \pm 0.011\%$	$0.325 \pm 0.012\%$	$0.078 \pm 0.011\%$	$0.251 \pm 0.005\%$
30-40 GeV	$0.240 \pm 0.010\%$	$0.247 \pm 0.016\%$	$0.205 \pm 0.015\%$	$0.040 \pm 0.011\%$	$0.168 \pm 0.006\%$
40-60 GeV	$0.193 \pm 0.010\%$	$0.210 \pm 0.016\%$	$0.226 \pm 0.017\%$	$0.077 \pm 0.015\%$	$0.176 \pm 0.007\%$
60-250 GeV	$0.125 \pm 0.008\%$	$0.114 \pm 0.012\%$	$0.117 \pm 0.011\%$	$0.066 \pm 0.010\%$	$0.108 \pm 0.005\%$

Table 6.14: The CMX individual and weighted fake rates, with Z and W subtraction.

Bin	Jet 100	Jet 70	Jet 50	Jet 20	Weig. Av.
20-30 GeV	$0.578 \pm 0.011\%$	$0.354 \pm 0.013\%$	$0.228 \pm 0.010\%$	$0.013 \pm 0.004\%$	$0.126 \pm 0.004\%$
30-40 GeV	$0.487 \pm 0.015\%$	$0.291 \pm 0.018\%$	$0.214 \pm 0.016\%$	$0.026 \pm 0.009\%$	$0.172 \pm 0.006\%$
40-60 GeV	$0.443 \pm 0.015\%$	$0.199 \pm 0.016\%$	$0.095 \pm 0.011\%$	$0.019 \pm 0.007\%$	$0.109 \pm 0.005\%$
60-250 GeV	$0.267 \pm 0.012\%$	$0.126 \pm 0.012\%$	$0.063 \pm 0.007\%$	$0.008 \pm 0.004\%$	$0.041 \pm 0.003\%$

Table 6.15: The CMU individual and weighted fake rates, with Z and W subtraction.

Bin	Jet 100	Jet 70	Jet 50	Jet 20	Weig. Av.
20-30 GeV	$0.497 \pm 0.010\%$	$0.744 \pm 0.018\%$	$0.454 \pm 0.014\%$	$0.093 \pm 0.012\%$	$0.395 \pm 0.006\%$
30-40 GeV	$0.423 \pm 0.014\%$	$0.513 \pm 0.023\%$	$0.404 \pm 0.02\%$	$0.043 \pm 0.011\%$	$0.251 \pm 0.008\%$
40-60 GeV	$0.359 \pm 0.014\%$	$0.371 \pm 0.022\%$	$0.257 \pm 0.019\%$	$0.071 \pm 0.014\%$	$0.246 \pm 0.008\%$
60-250 GeV	$0.224 \pm 0.010\%$	$0.231 \pm 0.017\%$	$0.211 \pm 0.014\%$	$0.073 \pm 0.011\%$	$0.171 \pm 0.006\%$

Table 6.16: The CMP individual and weighted fake rates, with Z and W subtraction.

Bin	Jet 100	Jet 70	Jet 50	Jet 20	Weig. Av.
20-30 GeV	$8.52 \pm 0.04\%$	$5.28 \pm 0.05\%$	$2.93 \pm 0.04\%$	$0.72 \pm 0.03\%$	$3.830 \pm 0.019\%$
30-40 GeV	$7.91 \pm 0.06\%$	$4.19 \pm 0.07\%$	$2.24 \pm 0.05\%$	$0.59 \pm 0.04\%$	$3.02 \pm 0.03\%$
40-60 GeV	$6.44 \pm 0.06\%$	$3.21 \pm 0.06\%$	$1.59 \pm 0.05\%$	$0.64 \pm 0.04\%$	$2.45 \pm 0.02\%$
60-250 GeV	$3.44 \pm 0.04\%$	$1.69 \pm 0.04\%$	$0.92 \pm 0.03\%$	$0.54 \pm 0.03\%$	$1.339 \pm 0.017\%$

Table 6.17: The CMIO individual and weighted fake rates, with Z and W subtraction.

fake rates. It should be noted that in spite of the fact that the differences are rather large, the fake background has a relatively small effect on the cross sections.

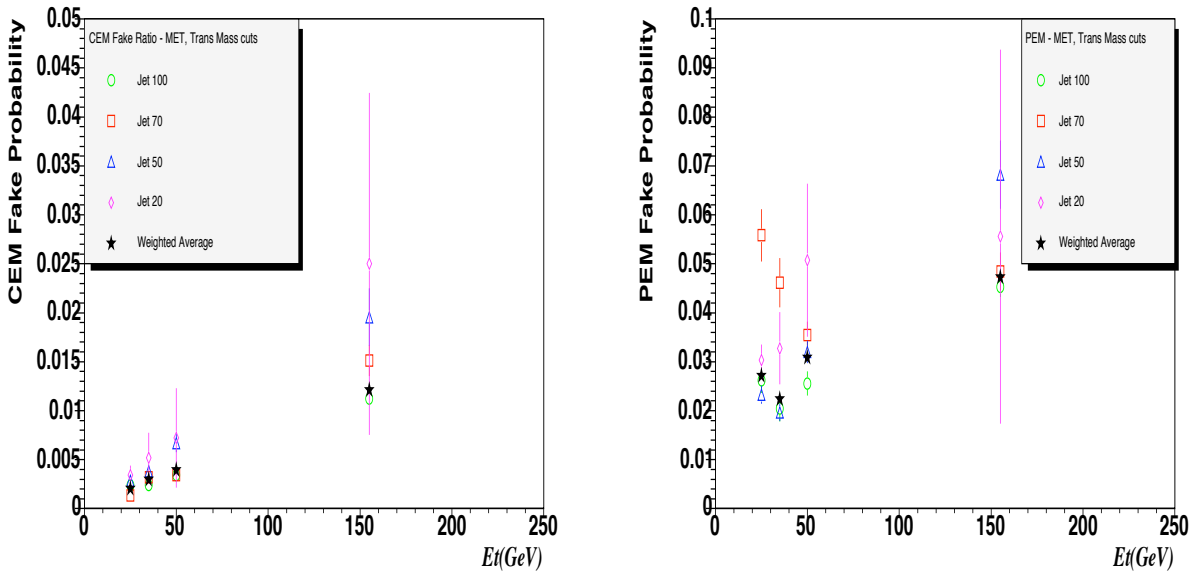

Figure 6.1: The CEM (left) and PHX (right) fake ratios.

6.4.3 Applying the Fake Rates to the W+jets Fakeable Data

To estimate the fake background we apply the fake rate probabilities to the W+jets data. For this, we select objects in W+jets events that have the same characteristics as the fakeable objects (denominator objects for the fake rate estimation) other than the lepton from the W. We use the W+jets data from the data samples listed in Table 6.18.

dataset ID	trigger requirement
bhel	high P_T electrons
bhmu	high P_T muons
ptop00	Forward Plug sample

Table 6.18: The samples used for extracting W+jets fakeable events.

In these data samples we select events with one tight lepton, according to our anal-

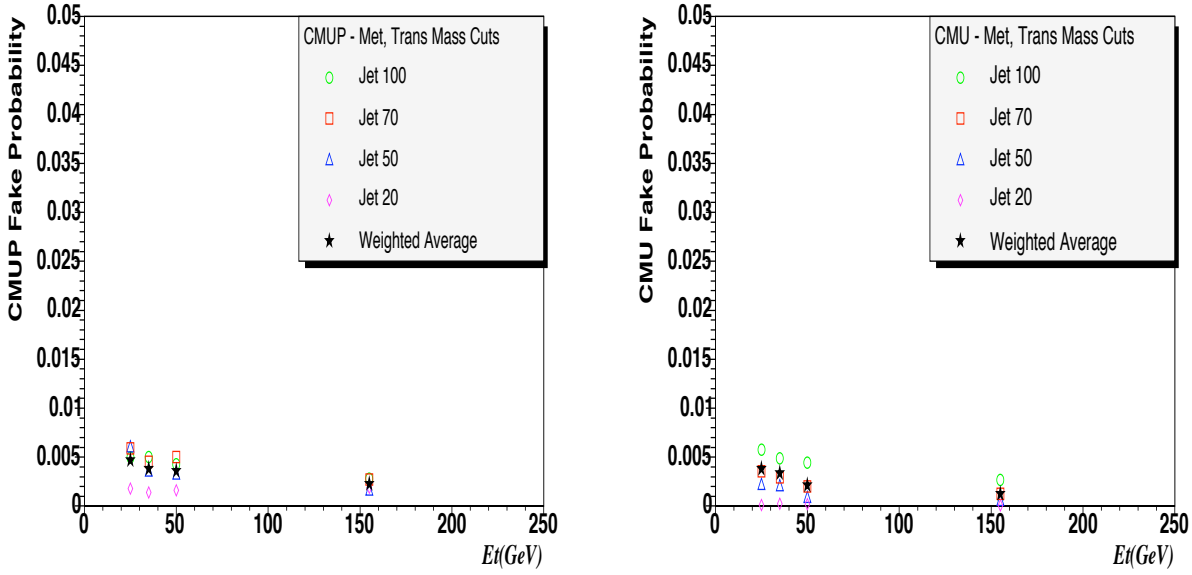

Figure 6.2: The CMUP (left) and CMU (right) fake ratios.

ysis lepton cuts definitions, and one or more fakeable object passing the denominator cuts. We then apply the dilepton analysis cuts such as the cosmic, and conversion cuts, the $\not\!\!E_T$ significance (for ee and $\mu\mu$ only) and the opposite sign cut. The fake ratio probabilities are folded in according to the fakeable event categories. For electrons the categories are uniquely separated so the weights are trivially applied. For muons we apply the different category weights to the same objects to obtain the background expectations for each muon category. The opposite sign cut is not applied to categories with phoenix electrons and instead the expectations are simply divided by two in those categories, given the high probability of charge mis-identification for the PHX electrons.

Similarly to the estimation of the fake rates, the Z^0 contamination is removed by cutting the events with dilepton invariant mass in the $66 < M_{\ell\ell} < 116$ GeV window. In Figures 6.4, 6.5 and 6.6 we see the dilepton invariant mass from the tight lepton and the fakeable lepton after the $\not\!\!E_T$ significance cut was applied for the ee and $\mu\mu$

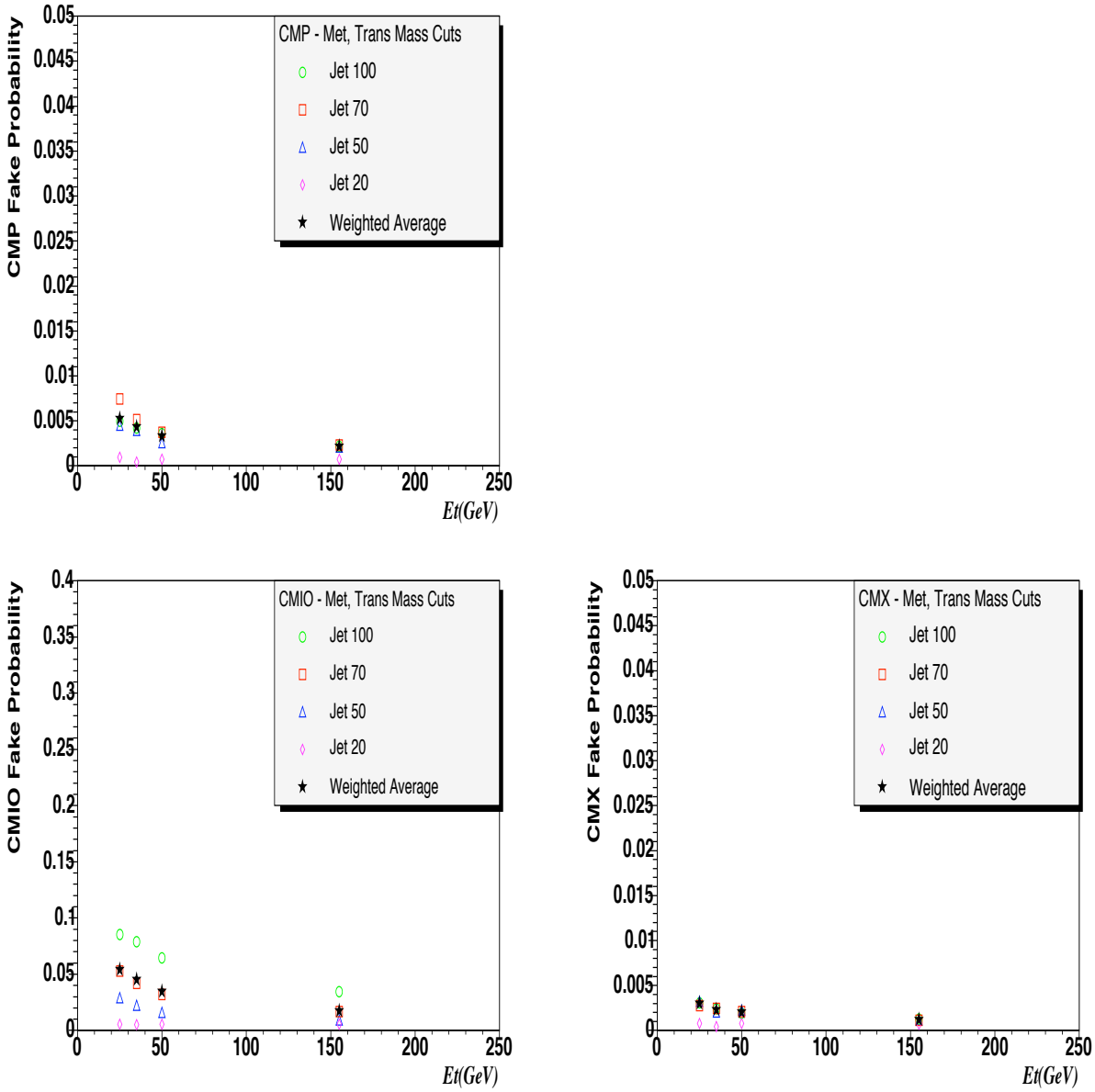

Figure 6.3: The CMP (top left), CMIO (bottom left) and CMX (bottom right) fake ratios.

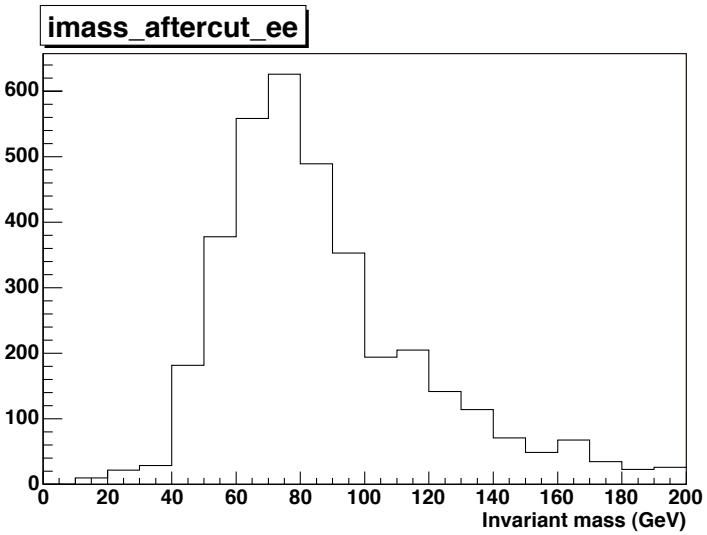

Figure 6.4: The ee invariant mass from the fake background. We use the "true" lepton from a W decay and the "fake" lepton.

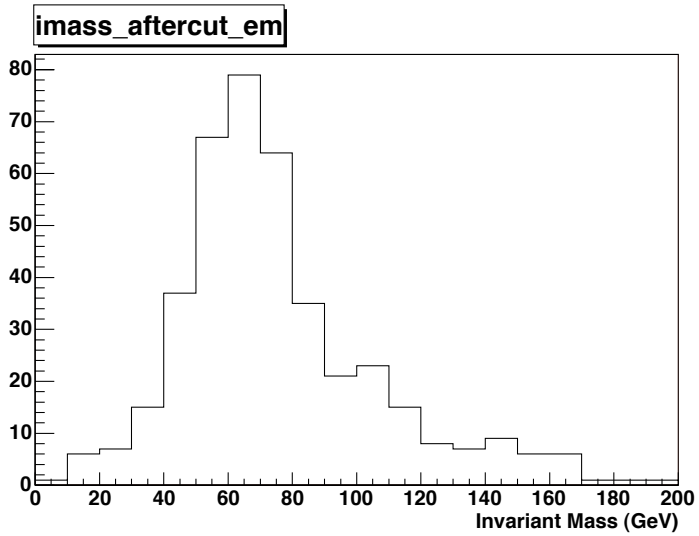

Figure 6.5: The $e\mu$ invariant mass from the fake background. We use the "true" lepton from a W decay and the "fake" lepton.

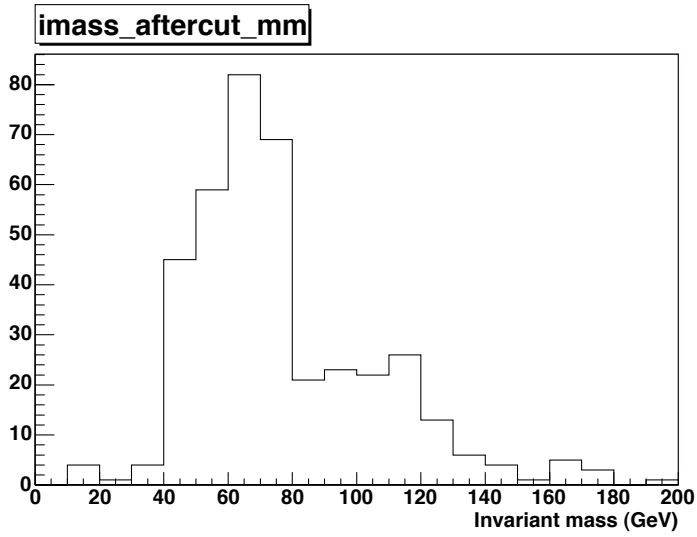

Figure 6.6: The $\mu\mu$ invariant mass from the fake background. We use the "true" lepton from a W decay and the "fake" lepton.

channels respectively, but before the Z^0 removal.

Care was taken to re-evaluate the $\not\!\!E_T$ and $\sum E_T$ corrections for fake dilepton events, as well as the number of jets distribution. The jets within a ΔR cone of 0.4 of the fake lepton are removed from the jet collection, and as a result from the $\not\!\!E_T$ correction and $\sum E_T$ calculation.

6.4.4 Fake Background Expectation and $\not\!\!E_T$-N_{jet} Phase Space Templates

After applying the fake rate to the fakeable events from W+jets data samples we obtain the expectation of the fake background as in Table 6.19, after each analysis cut. The first error is statistical and the second is the systematic error. For estimating the systematic error, the difference between the jet samples was used as a guide as derived from Figures 6.1 to 6.3. The difference in these fake rate estimates suggests an approximate systematic error of 100 %.

The Table 6.19 shows that this background is relatively small when compared to

the signal processes. We did a study where we increased this background in simulated experiments by a fraction significantly bigger than its systematic error and still do not see significant differences in the cross sections.

Category	ID+ISO	Conv+Cosm	metsig	OS
ee	14.08 ± 0.93	13.37 ± 0.90	4.48 ± 0.57	2.12 ± 0.39
$e\mu$	5.21 ± 0.46	5.17 ± 0.93	5.17 ± 0.93	3.05 ± 0.32
$\mu\mu$	8.58 ± 0.31	7.96 ± 0.30	3.28 ± 0.21	1.60 ± 0.15

Table 6.19: The estimated fake lepton background by dilepton category, after each analysis cut. The errors shown are statistical only. Systematic errors are 100% of the expected values.

For evaluating the $\not\!\!E_T$-N_{jet} phase space templates used in the fit, we used the same procedure as when estimating the expectations, with the event weights applied. The templates are shown in Figures 6.7, 6.8 and 6.9. It should be noted that in the ee and $\mu\mu$ templates the effect of the $\not\!\!E_T$ significance cut is to remove most of the events in the low $\not\!\!E_T$ region.

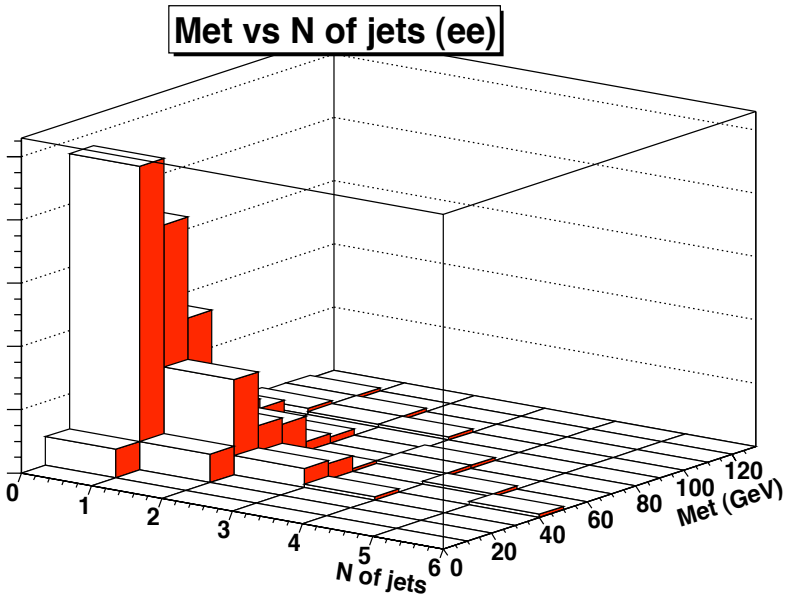

Figure 6.7: The ee fake background template.

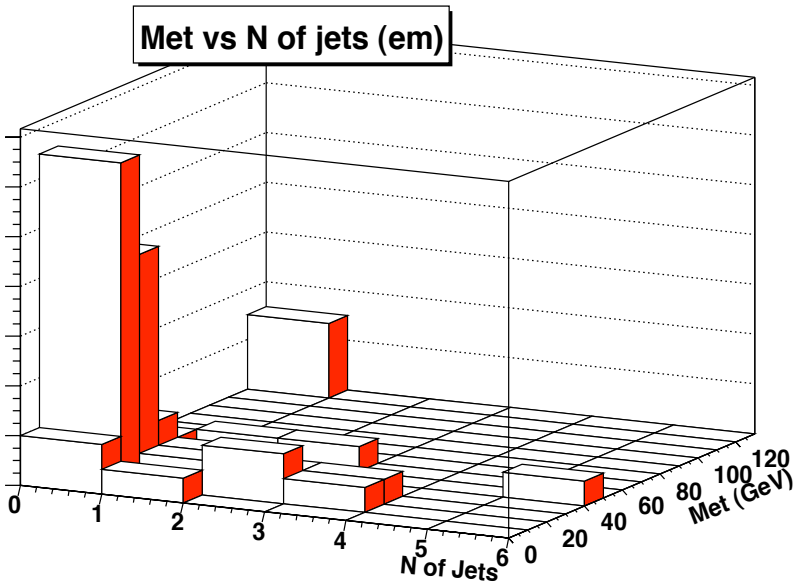

Figure 6.8: The $e\mu$ fake background template.

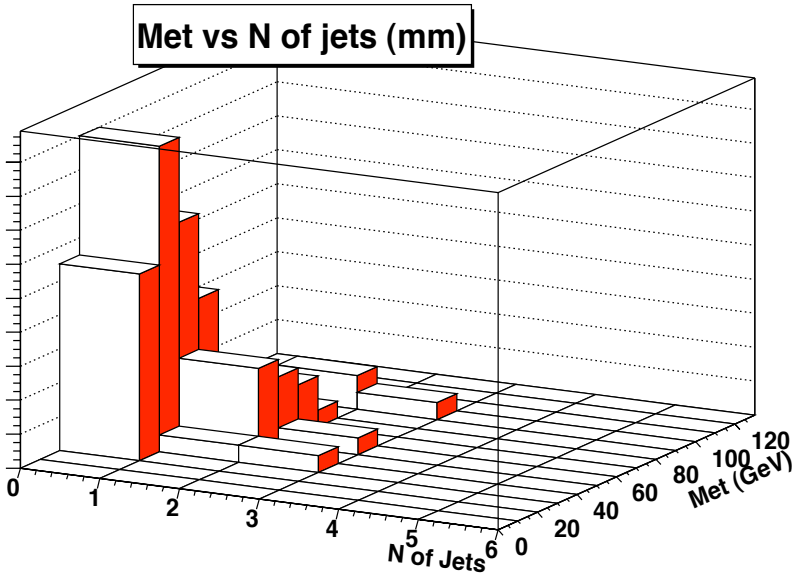

Figure 6.9: The $\mu\mu$ fake background template.

6.5 Systematic Uncertainties

We distinguish between: (a) the systematic errors that affect our signal and background acceptances, which are introduced in our fit through the use of Gaussian constrained parameters, with the width of the Gaussians set to the systematic errors, and, (b) systematic error sources that alter the shape of our $\not\!\!E_T$-N. of jets templates. These shape systematics are evaluated by doing so called "Pseudo-Experiments". In these Pseudo-Experiments, we use modified templates and simulate fits to Pseudo-data reconstructed from Monte Carlo events, we repeat this process a number of times, and then we take the shifts in the distributions of the fitted cross sections to estimate the systematic errors. We add in quadrature these latter sources of error to our final result errors. We are fortunate that our signal processes occupy very different regions of our phase space so that shape systematics are not a big issue.

In section 6.8 we will describe the shape systematic errors. We begin with the signal and background acceptance systematic errors.

6.5.1 The Signal Acceptance Systematic Uncertanties.

In this section we describe in more detail the sources of systematic error that affect our signal processes ($t\bar{t}$, WW and $Z \rightarrow \tau\tau$). The main sources of acceptance systematic error are listed below;

- The jet energy scale error.
- The initial and final state radiation error.
- The Monte Carlo generator associated uncertainties.
- The multiple interaction uncertainty.
- The lepton ID scale factor uncertainties.

- The track isolation systematic error.
- The parton distribution function (PDF) uncertainties.
- The $\not\!\!E_T$ significance cut uncertainty.

We now give a more detailed exposition of each of these systematic sources.

The Jet Energy Scale Systematic Errors.

Each of the seven levels of corrections that are applied to the jet energies, as described in Chapter 4, have an associated systematic uncertainty. For estimating the total uncertainty we use the maximal effect of all of these sources together. All of the sources of systematic errors are estimated in the CDF internal note 6419 [64].

In our analysis we do not cut on the number of jets, nevertheless, this source of systematic error enters our acceptance through the use of the $\not\!\!E_T$ significance cut in the ee and $\mu\mu$ channels, because this variable is dependent on the jet energies. There is no $\not\!\!E_T$ significance cut applied in the $e\mu$ dilepton channel. Therefore, there is no systematic error associated with this source in the events with $e\mu$ final states.

In Table 6.20 we see the effect of applying one standard deviation variation on the jet energy correction from the systematic error sources, in the acceptances. In Figure 6.10 the $\not\!\!E_T$ significance plots are shown without any variation and with one standard model deviation up and down for the $t\bar{t}$ and WW Monte Carlo samples. We extract the systematic errors from these variations, using the maximum difference from the unaltered acceptances.

The Initial and Final State Radiation Systematic Errors.

For $t\bar{t}$, the systematic effects due to QCD initial and final state radiation are estimated using Pythia samples generated with different QCD parton shower parameters, varied

Parameter	-1 σ Diff	+1 σ Diff	total
$t\bar{t}(ee)$	0.047 ± 0.035	0.056 ± 0.035	5%
$t\bar{t}(e\mu)$	0	0	0
$t\bar{t}(\mu\mu)$	0.048 ± 0.036	0.067 ± 0.036	6%
WW(ee)	0.005 ± 0.007	0.009 ± 0.007	1%
WW($e\mu$)	0	0	0
WW($\mu\mu$)	0.009 ± 0.008	0.013 ± 0.008	1%
Z$\rightarrow \tau\tau$ ($e\mu$)	0	0	0

Table 6.20: The Jet Energy Scale signal acceptance systematic error. The first number is the fractional variation in acceptance and the second the statistical error.

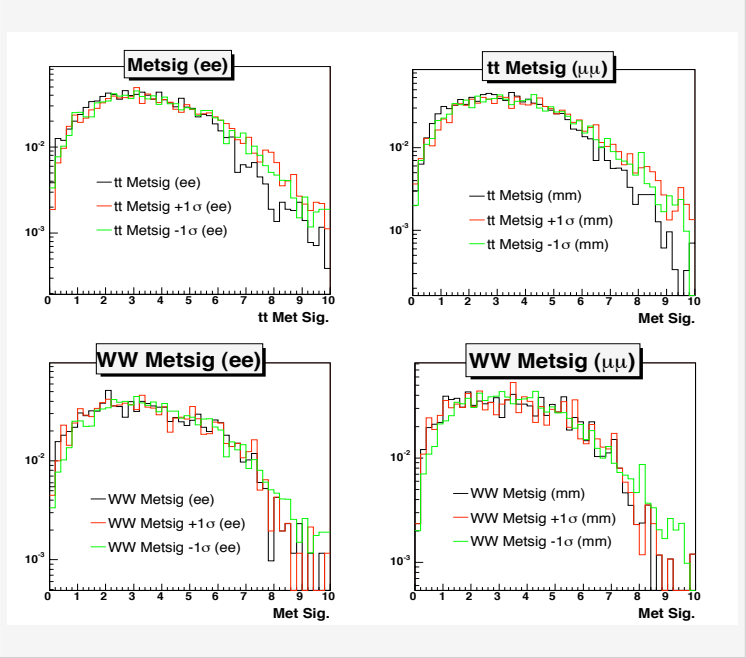

Figure 6.10: Missing energy significance from varying the jet energy scale by ± 1 σ, for $t\bar{t}$ and WW.

based on studies performed using Run II Drell-Yan data [65] and recommendations from the authors of PYTHIA. The $t\bar{t}$ samples used are: less-ISR(ttopbr), more-ISR(ttopdr), less-FSR(ttopfr) and more-FSR(ttopkr).

For WW a similar approach is followed with the samples produced being less-ISR and more-ISR. For the WW and $Z \rightarrow \tau\tau$ processes, there is no final state radiation. For the $Z \rightarrow \tau\tau$ process, we assume that the initial state radiation systematic error is of the same order as for WW, this because of the similarities in the initial state radiation mechanism in both processes.

In Table 6.21 we give the full estimations of our initial state radiation for our signal processes. In Table 6.22 we give the $t\bar{t}$ production final state radiation associated systematic error.

Parameter	Less ISR Diff.	More ISR Diff	error used
$t\bar{t}(ee)$	$-4.4 \pm 3.6\%$	$-8.2 \pm 3.6\%$	$+0\% - 8\%$
$t\bar{t}(e\mu)$	$-1.9 \pm 2.2\%$	$-4.0 \pm 2.2\%$	$+0\% - 4\%$
$t\bar{t}(\mu\mu)$	$0.4 \pm 3.8\%$	$-6.0 \pm 3.7\%$	$+0 - 6\%$
WW(ee)	5.3%	-7.2%	5%
WW($e\mu$)	6.3%	5.2%	5%
WW($\mu\mu$)	2.5%	6.4%	5%
Z$\rightarrow \tau\tau$ ($e\mu$)	—	—	5%

Table 6.21: The initial state radiation systematic errors. The numbers are the percentile variation due to the addition and substraction of ISR, the error is statistical.

Parameter	Less FSR Diff.	More FSR Diff.	error used
$t\bar{t}(ee)$	$-6.9 \pm 3.6\%$	$-1.0 \pm 4.5\%$	$+0\% - 7\%$
$t\bar{t}(e\mu)$	$-3.2 \pm 2.2\%$	$-0.4 \pm 2.7\%$	$+0\% - 3\%$
$t\bar{t}(\mu\mu)$	$-4.8 \pm 3.7\%$	$-4.5 \pm 4.6\%$	$+0\% - 5\%$

Table 6.22: The final state radiation systematic errors. The numbers are the percentile variation due to the addition and substraction of FSR, the error is statistical.

The Generator Systematic Errors.

The default $t\bar{t}$ acceptance is calculated using a PYTHIA (See Table 6.1) sample. PYTHIA does not fully treat spin correlations in its calculations. In contrast, HERWIG does include a full spin treatment. For that reason we take the difference between the acceptances resulting from both generators as a generator systematic error. There are other differences in the models used by both generators, including fragmentation and hadronization models. The HERWIG sample (CDF identification "ttophl") was generated with the same top mass, 178 GeV. We have to account for the known difference in the W leptonic branching fractions, as Pythia uses BR($W \to \ell\nu$ = 0.108), while HERWIG uses BR($W \to \ell\nu$ = 0.111). Therefore we reweigh the HERWIG acceptance by $(0.108/0.111)^2 = 0.947$ before comparing with PYTHIA.

The differences are consistent with the statistical uncertainties, as can be seen in Table 6.23, so we use no error from this source. We assume the error for WW and $Z \to \tau\tau$ are similarly small.

Parameter	Pythia sample	Herwig reweighed sample	Difference	Used
$t\bar{t}(ee)$	0.1439 ± 0.0035	0.1422 ± 0.0032	$-1.1 \pm 3.3\%$	0%
$t\bar{t}(e\mu)$	0.3988 ± 0.0059	0.3974 ± 0.0054	$-0.4 \pm 2.0\%$	0%
$t\bar{t}(\mu\mu)$	0.1363 ± 0.0034	0.1406 ± 0.0032	$3.1 \pm 3.5\%$	0%

Table 6.23: The $t\bar{t}$ generator systematic errors. The values are the acceptances, the errors are statistical.

The Multiple Interaction Systematic Errors.

Non inelastic $p\bar{p}$ soft interacting events are typically called minimum bias events, and have a high probability of occuring in th esame bunch crossing as an event of interest, resulting in multiple interaction events. In the $t\bar{t}$ sample we use for calculating acceptances, these additional interactions are not included.

To estimate the effect of multiple interactions on the $t\bar{t}$ signal acceptances, we

use two samples generated with one ("ttop5v") and two ("ttop7v") minimum bias events overlaid on the hard $t\bar{t}$ scattering. The choice for the relative fractions of these different samples was derived from a Poisson distribution with mean of 1.2, which represents the average number of extra minimum bias events expected. Using the Poisson distribution we have a 30% contribution from the sample with no minimum bias events, 36% for one minimum bias events and 34% for two or more minimum bias events. These proportions were used to weight the differences of the acceptances from the two extra minimum bias samples to the unaltered $t\bar{t}$ sample. The differences and the weighted error are given in Table 6.24.

Category	1 MB diff.	2 MB Diff.	Weighted error
ee	$-7.5 \pm 3.6\%$	$-12.5 \pm 3.4\%$	7%
$e\mu$	$-1.0 \pm 2.2\%$	$-2.9 \pm 2.1\%$	1.3%
$\mu\mu$	$-0.7 \pm 3.8\%$	$-6.1 \pm 3.5\%$	2.3%
total	$-2.9 \pm 2.8\%$	$-5.9 \pm 2.7\%$	$3.1 \pm 1.9\%$

Table 6.24: The $t\bar{t}$ multiple interaction systematic errors. The variations are in acceptance, the errors statistical.

The WW sample we use is already generated with the proper number of minimum bias events, so there is no systematic error associated with the WW acceptances from this source.

In the case of the $e\mu$ $Z \to \tau\tau$ production, we lack an extra minimum bias generated sample. Instead, We estimate the error by calculating the difference in acceptances of the $Z \to ee$ and $Z \to \mu\mu$ between samples with and without extra minimum bias events added. We then take the average of these differences and use them as the systematic error on the $Z \to \tau\tau$, given that these are all Drell-Yan processes. We have the results in Table 6.25.

Parameter	Exp. Without MB	Exp With MB	Diff	error used
$Z \rightarrow ee$	14539 ± 3	14270 ± 3	2%	—
$Z \rightarrow \mu\mu$	9551 ± 3	9276 ± 2	3%	—
$Z \rightarrow \tau\tau$	—	—	—	3%

Table 6.25: The $Z \rightarrow \tau\tau$ multiple interaction systematic errors. Values represent number of expected events just before applying the $\not\!\!E_T$ significance cut.

The Lepton Identification Factors Systematic Errors.

In Chapter 4 we described the lepton identification cuts. Discrepancies between data and Monte Carlo in the distributions of the variables the cuts are placed on, lead to systematic errors in the acceptances associated with such cuts. We combine the systematic errors of all the identification cuts into one. Additionally, there are errors associated with the various scale factors, as given in section 6.2.1, that we apply to our acceptances. Again, all the errors from these sources are folded together event by event. In Table 6.26 we show the combined systematic errors.

Source	$t\bar{t}(ee)$	$t\bar{t}(e\mu)$	$t\bar{t}(\mu\mu)$	WW(ee)	WW($e\mu$)	WW($\mu\mu$)	Z$\rightarrow \tau\tau$ ($e\mu$)
lepton SF	3%	3%	2%	4%	3%	2%	3%

Table 6.26: The lepton scale factor systematic errors. Includes lepton ID, trigger efficiency, PHX charge miss-identification scale factors and Monte Carlo reconstruction scale factors.

The Track Isolation Systematic Error.

We separate the systematic error introduced by the track isolation cut, and that from the lepton identification efficiencies systematic error because this cut is not commonly applied as a lepton cut by other CDF measurements. The error is obtained from the comparison of data and Monte Carlo track isolation scale factors. The result is a 1% error per lepton, which translates into a 2% error on all of our acceptances.

The Parton Distribution Functions (PDF) Systematic Errors.

The parton distribution functions are used by the Monte Carlo generator programs such as PYTHIA and HERWIG. The evaluation of the PDF uncertainty is done using the CTEQ6M PDF set [34]. This group contains a set of 40 complementary PDF sets CTEQ6M.01...CTEQ6M.40, each of which represents different variations in each of the twenty eigenvectors (corresponding to 20 free parameters used in the PDF). They form an orthonormal basis spanning the full PDF parameter space. Each event in PYTHIA signal processes is reweighed with the ratio of the CTEQ6M PDF values and the CTEQ6M.xx PDF values. The systematic error is taken to be the biggest variation on the acceptances.

We found the error to be consistent with a 1% variation on the acceptances.

The $\not\!\!E_T$ Significance Cut Systematic Errors.

The $\not\!\!E_T$ significance cut affects mostly the Drell-Yan background. However, it still cuts a small portion of the $t\bar{t}$ and WW contributions in the ee and $\mu\mu$ channels. Deficiencies in modeling of this variable by the Monte Carlo leads to a systematic error in the acceptance. To estimate the systematic error on the signal acceptances, we use W+jets data events by selecting data events with 1 lepton and $\not\!\!E_T > 25$ GeV, and comparing them with W Monte Carlo. The error on the $\not\!\!E_T$ significance is then the ratio of the cut efficiencies in data and Monte Carlo selected samples. From these comparisons we conclude that the error for events with real $\not\!\!E_T$ sources (our $t\bar{t}$ and WW signal processes) is of the order of 3%.

Additional Acceptance Systematic Error Sources

There are other sources of systematic errors, most important among them is the luminosity systematic error, which is 6% [66]. The integrated luminosity, calculated

Source	$t\bar{t}(ee)$	$t\bar{t}(e\mu)$	$t\bar{t}(\mu\mu)$	WW(ee)	WW($e\mu$)	WW($\mu\mu$)	Z$\rightarrow \tau\tau$ ($e\mu$)
JES	5%	0	6%	1%	0	1%	0
ISR	$+0-8\%$	$+0-4\%$	$+0-6\%$	5%	5%	5%	5%
FSR	$+0-7\%$	$+0-3\%$	$+0-5\%$	na	na	na	na
PDF	1%	1%	1%	1%	1%	1%	1%
Mult. Int.	3%	3%	3%	0%	0%	0%	3%
Lepton SF	3%	3%	2%	4%	3%	2%	3%
Track Iso	2%	2%	2%	2%	2%	2%	2%
Metsig cut	3%	0	3%	3%	0	3%	0
total	$+8-13\%$	$+5-7\%$	$+8-11\%$	7%	6%	7%	7%
error used	13%	7%	11%	7%	6%	7%	7%

Table 6.27: Signal acceptance systematic summary. Note some errors are asymmetric, which result in an asymmetric total, however, we used the largest error (symmetrized) in our fit.

from the readings of the Cherenkov luminosity counters, can have various sources of uncertainties, including detector calibration, instability and uncertainties in the $p\bar{p}$ inelastic cross section, among others.

Summary of Signal Acceptance Systematic Errors

In Table 6.27 we summarize all of our sources of signal acceptance systematic error and give the total combined error by signal process and decay channel. We use the largest value in each of our asymmetric estimations.

6.5.2 Background Systematic Uncertainties

Our backgrounds processes have similar systematic errors as our signal acceptances. However there are 3 type of errors that contribute to the error significantly for the backgrounds; the fake systematic error of about 100% on the fake background, the considerable statistical error on the $W\gamma$ Monte Carlo samples, and the error associated with the $\not\!\!E_T$ significance cut for the Drell-Yan background in the ee and $\mu\mu$ channels.

To estimate the Drell-Yan $\not\!\!E_T$ significance cut systematic error, we use the difference in the $\not\!\!E_T$ significance distributions from the data after subtracting the WW, $t\bar{t}$ and $Z \rightarrow \tau\tau$ contributions, from Drell-Yan contributions, inside the Z^0 window ($76 < M_{\ell\ell} < 106$ GeV). A comparison of those distributions can be seen in the Figure 6.11. We don't have much statistics left in the data after a $\not\!\!E_T$ significance value of about 2.5. Instead we look at the ratio of the cut efficiencies just below 2.5 (see Figure 6.12) of data to Monte Carlo as a measure of the systematic error, and extrapolate the ratio to higher values of $\not\!\!E_T$ significance. From these ratios of cut efficiencies, we estimate a 20% error in both the ee and $\mu\mu$ channels.

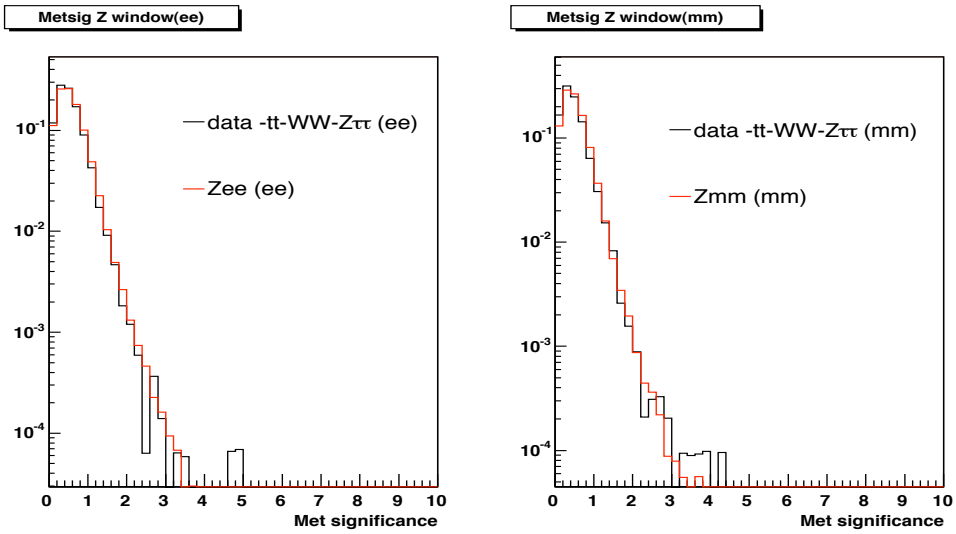

Figure 6.11: The ee and $\mu\mu$ met significance inside the Z^0 window. The WW, $t\bar{t}$ and $Z \rightarrow \tau\tau$ contributions were subtracted from the data.

In Table 6.28 we summarize all sources of errors in the background, and give the total errors in our background acceptances and expectations. As mentioned already, the dominating errors are the Drell-Yan $\not\!\!E_T$ significance cut systematic error, the fake background systematic error and the $W\gamma$ statistical error.

Process	Number of events in 360 pb^{-1}	Syst. error (%)	Statistical error (%)	Total error (%)	Total error (events)
Zee (ee)	15.38	20%	6%	21%	3.2
$Z \to \tau\tau$ (ee)	1.06	20%	8%	22%	0.2
WZ (ee)	1.26	5%	5%	7%	0.09
ZZ (ee)	0.47	5%	5%	7%	0.03
Wγ (ee)	1.77	30%	24%	38%	0.7
fakes (ee)	2.12	100%	17%	101%	2.2
total (ee)	22.06	–	—	29%	±6.4
Z$\mu\mu$ ($e\mu$)	9.25	5%	8%	9%	0.8
WZ ($e\mu$)	0.7	5%	7%	9%	0.06
ZZ ($e\mu$)	0.07	5%	13%	14%	0.01
Wγ ($e\mu$)	1.23	30%	24%	38%	0.5
fakes ($e\mu$)	3.05	100%	10%	100%	3.1
total ($e\mu$)	14.3	—	—	31%	±4.5
Z$\mu\mu$ ($\mu\mu$)	11.59	20%	7%	21%	2.4
$Z \to \tau\tau$ ($\mu\mu$)	0.61	20%	10%	22%	0.1
WZ ($\mu\mu$)	1.11	5%	5%	7%	0.08
ZZ ($\mu\mu$)	0.42	5%	6%	8%	0.03
fakes ($\mu\mu$)	1.60	100%	9%	100%	1.6
total ($\mu\mu$)	15.33	—	—	27%	±4.2
luminosity	360 pb^{-1}	6%	—	6%	—

Table 6.28: Systematic and statistical errors on the fixed backgrounds and the integrated luminosity.

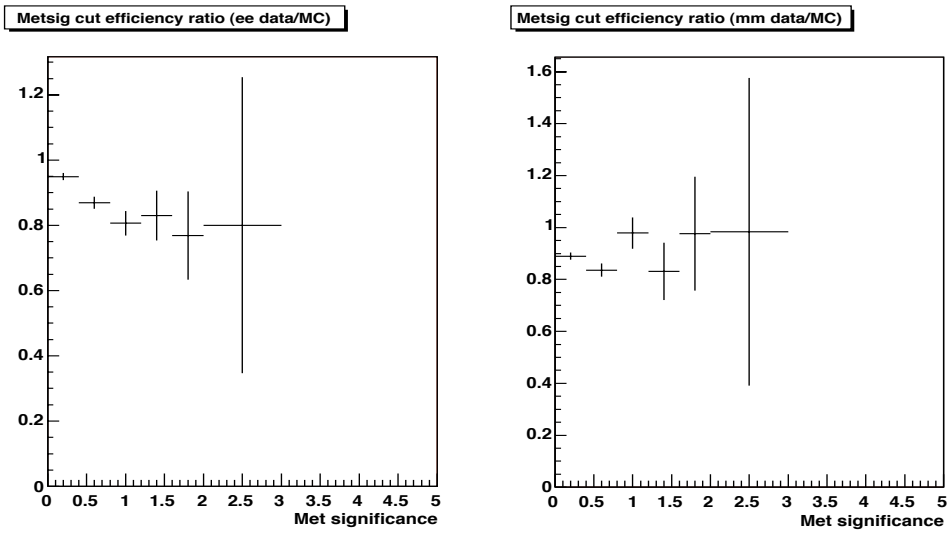

Figure 6.12: The *ee* and $\mu\mu$ ratio of the Monte Carlo to data $\not\!\!E_T$ significance cut efficiency as a function of the cut value

6.6 The Data Events and Grand Summary of the Standard Model Expectations

We select data events using version 7 of the good run list from the CDF Top, Electroweak and Exotics group [1]. This covers all the runs numbers up to 186598 and does not include a number of runs where the COT was experiencing malfunctions that represent about a 50 pb^{-1} data loss. We note the following:

- In the *ee* channel we apply the good run list without muon requirements.
- We apply the good run list without silicon detector checks to the events that do not contain a PHX electron.
- For dilepton events with a PHX electron (TCE-PHX, CMUP-PHX and CMX-PHX), the good run list with silicon detector checks was used.

[1] http://www-cdf.fnal.gov/internal/dqm/goodrun/v7/goodv7.html

Because we do make these different good run requirements depending on the type of objects we have in the event, the total integrated luminosity depends on the dilepton category. In Table 6.29 we give the breakdown of integrated luminosity by dilepton category.

Dilepton Combination Type	Good Run List	Offline $\mathcal{L}_{int}$ (pb^{-1}) +1.9% correction and ±5.9% errors
TCE-TCE	1001	374 ± 22
PHX-{TCE, PHX}	1101	343 ± 21
TCE-{CMUP, CMU, CMP, CMIO}	1031	366 ± 22
TCE-CMX	1021	333 ± 20
PHX-{CMUP}	1131	337 ± 20
PHX-CMX	1121	310 ± 19
CMUP-{CMUP, CMU, CMP, CMIO}	0031	378 ± 23
CMX-{CMUP, CMX, CMU, CMP, CMIO}	0011	339 ± 20

Table 6.29: Integrated luminosities of the different dilepton categories used in the analysis.

.

Each physics process has a different proportion of expected number of events depending on the dilepton categories (see appendix D), then each physics process is weighted with a different integrated luminosity. Using the integrated luminosities from Table 6.29, together with the relative dilepton category acceptances in our signal processes, gives us:

for $t\bar{t}$

$$\mathcal{L} = (360 \pm 22)\,\mathrm{pb}^{-1}$$

for WW

$$\mathcal{L} = (358 \pm 21)\,\mathrm{pb}^{-1}$$

for $Z \rightarrow \tau\tau$

$$\mathcal{L} = (355 \pm 21)\,\mathrm{pb}^{-1}$$

We process the data through the same analysis cuts as we applied when calculating the acceptances. Table 6.30 shows the number of events surviving after each analysis selection requirement.

Category	ID+CAL ISO	Conv+Cosm	$\not\!\!E_T$sig	OS
TCE-TCE	7389	6781	15	14
TCE-PHX	7974	7642	14	10
ee	15363	14423	29	24
TCE-CMUP	49	44	44	44
TCE-CMU	8	6	6	6
TCE-CMP	12	11	11	11
TCE-CMX	17	15	15	15
TCE-CMIO	14	13	13	12
PHX-CMUP	17	15	15	6
PHX-CMX	14	14	14	9
eμ	131	118	118	103
CMUP-CMUP	2985	1946	6	5
CMUP-CMU	960	822	3	3
CMUP-CMP	1483	1041	8	8
CMUP-CMX	1822	1792	6	6
CMUP-CMIO	2081	1937	5	5
CMX-CMX	607	546	2	1
CMX-CMU	501	449	0	0
CMX-CMP	498	489	0	0
CMX-CMIO	883	838	1	1
$\mu\mu$	11820	9860	31	29

Table 6.30: Number of events in about 360 pb^{-1} of Run II data, after the requirement of 2 opposite-sign isolated high-P_T leptons. The ee and $\mu\mu$ channels have an additional $\not\!\!E_T^{sig}$ requirement.

6.6.1 Grand Summary Table

In Table 6.31 we show a summary of all the signal and background Standard Model expectations presented in the previous sections. Statistical and acceptance systematic errors are included. Shown for comparison is the number of observed data events in each channel.

	$e\mu$	ee	$\mu\mu$	$\ell\ell$
"Signal" processes				
$t\bar{t}$	10.0 ± 0.7	3.6 ± 0.5	3.4 ± 0.4	17.0 ± 1.6
WW	13.8 ± 0.8	5.2 ± 0.4	4.3 ± 0.3	23.3 ± 1.5
$Z \to \tau\tau$	57.8 ± 4	1.1 ± 0.2	0.6 ± 0.1	59.5 ± 4.3
"Background" processes				
$DY \to ee$	0	15.4 ± 3.2	0	15.4 ± 3.2
$DY \to \mu\mu$	9.3 ± 0.8	0	11.6 ± 2.4	20.8 ± 3.2
WZ	0.70 ± 0.06	1.26 ± 0.09	1.11 ± 0.08	3.07 ± 2.3
ZZ	0.07 ± 0.01	0.47 ± 0.03	0.42 ± 0.03	0.96 ± 0.07
$W\gamma$	1.2 ± 0.5	1.8 ± 0.7	0	3.0 ± 1.2
$W + j$	3.05 ± 3.05	2.12 ± 2.12	1.60 ± 1.60	6.8 ± 6.8
Total expected "Signal + Background" event count				
	96 ± 5	31 ± 4	23 ± 3	150 ± 12
"CDF Data"				
Data	103	24	29	156

Table 6.31: Grand summary of expected and observed numbers of events in $\sim 360\,\mathrm{pb}^{-1}$ of data

6.6.2 $\not\!\!E_T$ vs N_{jet} Jets Distributions

In Figures 6.13- 6.15 are the ee, $e\mu$ and $\mu\mu$ templates, which are used to measure the $t\bar{t}$, WW and $Z \to \tau\tau$ cross sections. Our data phase space $\not\!\!E_T$-N_{jet} distributions are composed of 103 $e\mu$ events, 24 ee events, and 29 $\mu\mu$ events, we use these events to fit the Standard Model processes to the data. Additionally, in appendix B we show various data kinematic distributions compared with the Standard Model expectations from our Monte Carlo samples.

6.7 Fitting Technique

To fit the Standard Model to the data, we use a maximum likelihood method. Our likelihood function is derived from the Poisson probabilities, comparing bin by bin in the $\not\!\!E_T$-N_{jet} space, of the data observed number of events when compared with the Standard Model expectations. We minimize the negative of the logarithm of this

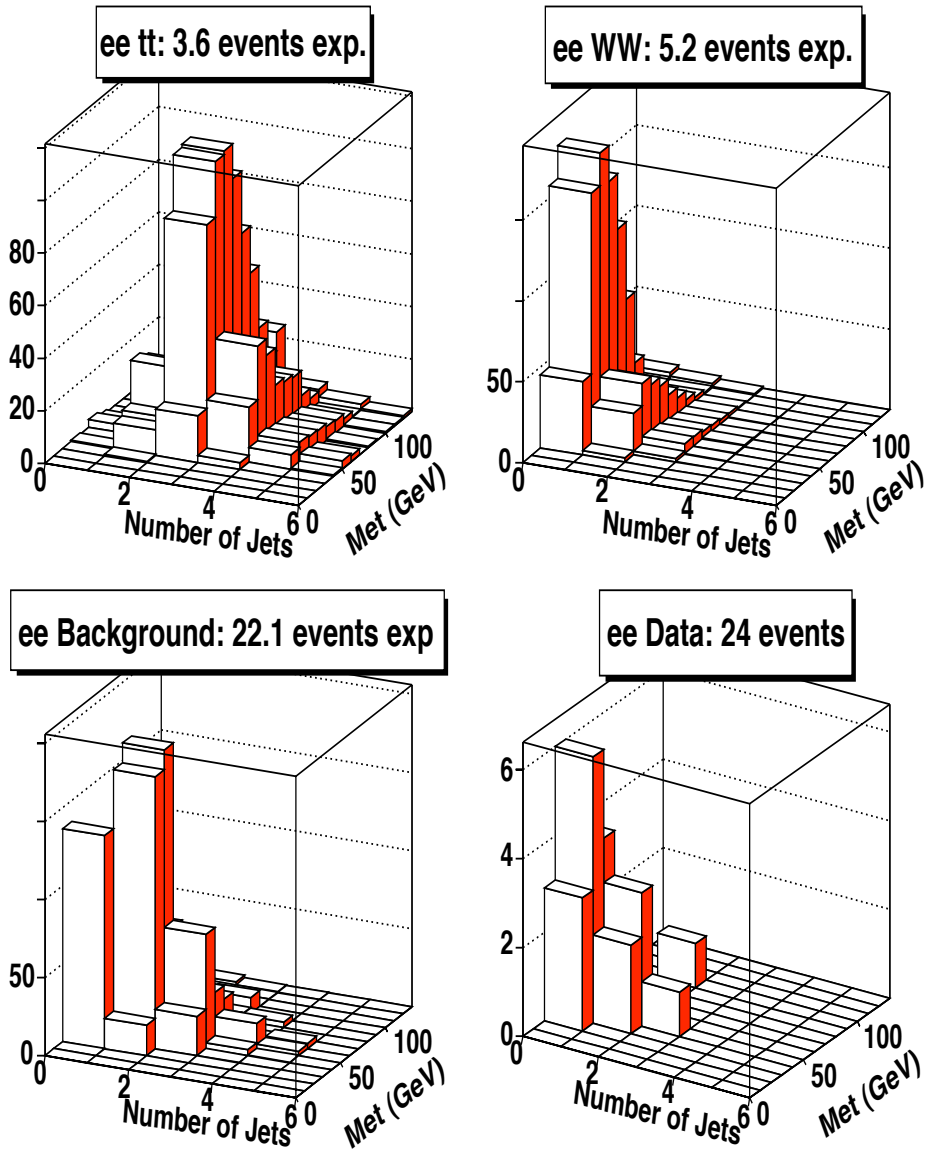

Figure 6.13: The ee 2-D $\not\!\!E_T$-N_{jet} distributions for the SM "signal" sources, "background" sources (summed together) and from 360 pb^{-1} of data.

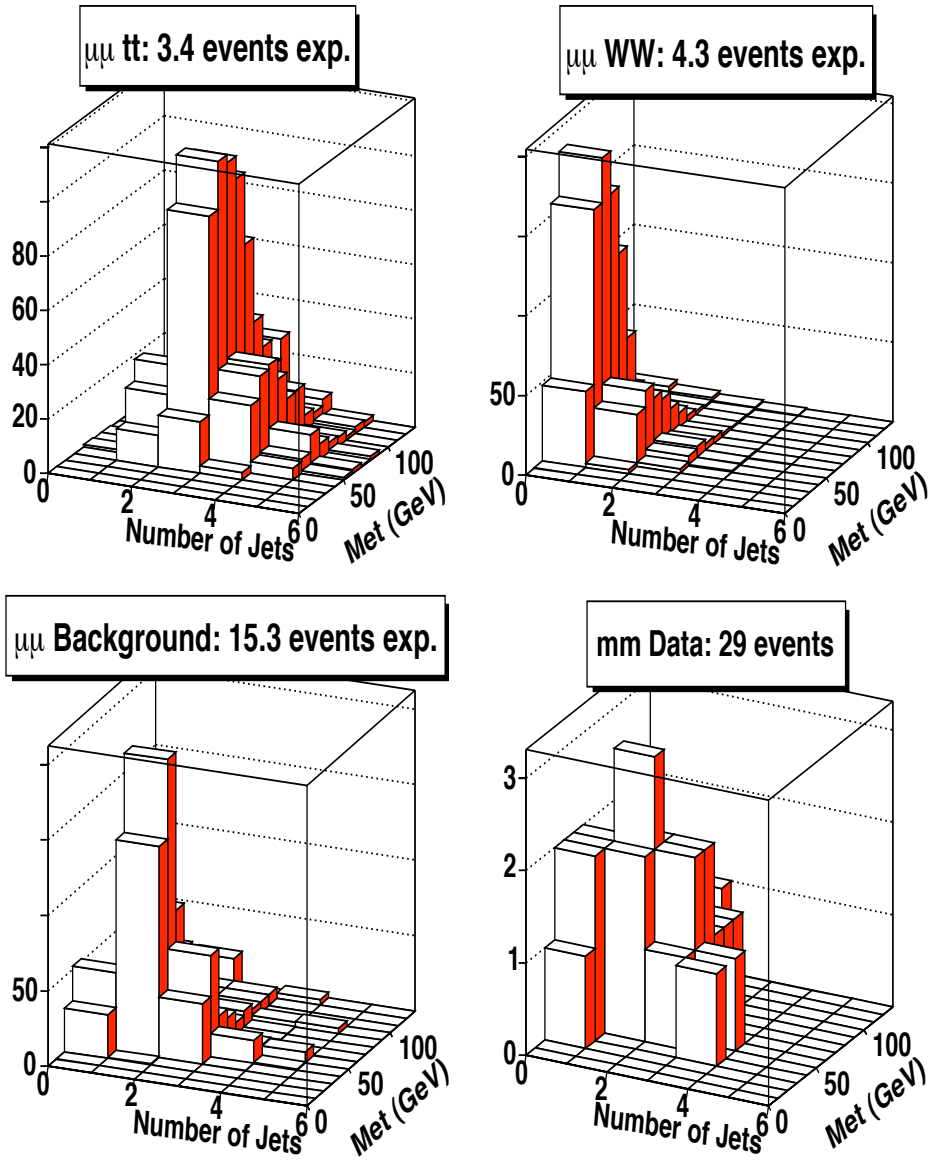

Figure 6.14: The $\mu\mu$ 2-D $\not\!\!E_T$-N_{jet} distributions for the SM "signal" sources, "background" sources (summed together) and from 360 pb^{-1} of data.

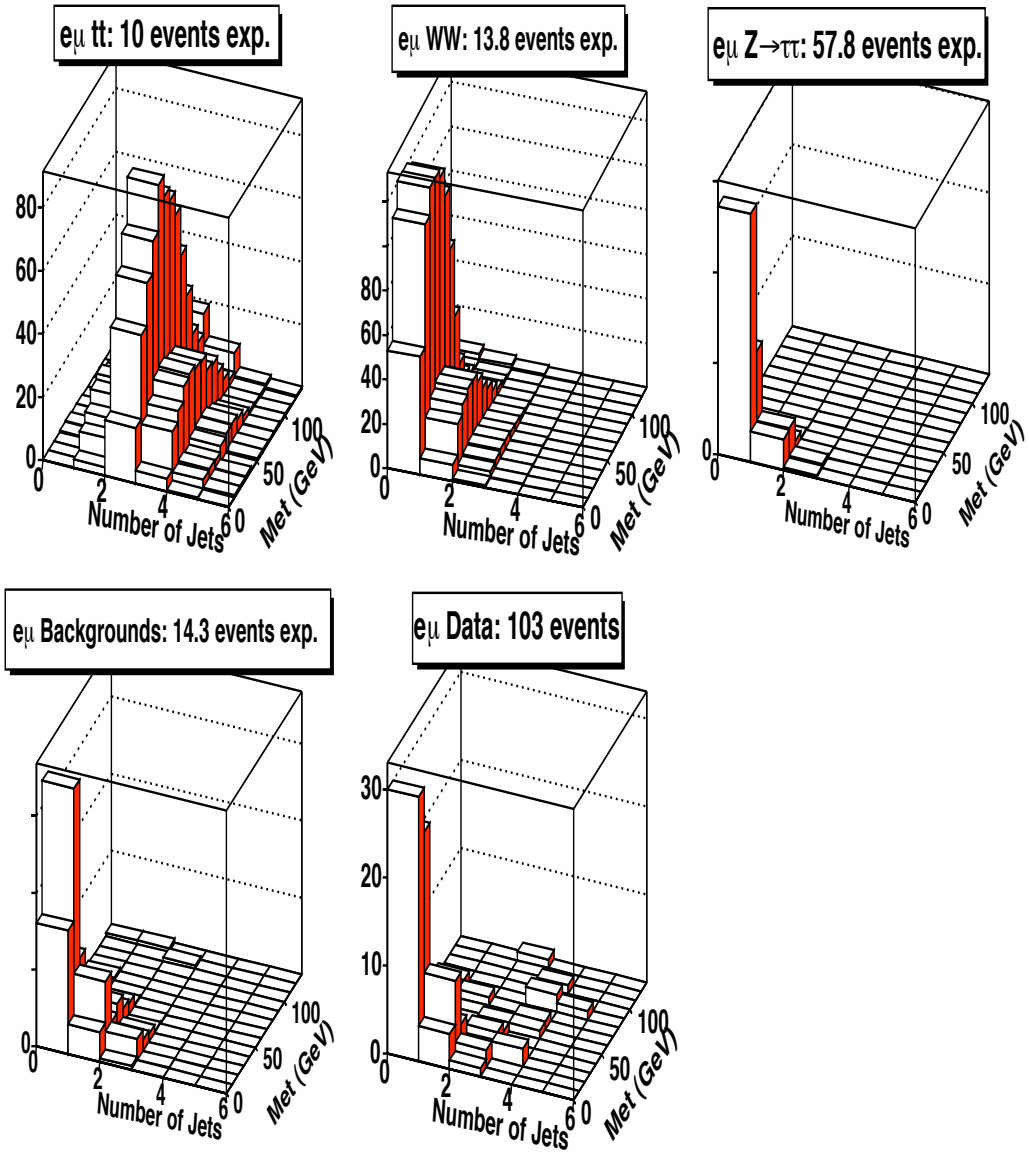

Figure 6.15: The $e\mu$ 2-D $\not\!\!E_T$-N_{jet} distributions for the SM "signal" sources, "background" sources (summed together) and from 360 pb^{-1} of data.

likelihood function, and measure the Standard Model cross sections. In reference [67] we give a detailed description of this method.

If we take into account only the Standard Model contributions, the data $\not\!\!E_T$-N. of jets distribution must be given by:

$$\frac{\partial^2 N}{\partial \not\!\!E_T \partial N_{jet}} = \alpha N_{t\bar{t}} + \beta N_{WW} + \gamma N_{Z\to\tau\tau} + n_{other} \tag{6.4}$$

Where the $t\bar{t}$, WW and $Z \to \tau\tau$ distributions (N_i) are normalized to 1, and the parameters α, β and γ are the number of events from each contribution, and are related to the respective cross sections through

$$\begin{aligned} \alpha &= \sigma_{t\bar{t}} A_{t\bar{t}} \mathcal{L} \\ \beta &= \sigma_{WW} A_{WW} \mathcal{L} \\ \gamma &= \sigma_{Z\to\tau\tau} A_{Z\to\tau\tau} \mathcal{L} \end{aligned} \tag{6.5}$$

where σ is the cross section, A is total acceptance including the branching ratios, and $\mathcal{L}$ is the weighted integrated luminosity (from the numbers presented in the previous section).

The distributions of the "other" Standard Model sources are normalized and fixed to the number of expected events, as given in Table 6.31. We begin with a likelihood function defined by:

$$L = \prod_i \rho_i \tag{6.6}$$

where i runs over all bins in our 2-D distributions, and where

$$\rho_i = \frac{\mu_i^{n_i} e^{-\mu_i}}{n_i!} \tag{6.7}$$

Here n_i is the data distribution bin content for bin "i" and μ_i is the corresponding

total expected number given by:

$$\mu_i = \alpha N_{t\bar{t}_i} + \beta N_{WW_i} + \gamma N_{Z\to\tau\tau_i} + n_{other_i} \tag{6.8}$$

If we minimize $-ln(L)$ as a function of α, β and γ, we can find the respective "best fit" contributions to the data sample. We use the logarithm of the likelihood, so that the numbers we get are easier to compute, as otherwise the numbers become too large. This also means that the product over the Poisson probabilities becomes a summation. We multiply by -1 in order to use minimization programs, and while maximizing the likelihood.

The actual form of the likelihood function we use for our fit is more complex than what was presented because we have to account for systematic errors in all the acceptances, and the integrated luminosity. We do this by adding Gaussian constraints for each acceptance and the integrated luminosity. That is, the Likelihood function in equation (6.6) is multiplied by terms of the form:

$$G_f = e^{-\frac{(A_f - \hat{A}_f)^2}{2\sigma^2_{A_f}}} \tag{6.9}$$

where, f refers to a given acceptance (or the integrated luminosity) for each source. $\hat{A}_f$ is its expected value, σ_{A_f} is its uncertainty, and A_f is its value in the fit that is allowed to float only insofar that G_f doesn't significantly reduce the Likelihood.

In the minimization program, α, β and γ are of the form:

$$\alpha_i = \sigma_i A_i \mathcal{L} \tag{6.10}$$

In effect we add to the $-ln(L)$ terms like the following for each constrained parameter:

$$-ln(L) + \frac{(A_i - \hat{A}_i)^2}{2\sigma^2_{A_i}} + ... \tag{6.11}$$

Then, when our minimization program computes the errors on the cross section parameters, they also include the acceptance and luminosity systematic errors.

When including all dilepton final state channels (ee, $e\mu$ and $\mu\mu$) we build the likelihood function in a similar way and then we combine the likelihood functions for each channel. Then we fit the Standard Model to the data in all three channels at the same time.

For the minimization program, we use the MINUIT package [68]. In Table 6.32 we show the successive steps in our minimization program, which are a fairly standard procedure. First we apply a rough Metropolis Monte Carlo minimization, which is a rough minimization with variable step size. This minimization has the ability to jump through barriers in the likelihood function to get near the global minimum, and does not get stuck in a local minimum. Our likelihood function is well behaved, but this insures getting close to the global minimum in any case. Then we apply a more refined minimization method, of fixed step, the most precise algorithm available in the MINUIT package, called the MIGRAD algorithm, which finds the values that maximize the likelihood for each of our fit parameters. Finally we can apply the MINOS algorithm, which makes an asymmetric error analysis by fluctuating the parameters around the minimum. We obtain from the MINOS algorithm asymmetric errors on all of the parameters, a correlation matrix between parameters, and can create contour plots for standard deviation confidence level regions in the cross section space. For more information on MINUIT algorithms see reference [68].

Metropolis MC of variable step size
MIGRAD minimization
MINOS error analysis

Table 6.32: Minimization steps used in the fit.

6.7.1 Extracting the $t\bar{t}$ and WW Cross Sections from the eμ Data

For the $e\mu$-only fit, we assume 100% correlation between the signals ($t\bar{t}$, WW and $Z \to \tau\tau$), as in general if the $e\mu$ acceptance goes in one direction for a given process it should do so for all processes, to first order. Although this won't be precisely true, we have seen that changing the correlations has little effect (less than 2%) on the fitted cross sections and their errors.

The $e\mu$ fit is an 8 parameter fit, with the following parameters:

- $\mathcal{L}$ - Gaussian constrained;
- $\sigma_{t\bar{t}}$, σ_{WW}, $\sigma_{Z\to\tau\tau}$ - floating;
- $\epsilon_{t\bar{t}}(e\mu)$, $\epsilon_{WW}(e\mu)$, $\epsilon_{Z\to\tau\tau}(e\mu)$ - Gaussian constrained;
- $B_{e\mu}$ - Gaussian constrained;

where ϵ_{signal} are the expected acceptance, while $B_{<ch>}$ represents the background in the channel $< ch >$.

There are acceptance errors which are correlated between different signal samples (jet energy scale, ISR, lepton identification, etc). For simplicity, we assumed 100% correlation between the errosr on the acceptances across samples and compared the outcome with an uncorrelated fit. The correlations are included into the fit as follows:

- Express the signal acceptances as

$$A_l = A(0)_l * (1 + f_l * \delta_l), \tag{6.12}$$

  where $A(0)_l$ is the expected acceptance, f_l is the relative error on acceptance ($\delta A_l / A_l$) and δ_l is a Gaussian G(0,1).

- The contribution to the total expected number of events from the signals is

$$\mu_{ijl} = \sigma_l * \mathcal{L} * A_l * k_{ij} \tag{6.13}$$

where l loops over signal ($t\bar{t}$, WW, $Z \rightarrow \tau\tau$), i loops over $\not\!\!E_T$ bins, while j over N. of jets bins. k_{ij} is the number of events in bin ij, of the normalized templates.

- Assuming 100% correlated errors, all three signal acceptances must be constrained with the same Gaussian:

$$\begin{aligned} \mu_{ij} = k_{ij} * \sigma_{t\bar{t}} * \mathcal{L} * A(0)_{t\bar{t}}(1 + f_{t\bar{t}} * \delta) + \\ k_{ij} * \sigma_{WW} * \mathcal{L} * A(0)_{WW}(1 + f_{WW} * \delta) + \\ k_{ij} * \sigma_{Z\rightarrow\tau\tau} * \mathcal{L} * A(0)_{Ztt}(1 + f_{Z\rightarrow\tau\tau} * \delta) \end{aligned} \tag{6.14}$$

where δ is constrained by a Gaussian (0,1), $\mathcal{L}_{int}$ by a Gaussian ($\mathcal{L}_\prime, \delta\mathcal{L}_\prime$) and σ's are floating and fitted for.

Then the it can be applied to extract the $t\bar{t}$ and WW cross sections in the $e\mu$ channel. In the case of the $Z \rightarrow \tau\tau$, a correction factor must be applied, which we will describe shortly. But first, we want to test the behaviour of our fit methodology.

6.7.2 Pseudo Experiments in the $e\mu$ Final State Channel

We test our fitting method with pseudo-experiments, in order to understand what we should expect from the fit, and to understand if the method has any pathologies not revealed by the fit to the data.

For performing pseudo-experiments, we use the expected number of events from each Standard Model contribution from Table 6.31. First we fluctuate the acceptances and luminosities accordingly to a Gaussian distribution. Then we fluctuate the new

number of events by a Poisson distribution with mean set to the expected originally estimated number of events. The resulting number of events is then used to randomly sample from the appropriate $\not\!\!E_T$-N_{jet} distribution. The entries are all added to create our pseudo-data, which is then fitted as if it was real data. We repeat this procedure 10000 times. For these pseudo-experiments, we let all 3 signal cross sections float in the fit simultaneously.

We show the results of the $e\mu$ pseudo-experiments in the Figures 6.16 to 6.18. In the figures, we give the cross sections, errors and pull distributions for each of the cross section parameters. The pull distributions are defined by:

$$pull = \frac{(\sigma_{fit} - \sigma_{input})}{\Delta\sigma_{(+/-)}} \tag{6.15}$$

where σ_{fit} is the cross section returned by the fit, σ_{input} is the Standard Model cross section used for building the pseudo experiments, and $\Delta\sigma_{(+/-)}$ is the positive or negative error (used depending on the sign of the numerator) returned by the fit error analysis. The pull distribution is expected to be a Gaussian centered at the origin with unit width. We fit the pull distributions with a Gaussian to test this expectation in each of the pull figures.

In Figure 6.19 we also see the distribution of the $e\mu$ maximum likelihood values from pseudo experiments overlaid with the value of the maximum likelihood from the actual data fit. The good agreement suggests that our data has good consistency with the Standard Model.

We see from the pseudo-experiment figures that we have a very well behaved $e\mu$ fit. The returned cross sections distribution mean is consistent with the Standard Model inputs. It should be noted that we used for the $t\bar{t}$ cross section we inputed a value of 6.7 pb instead of the 6.1 pb value that corresponds to a top mass of 178 GeV. The error distributions are also well behaved, and the Gaussian fit to the pull

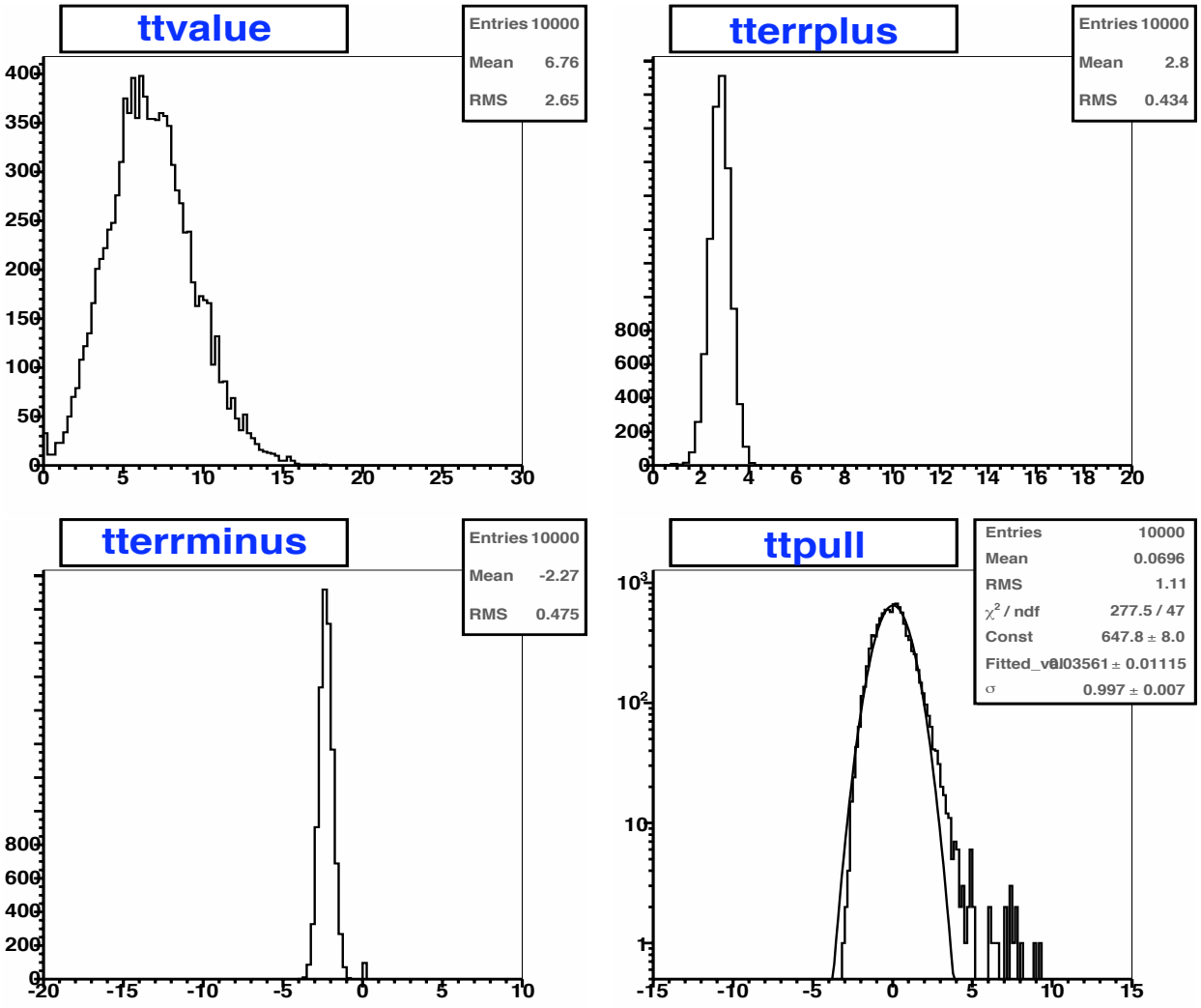

Figure 6.16: Fitted cross sections,the asymmetric errors and the pull distribution for $t\bar{t}$, from 10000 pseudo-experiments in the $e\mu$ channel, for 360 pb^{-1}, assuming totally correlated errors.

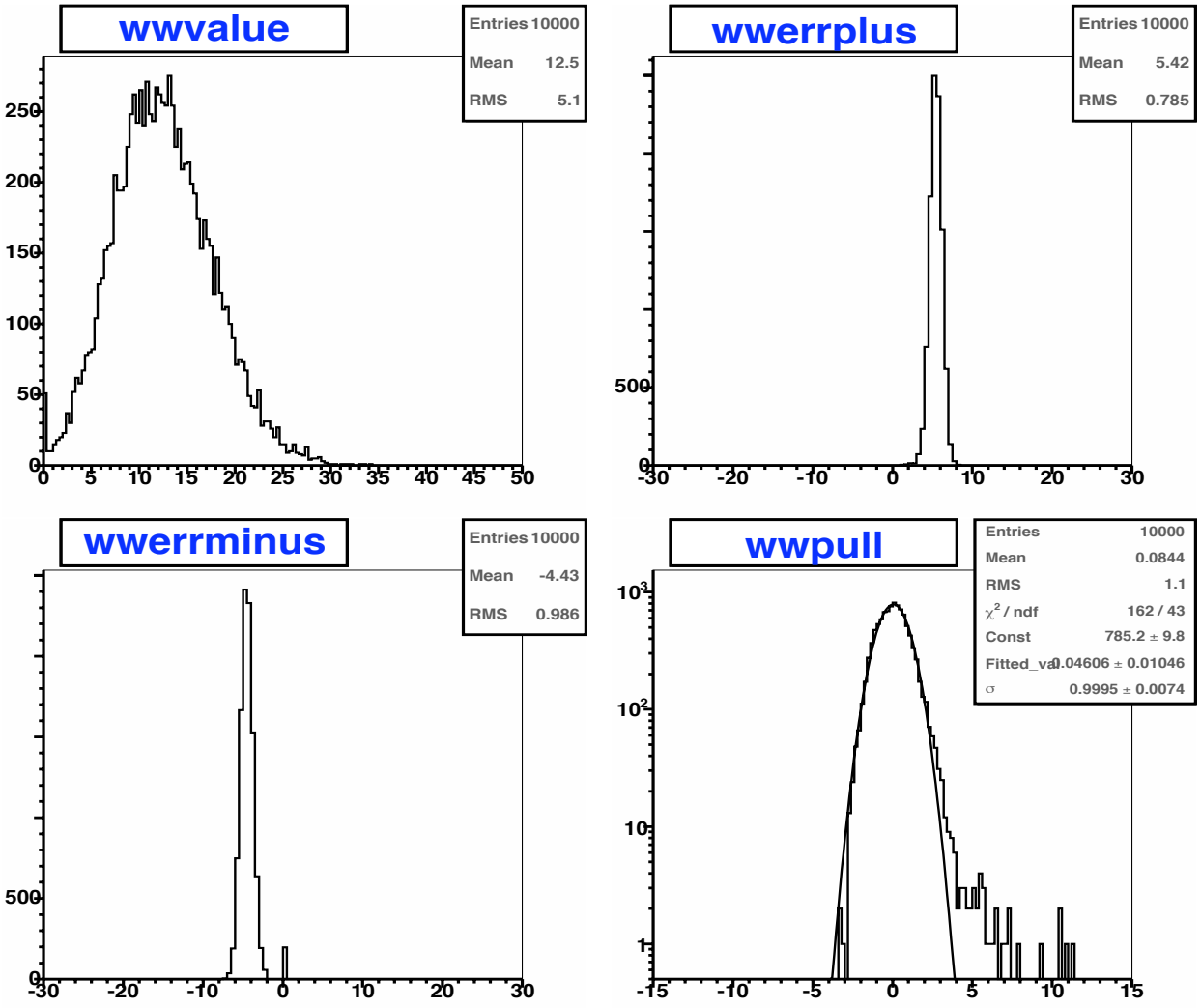

Figure 6.17: Fitted cross sections,the asymmetric errors and the pull distribution for WW, from 10000 pseudo-experiments in the $e\mu$ channel, for 360 pb^{-1}, assuming totally correlated errors.

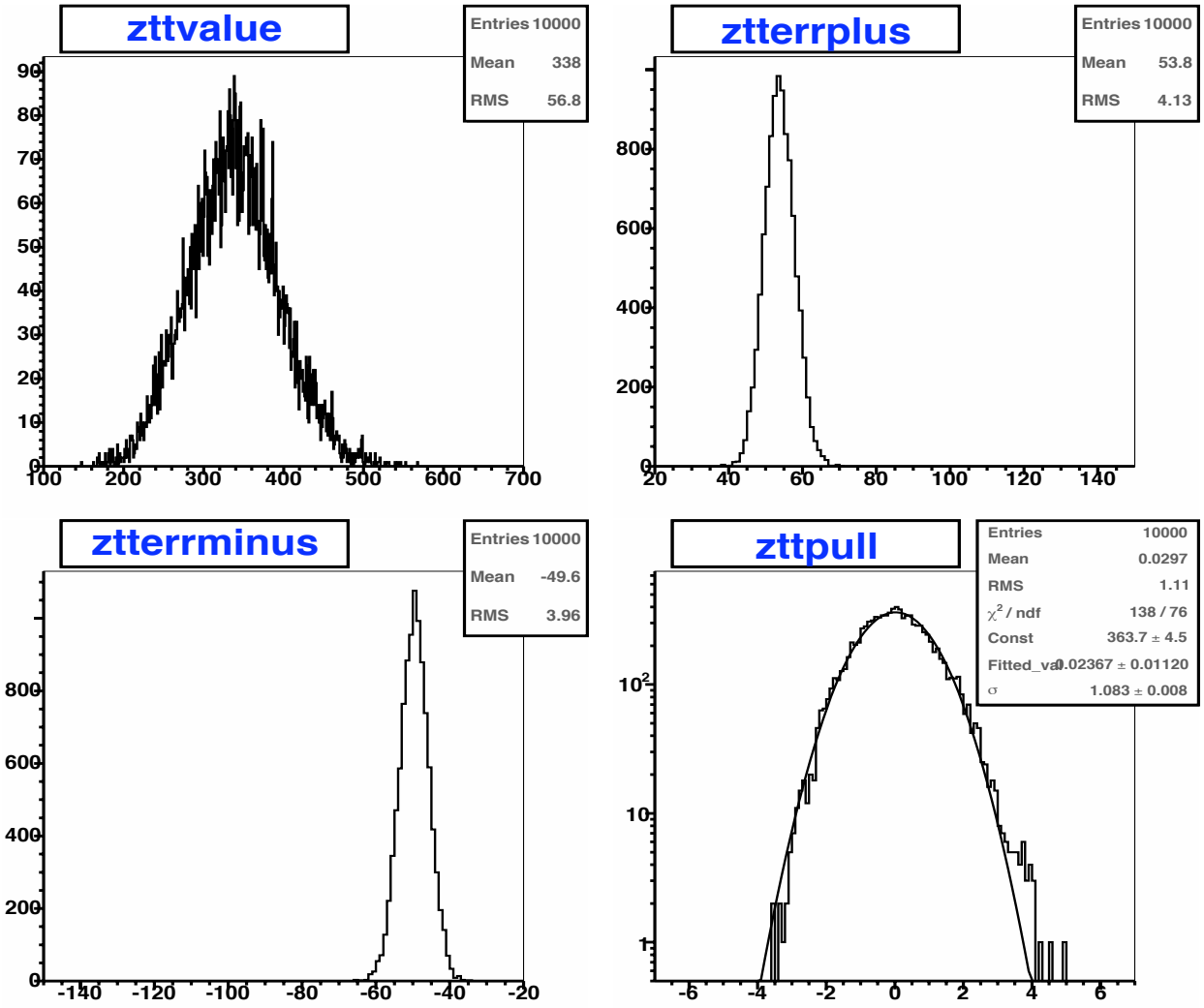

Figure 6.18: Fitted cross sections,the asymmetric errors and the pull distribution for $Z \rightarrow \tau\tau$, from 10000 pseudo-experiments in the $e\mu$ channel, for 360 pb^{-1}, assuming totally correlated errors.

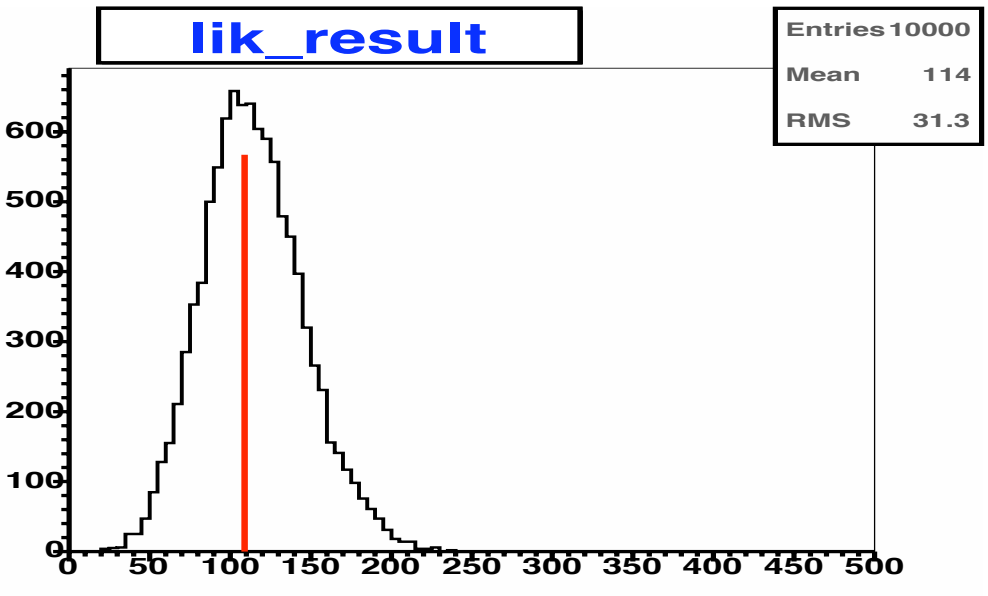

Figure 6.19: Likelihood values from 10000 pseudo-experiments in the $e\mu$ channel, for 360 pb^{-1}, assuming totally correlated errors. The red line shows the likelihood value for the data fit.

distribution in the totally correlated pseudo experiments returns a Gaussian with width close to unity. The fit parameters are given in Table 6.33;

Process	Pull Gaussian mean	Pull Gaussian width
$t\bar{t}$	0.035±0.011	0.997±0.007
WW	0.046±0.010	0.999±0.007
$Z \rightarrow \tau\tau$	0.024±0.011	1.083±0.08

Table 6.33: Gaussian parameters of fit to pull distributions in the $e\mu$ pseudo experiments

6.7.3 Extracting the $Z \rightarrow \tau\tau$ Cross Section from the $e\mu$ Data Fit

We want to measure the $p\bar{p} \rightarrow Z \rightarrow \tau^+\tau^-$ cross section, where the τ's decay leptonically, one to an electron, the other to a muon, and neutrinos[2]. For consistency with the $p\bar{p} \rightarrow Z^0$ measurements, performed in Run II in electron, muon or di-tau

[2]Remember that we measure the $Z/\gamma^* \rightarrow \tau^+\tau^-$ cross section only in eμ channel.

(e+hadronic tau) channel [69], we want to estimate the cross section for the true di-tau mass within the range 66 GeV/c^2 < $M_{\tau\tau}$<116 GeV/c^2. Therefore, we define the acceptance, α, as the number of $Z/\gamma^* \rightarrow \tau\tau$ events generated in the Monte Carlo mass window 66 GeV/c^2 < $M_{\tau\tau}$ < 116 GeV/c^2, which pass our eμ channel selection criteria, as described in section 5.2.

$$\alpha = \frac{N^{in}_{pass_selection}}{N^{in}_{generated}} \tag{6.16}$$

where both numerator and denominator are restricted to events within the mass window. Figure 6.20 shows the $M_{\tau\tau}$, after all the selection requirements.

We use the ztop4i, ztop5i and ztop1i Monte Carlo samples, each one being not enough for our needs: ztop1i has a very limited number of events passing our selection criteria, and ztop4i and ztop5i have a filter applied to select events with two leptons with $p_T > 17$ GeV, with an efficiency of 0.1367. We will refer to the combined ztop4i and ztop5i samples as the ztop45i sample.

The acceptance α calculated from the ztop45i samples (and its filter efficiency) is $(1.21 \pm 0.01)\%$.

We fit to the total number of events, N_{tot}, coming from $Z/\gamma^* \rightarrow \tau\tau$ and treat the contribution of events from outside the mass window as a correction factor, f^α.

$$f^\alpha = \frac{N^{all}_{pass/selection}}{N^{in}_{pass/selection}} \tag{6.17}$$

We find from the ztop45i samples that $N^{in}_{pass/selection} = 8223$, and $N^{all}_{pass/selection} = 8757$, giving;

$$f^\alpha = 1.065 \pm 0.021$$

The cross section expression becomes:

$$\sigma_{in} = \frac{N_{tot}}{f^{\alpha}} \frac{1}{2 \cdot BR(\tau \to e) BR(\tau \to \mu)} \frac{1}{\alpha \epsilon_{sf,trig} \mathcal{L}} \tag{6.18}$$

where the scale factors and trigger efficiencies (all included in $\epsilon_{sf,trig}$) are taken from Tables 6.2, 6.3 and 6.4. The branching ratios are from reference [16]:

$$BR(\tau \to e\bar{\nu}\nu) = (17.83 \pm 0.08)\%$$

$$BR(\tau \to \mu\bar{\nu}\nu) = (17.35 \pm 0.10)\%$$

Ideally we should subtract the contribution from $\gamma^* \to \tau\tau$ and the interference between γ^* and Z^0, to determine the $Z^0 \to \tau\tau$ cross section. Based on the calculation in CDF-6681 [70], this contribution is about 0.3% of the total, when restricted to the Z^0 mass window, well within our estimated uncertainty on the cross section, thus we ignore such a substraction.

6.7.4 Extracting the $t\bar{t}$ and WW Cross Sections from the $ee + \mu\mu + e\mu$ Data Fit

Assuming no correlations between acceptances between different dilepton channels and samples, the $ee + \mu\mu + e\mu$ fit is a 14 parameter fit. The parameters are the following:

- $\mathcal{L}$ - Gaussian constrained;
- $\sigma_{t\bar{t}}$ - σ_{WW}, floating;
- $\sigma_{Z\to\tau\tau}$ - Gaussian constrained;
- $\epsilon_{t\bar{t}}(e\mu)$, $\epsilon_{WW}(e\mu)$, $\epsilon_{Z\to\tau\tau}(e\mu)$ - Gaussian constrained;

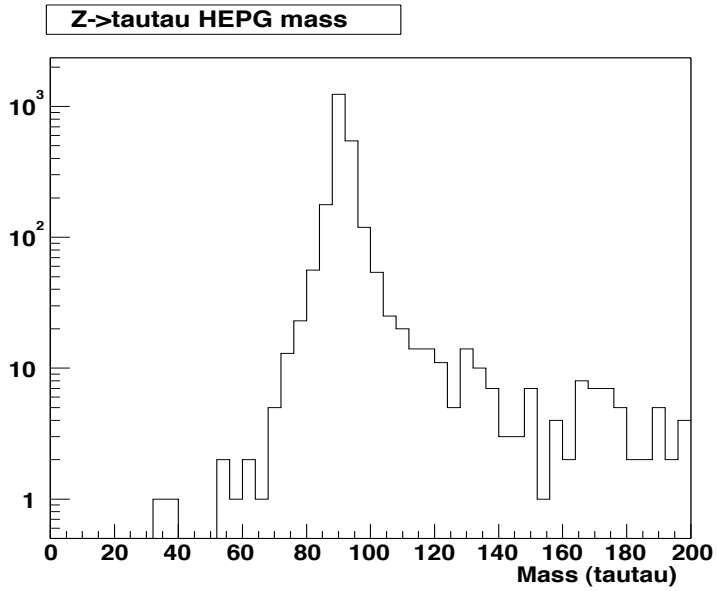

Figure 6.20: $M_{\tau\tau}$ invariant mass distribution, at the generator level, for events passing all the cuts, in eμ channel.

- $\epsilon_{t\bar{t}}(ee)$, $\epsilon_{WW}(ee)$ - Gaussian constrained;
- $\epsilon_{t\bar{t}}(\mu\mu)$, $\epsilon_{WW}(\mu\mu)$ - Gaussian constrained;
- $B_{e\mu}$, B_{ee}, $B_{\mu\mu}$ - Gaussian constrained;

where ϵ_{signal} is the expected acceptance, while $B_{<ch>}$ represents the background in the channel $< ch >$.

However given that there are many errors which are correlated between different signal samples (jet energy scale, ISR, lepton ID, etc), we have taken correlations into account. For simplicity we assumed 100% correlation between signal acceptances, within the same channel, and compared the outcome with uncorrelated fit. Thus we fold the correlations in as follows:

- $e\mu$ channel:

$$\mu_{ij}(e\mu) = k_{ij} * \sigma_{t\bar{t}} * \mathcal{L} * A(0)_{t\bar{t}}(e\mu) * (1 + f_{t\bar{t}}(e\mu) * \delta_1) + \tag{6.19}$$

$$k_{ij} * \sigma_{WW} * \mathcal{L} * A(0)_{WW}(e\mu) * (1 + f_{WW}(e\mu) * \delta_1) + \tag{6.20}$$

$$k_{ij} * \sigma_{Z\to\tau\tau} * \mathcal{L} * A(0)_{Z\to\tau\tau}(e\mu) * (1 + f_{Z\to\tau\tau}(e\mu) * \delta_1) \tag{6.21}$$

- ee channel:

$$\mu_{ij}(ee) = k_{ij} * \sigma_{t\bar{t}} * \mathcal{L} * A(0)_{t\bar{t}}(ee) * (1 + f_{t\bar{t}}(ee) * \delta_2) + \tag{6.22}$$

$$k_{ij} * \sigma_{WW} * \mathcal{L} * A(0)_{WW}(ee) * (1 + f_{WW}(ee) * \delta_2) \tag{6.23}$$

- $\mu\mu$ channel:

$$\mu_{ij}(\mu\mu) = k_{ij} * \sigma_{t\bar{t}} * \mathcal{L} * A(0)_{t\bar{t}}(\mu\mu) * (1 + f_{t\bar{t}}(\mu\mu) * \delta_3) + \tag{6.24}$$

$$k_{ij} * \sigma_{WW} * \mathcal{L} * A(0)_{WW}(\mu\mu) * (1 + f_{WW}(\mu\mu) * \delta_3) \tag{6.25}$$

where δ_1, δ_2 and δ_3 are Gaussians G(0,1).

We then use the fit to measure the $t\bar{t}$ and WW cross sections. It should be noted that in the full fit we do not try to measure the $Z \to \tau\tau$ cross section, as its measurement in our analysis is made only in the $e\mu$ channel.

6.7.5 Pseudo Experiments in the $ee + e\mu + \mu\mu$ Fit

In the same way as it is done in for the $e\mu$ fit, we test the behavior of our full fit with pseudo experiments. The results are shown in Figures 6.21-6.22. The pseudo experiments cross section distributions show a reasonable agreement with the input cross sections. It should be noted that the $t\bar{t}$ input cross sections used was 6.7 pb instead of the 6.1 pb expected for a top mass of 178 GeV. The pulls fit well to a Gaussian of mean 0 and width of about unity, with the Gaussian fit parameters to

the pulls of the totally correlated pseudo experiments given in Table 6.34. To check if the small high-tail present in the pull distributions goes away, we did pseudo-experiments with 10 times more integrated luminosity, far from any non-asymptotic regime. The upper tails in the pulls decreased, as expected.

Process	Gaussian mean	Gaussian width
$t\bar{t}$	0.031±0.010	0.956±0.007
WW	0.031±0.009	0.956±0.007

Table 6.34: Gaussian parameters of fit to pull distributions in the $ee + e\mu + \mu\mu$ pseudo experiments

In Figure 6.23 we can see the pseudo experiment maximum likelihood distribution against the maximum likelihood from the data fit. The good agreement suggests our data is consistent with Standard Model processes.

We also check if the expected errors improve as we increase the integrated luminosity. The Figures 6.24 and 6.25 show the pulls, fitted values and the errors for 3.6 fb^{-1}. We see the errors decrease as $1/\sqrt{10}$, as expected.

6.8 Shape Systematic Errors

We consider the sources of systematic errors that can alter the shape of our $\not\!\!E_T$-N. of jets templates. Among these, the major contribution come from uncertainties due to the jet energy scale and uncertainties in the initial and final state radiation. The errors are calculated using pseudo experiments, with an altered template being used for creating the pseudo-data and the unaltered templates used as the fit templates. We go into some detail about the $\not\!\!E_T$-N. of jets $e\mu$ shape systematic errors, and then we summarize the shape systematic errors in all channels.

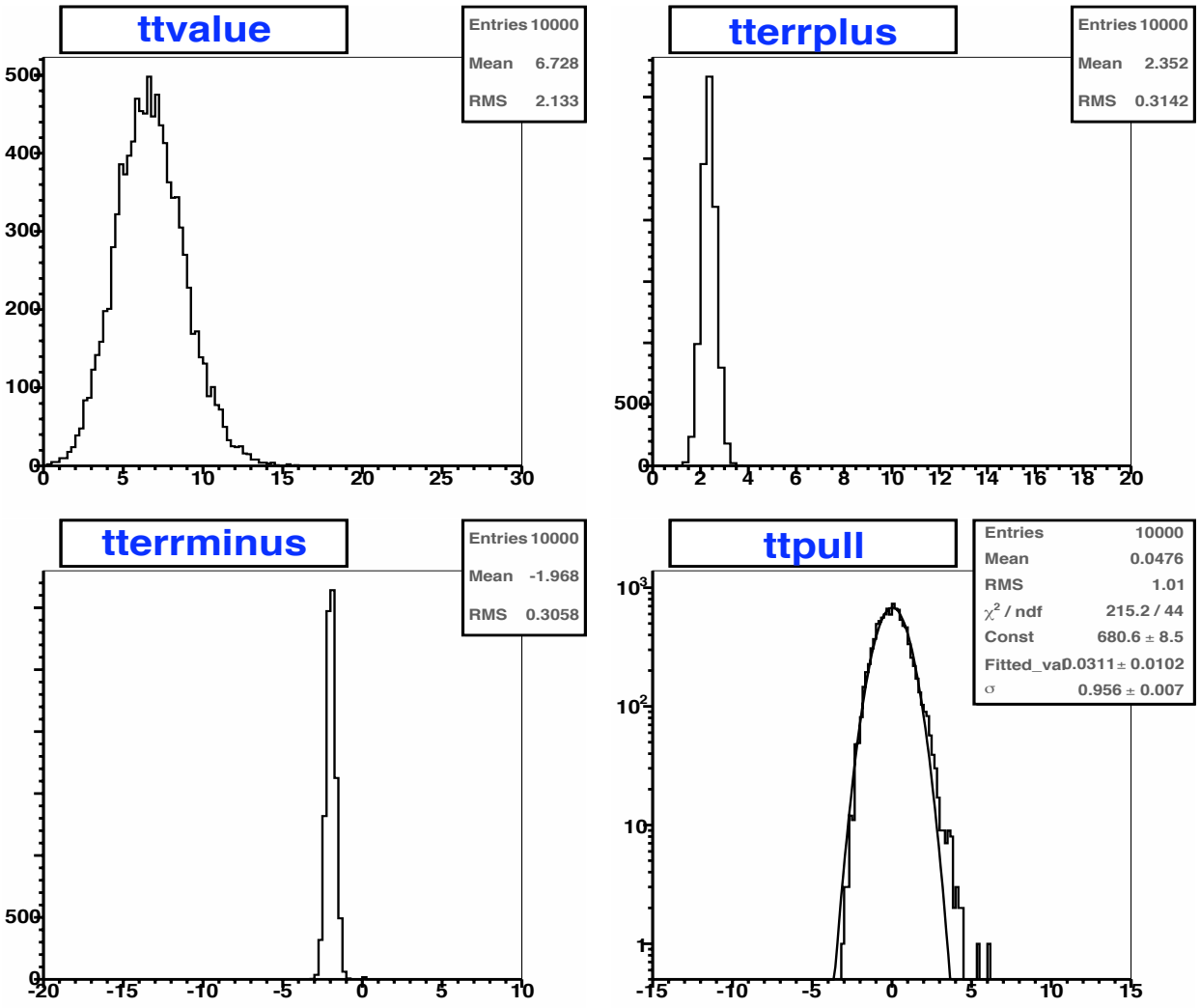

Figure 6.21: Fitted cross sections,the asymmetric errors and the pull distribution for $t\bar{t}$, from 10000 pseudo-experiments with the full fit, for 360 pb^{-1}, assuming totally correlated errors.

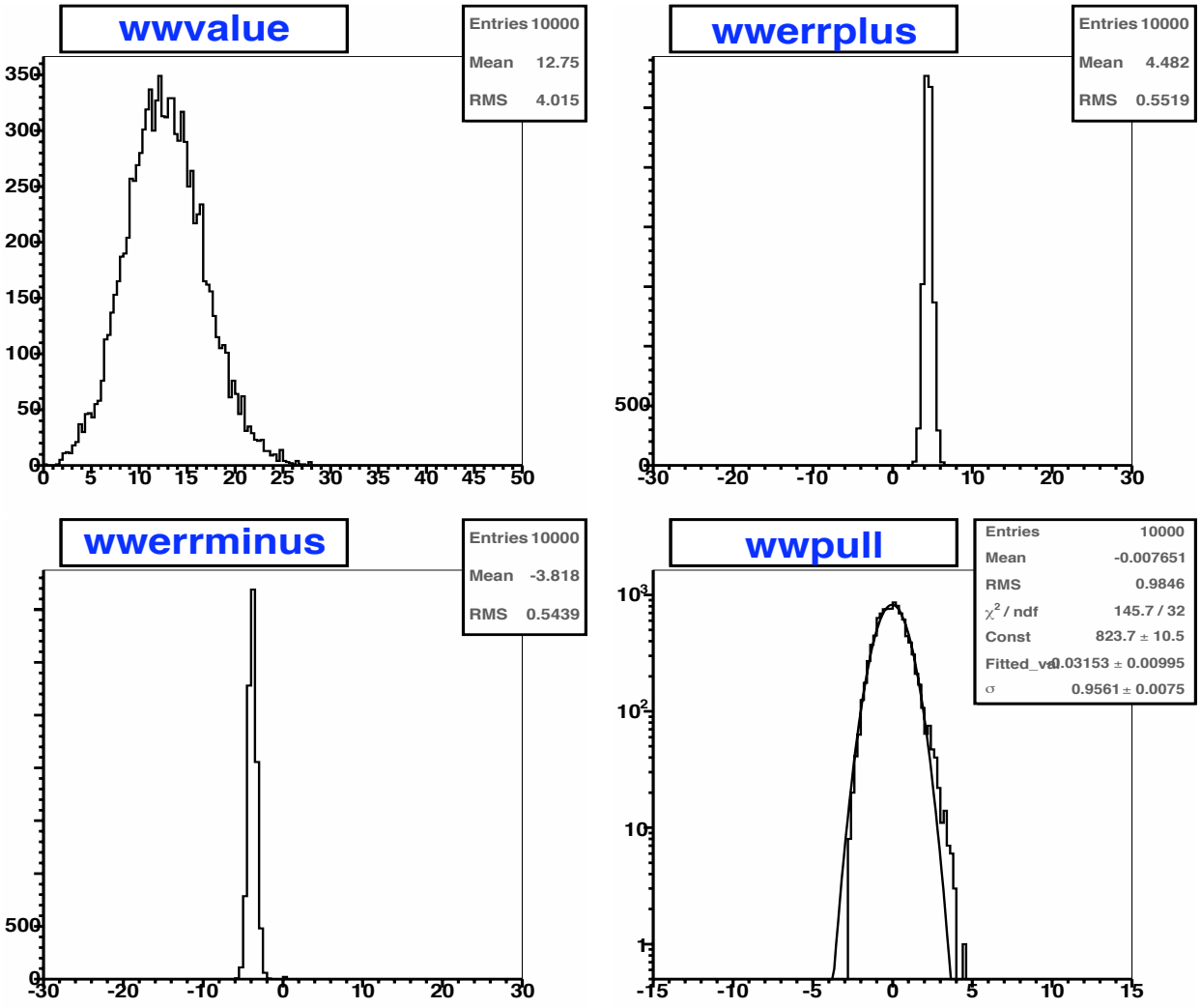

Figure 6.22: Fitted cross sections,the asymmetric errors and the pull distribution for WW, from 10000 pseudo-experiments with the full fit, for 360 pb^{-1}, assuming totally correlated errors.

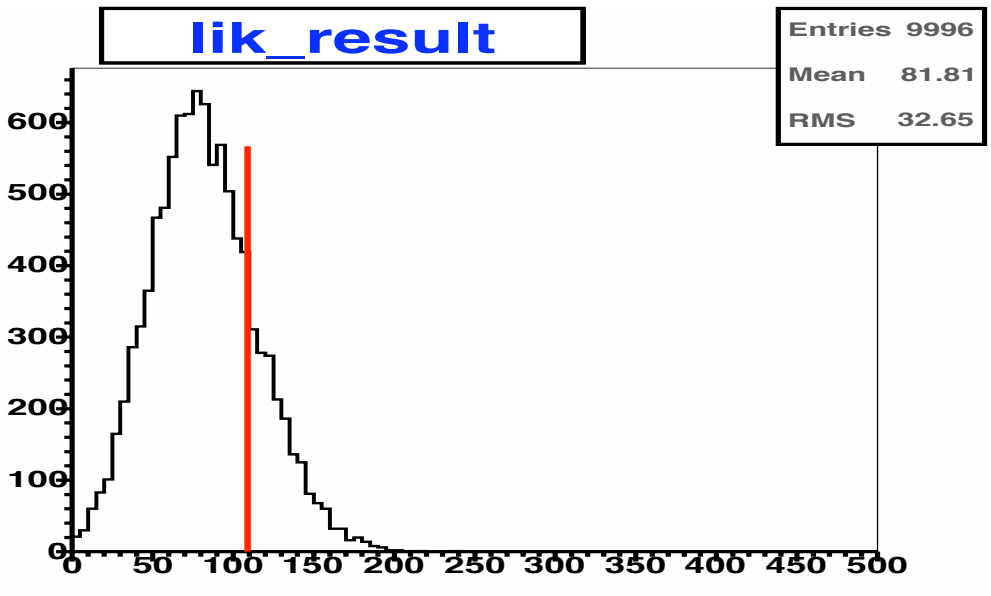

Figure 6.23: Likelihood values from 10000 pseudo-experiments with the full fit, for 360 pb^{-1}, assuming totally correlated errors. The red line shows the likelihood value for the data fit.

6.8.1 The $e\mu$ Fit Shape Systematics

For the jet energy scale systematic error estimation, we used the same tools as we did for estimating the acceptance systematic error from this source. We use the maximal variation of the systematic errors associated with each level of the jet energy corrections. These affect the shape of our number of jet distributions as well as the $\not\!\!E_T$ corrections, thus our templates are altered. We considered one standard deviation up and down for each of the systematic sources. We performed five 10000 iteration pseudo experiments with different random seeds to evaluate both the difference and the error on the difference between the mean of the fitted cross sections.

In Table 6.35 we have summarized the differences observed in pseudo-experiments of the fitted cross section and the error assigned to the $e\mu$ fit for this source of systematic error. For finding the average unaltered fitted cross sections we also use five different 10000 iteration pseudo-experiments.

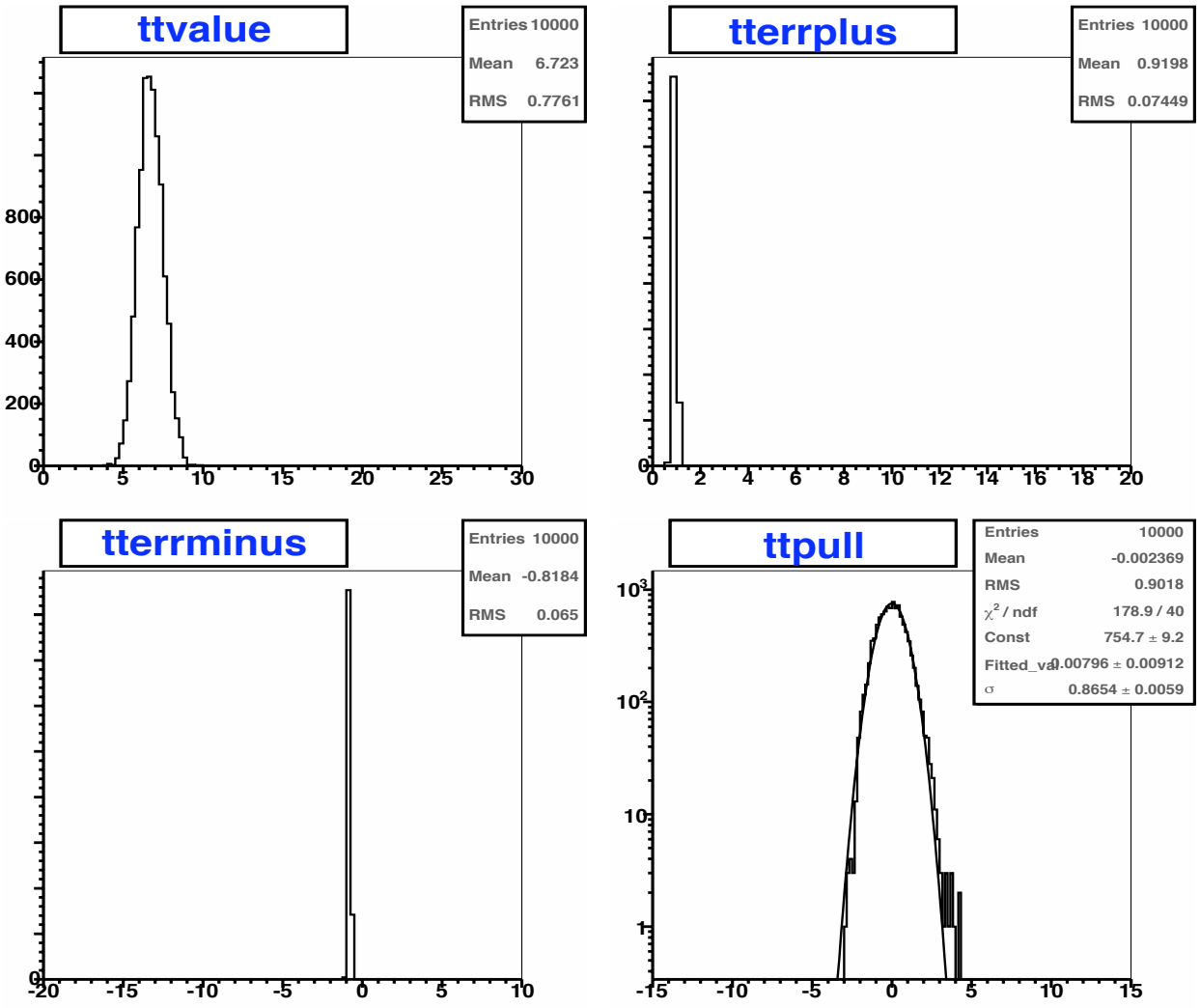

Figure 6.24: Fitted cross sections,the asymmetric errors and the pull distribution for $t\bar{t}$, from 10000 pseudo-experiments with the full fit, for $3600 pb^{-1}$, assuming totally correlated errors.

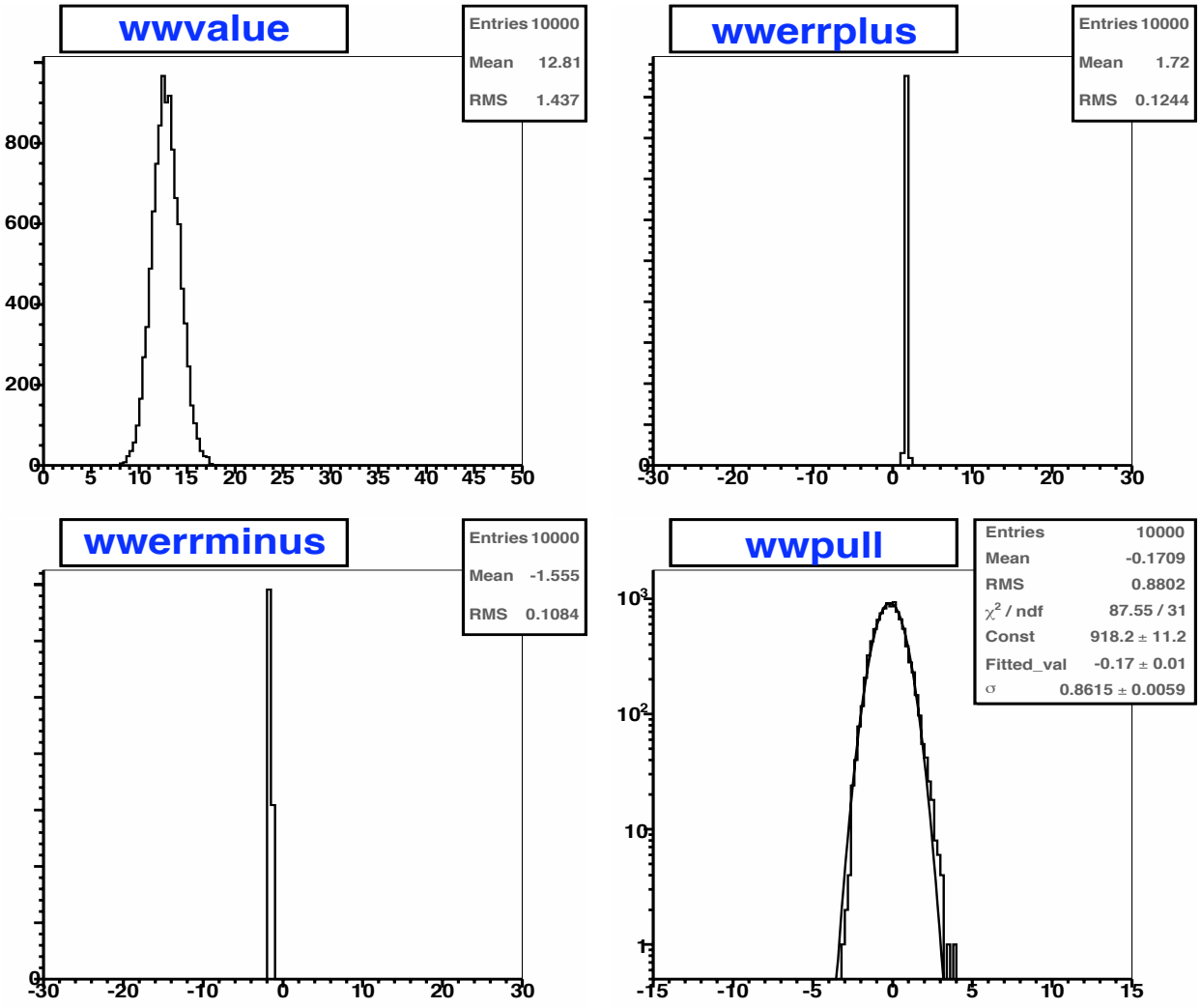

Figure 6.25: Fitted cross sections,the asymmetric errors and the pull distribution for WW, from 10000 pseudo-experiments with the full fit, for 3600 pb^{-1}, assuming totally correlated errors.

Batch	$t\bar{t}$ $+1\sigma$ (pb)	$t\bar{t}$ -1σ (pb)
1	6.712	7.142
2	6.682	7.138
3	6.701	7.147
4	6.714	7.166
5	6.694	7.121
Average	6.701	7.143
Unaltered average	6.743	6.743
Error	-1%	$+6\%$

Table 6.35: The $t\bar{t}$ jet energy scale systematic error for the $e\mu$ fit

Batch	WW $+1\sigma$ (pb)	WW -1σ (pb)
1	12.3	13.07
2	12.43	13
3	12.52	13.04
4	12.32	13.07
5	12.47	13.03
Average	12.41	13.04
Unaltered average	12.48	12.48
Error	-1%	$+4\%$

Table 6.36: The WW jet energy scale systematic error for the $e\mu$ fit

Batch	$Z \rightarrow \tau\tau$ $+1\sigma$ (pb)	$Z \rightarrow \tau\tau$ -1σ (pb)
1	335.9	342.7
2	337	341.7
3	335.7	340.5
4	336	341.5
5	337.2	341.6
Average	336	342
Unaltered average	337	337
Error	$- < 1\%$	$+2\%$

Table 6.37: The $Z \rightarrow \tau\tau$ jet energy scale systematic error for the $e\mu$ fit. The correction factor for Z$\rightarrow \tau\tau$ has not been applied yet for this table

In order to visualize the variation on the cross sections from jet energy scales, we plot in Figure 6.26 one of the 10000 iterations group of pseudo experiments each with the up and down variation of the jet energy scale against each other.

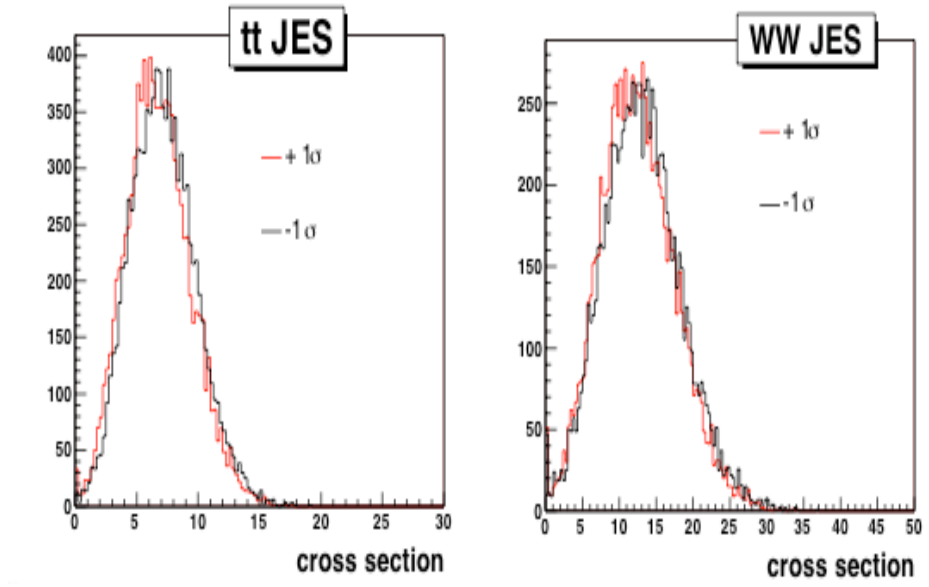

Figure 6.26: Example of variation due to jet energy scale on the $e\mu$ fit $t\bar{t}$ and WW cross sections

We estimate the initial state radiation shape systematic errors with the use of Pythia samples with more and less ISR than the expected amount. We used such samples for the $t\bar{t}$ and WW processes, and assumed that the $Z \rightarrow \tau\tau$ is affected by about the same order as the WW process. In Tables 6.38 and 6.39 we see the effect of these variations, using pseudo experiments in a similar way as was done for the jet energy scale shape systematic errors. We use five batches of 10000 iterations pseudo experiments to get an estimation of the statistical significance of the estimated differences.

In Figure 6.27 we show an example of the effect of more and less ISR than the expected amount, on the fitted $t\bar{t}$ and WW cross sections.

Batch	$t\bar{t}$ more ISR (pb)	$t\bar{t}$ less ISR (pb)
1	7.004	6.662
2	7.031	6.678
3	6.983	6.694
4	6.971	6.68
5	6.964	6.63
Average	6.991	6.608
Unaltered average	6.743	6.743
Error	+4%	−2%

Table 6.38: The $t\bar{t}$ ISR systematic error for the $e\mu$ fit

Batch	WW more ISR (pb)	WW less ISR (pb)
1	12.62	12.45
2	12.61	12.39
3	12.73	12.38
4	12.59	12.33
5	12.61	12.32
Average	12.63	12.37
Unaltered average	12.48	12.48
Error	+1%	−1%

Table 6.39: The WW FSR error for the $e\mu$ fit

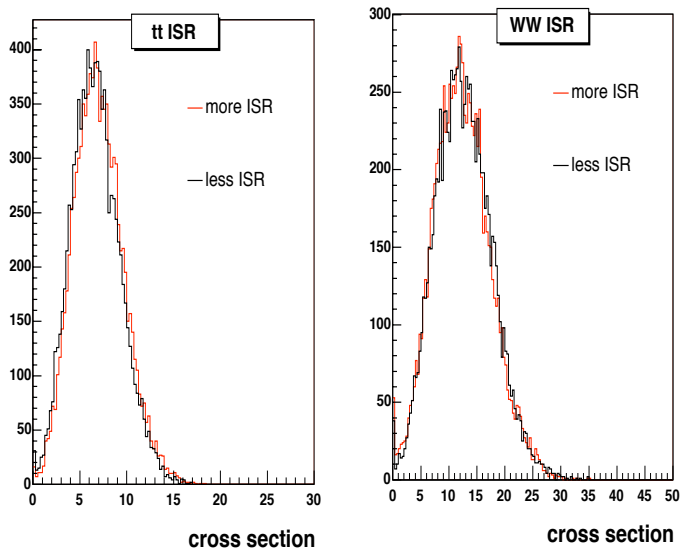

Figure 6.27: Example of variation due to ISR on $e\mu$ fit cross sections

Finally there is an error associated with the final state radiation. this is only important in the $t\bar{t}$ process. We calculate the $t\bar{t}$ FSR systematic errors using also Pythia samples with more FSR and less FSR than the expected amount. In Table 6.40 we see the results of our pseudo experiments and the variation in the fitted cross sections we observe. In Figure 6.28 we see an example of the effect of more and less FSR in the $t\bar{t}$ fitted cross section.

Batch	$t\bar{t}$ more FSR (pb)	$t\bar{t}$ less FSR (pb)
1	6.704	6.748
2	6.736	6.743
3	6.711	6.785
4	6.707	6.76
5	6.712	6.786
Average	6.714	6.764
Unaltered average	6.743	6.743
Error	-0.4%	$+0.3\%$

Table 6.40: The $t\bar{t}$ FSR systematic error for the $e\mu$ fit

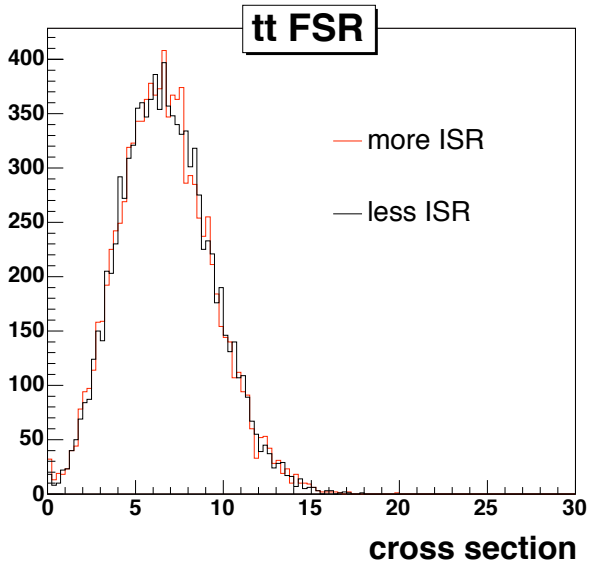

Figure 6.28: Example of variation due to FSR on $e\mu$ fit cross sections

6.8.2 Shape Systematic Errors Summary.

For the full fit shape systematic errors, we follow the same procedure as we did in the $e\mu$ channel only fit. We summarize the main sources of template shape systematic errors in Table 6.41, in both the $e\mu$ only and the full fits.

Source	$t\bar{t}$ $e\mu$	WW $e\mu$	$Z \to \tau\tau$ $e\mu$	$t\bar{t}$ (full)	WW (full)
JES	$-1+6\%$	$-1+4\%$	$-1+2\%$	$-2+7\%$	$-1+5\%$
ISR	$-2+4\%$	$\pm 1\%$	$\pm 1\%$	$-2+5\%$	$\pm 1\%$
FSR	$\pm 1\%$	—	—	—	—
Total	$-2+7\%$	$-1+4\%$	$-1+2\%$	$-3+8\%$	$-1+5\%$

Table 6.41: The shape systematic errors summary on the $e\mu$ and full fit.

Chapter 7

Cross Section Results

In this chapter we present the cross section measurements from our fit. These are for the $t\bar{t}$, WW and $Z \rightarrow \tau\tau$ production processes.

7.1 Fit Cross Section Results

In order to measure the signal processes cross sections we run both the $e\mu$ only fit and the $ee+e\mu+\mu\mu$ fit, with all of the cross section parameters allowed to float in the fit as well as with only one of the cross section parameters allowed to float at a time and the other constrained to the theoretical value. The highest statistical precision is obtained when allowing to float in the fit only one cross section at a time. In Table 7.1 we summarize all of the fit cross results. The first error (fit) in the values in the table, combines the statistical uncertainties, the acceptance systematic uncertainties and the luminosity systematic uncertainty. The second error (shape) in the values in the table is from the $\not\!\!E_T$-number of jets template shape systematic uncertainties. The results are consistent within errors to the Standard Model theoretical values, which are 6.1 pb, 12.4 pb and 250.4 pb for the $t\bar{t}$, WW and $Z \rightarrow \tau\tau$ processes respectively. All fits were performed with about 360 pb^{-1} of CDF-Run II data.

7.2 Data Fit Contour Plots

In order to visualize the relationships between the measurements of each of the cross sections, we plot the various two dimensional projections of the contour in the cross section values defined by the error in the measurements. These are obtained only when allowing all of the cross sections to float in the fit simultaneously. In Figure 7.1

Process	$e\mu$	$ee + \mu\mu + e\mu$
$\sigma(t\bar{t})$ (WW, $Z \to \tau\tau$ fixed)	$9.3^{+3.1}_{-2.6}(fit)^{+0.7}_{-0.2}(shape)$ pb	$8.4^{+2.5}_{-2.1}(fit)^{+0.7}_{-0.3}(shape)$ pb
$\sigma(t\bar{t})$ (all floating)	$9.3^{+3.1}_{-2.6}(fit)^{+0.7}_{-0.2}(shape)$ pb	$8.5^{+2.6}_{-2.2}(fit)^{+0.7}_{-0.3}(shape)$ pb
$\sigma(WW)$ ($t\bar{t}$, $Z \to \tau\tau$ fixed)	$12.3^{+5.3}_{-4.4}(fit)^{+0.5}_{-0.1}(shape)$ pb	$16.1^{+5.0}_{-4.3}(fit)^{0.8}_{-0.2}(shape)$ pb
$\sigma(WW)$ (all floating)	$11.4^{+5.2}_{-4.3}(fit)^{+0.5}_{-0.1}(shape)$pb	$16.3^{+5.1}_{-4.4}(fit)^{0.8}_{-0.2}(shape)$ pb
$\sigma(Z \to \tau\tau)$ ($t\bar{t}$, WW fixed)	$292.7^{+48.9}_{-45.1}(fit)^{+5.9}_{-2.9}(shape)$ pb	-
$\sigma(Z \to \tau\tau)$ (all floating)	$291.4^{+49.5}_{-46.0}(fit)^{+5.8}_{-2.9}(shape)$pb	-

Table 7.1: The final results for the Standard Model cross sections measured with 360 pb^{-1} are shown. By *fit* we mean the error returned by the fit, which includes the statistical, acceptance systematic and error on the luminosity; *shape* refers to the template distribution shape systematic uncertainty.

we give these contours for both $e\mu$ and the $ee + e\mu + \mu\mu$ fits. In the case of the $e\mu$ fit we have three two dimensional distributions: $\sigma_{t\bar{t}}$ vs. σ_{WW}, $\sigma_{t\bar{t}}$ vs. $\sigma_{Z\to\tau\tau}$ and σ_{WW} vs. $\sigma_{Z\to\tau\tau}$. In the case of the full fit we have only the $\sigma_{t\bar{t}}$ vs. σ_{WW} contour. We can see from the contours that each of our cross section measurements is not highly correlated with any of the others, as might be expected from the fact that the signal contributions occupy very different regions of the $\not\!\!E_T$-N_{jet} phase space.

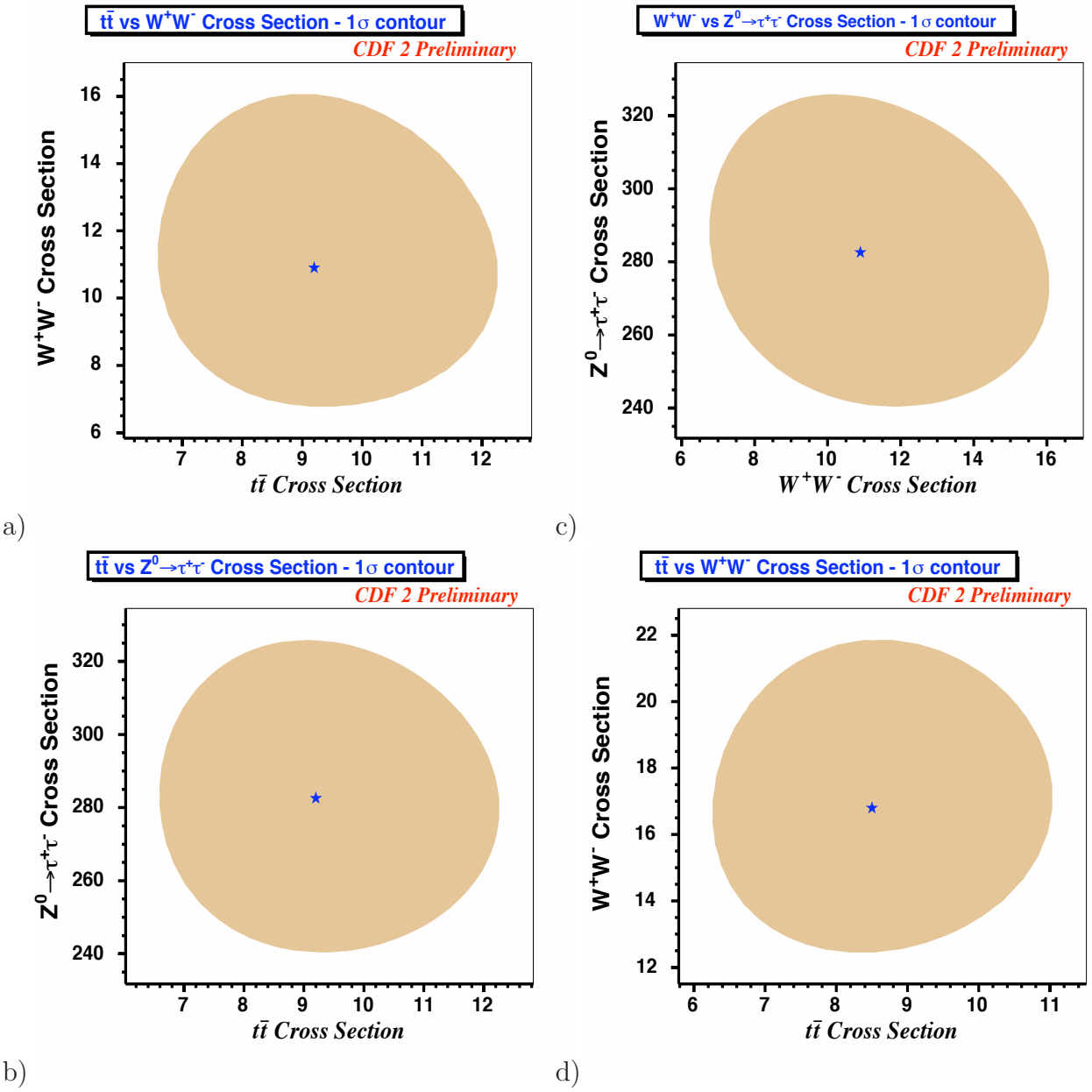

Figure 7.1: The two dimensional data 1σ cross section contours from the $e\mu$ fit (a, b and c), and from the $ee + e\mu + \mu\mu$ fit (d).

Chapter 8

Conclusions

We have developed a method to simultaneously extract the main SM cross sections from high-P_T dilepton events. The method considers the data in a more global fashion than the more traditional cross section measurements. The main Standard Model contributions occupy very different regions of the $\not\!\!E_T$-N_{jet} phase space, which allows for the simultaneous extraction of their cross sections. From a global fit of the dilepton sample to the expected Standard Model distributions, the most significant cross section measurements we obtain are with all the cross sections allowed to float in the fit simultaneously:

$$\sigma(t\bar{t}) = 8.5^{+2.6}_{-2.2}(fit)^{+0.7}_{-0.3}(shape) \text{ pb}$$

$$\sigma(WW) = 16.3^{-4.4}_{+5.1}(fit)^{0.8}_{-0.2}(shape) \text{ pb}$$

$$\sigma(Z \to \tau\tau) = 291.4^{+49.5}_{-46.0}(fit)^{+5.8}_{-2.9}(shape) \text{ pb}$$

where the first error combines statistical, acceptance systematic and luminosity uncertainties, and the second is due to systematic errors on the modeling of the shapes in the phase space we use for fitting.

In comparison the Standard Model cross section for the $t\bar{t}$ production process is 6.1 ± 0.3 pb (assuming a top mass of 178 GeV). The Standard Model cross section for the WW production is 12.4 ± 0.8 pb, and for the Drell-Yan $Z \to \tau\tau$ process in the Standard Model we have; $\sigma(p\bar{p} \to)BR(Z \to \tau\tau) = 250.4 \pm 5.0$ pb. We see that our results agree withing their uncertainties with the Standard Model expectations.

This method has allowed us to gain statistical significance in the $p\bar{p} \to t\bar{t}$ and $p\bar{p} \to WW$ cross sections over more traditional methods that apply kinematical cuts

to select the signal process, in addition to providing an independent measurement for these processes.

Our measurement of the $Z \rightarrow \tau\tau$ cross section uses $e\mu$ events only, and gives a measurement of comparable precision to a dedicated $Z \rightarrow \tau\tau$ analysis at CDF which identifies taus also through their hadronic decays.

Because this analysis makes minimal requirements on the data after selecting events with two high-P_T leptons, it can also provide a sensitive probe for new physics. Our measurements indicate good agreement with the SM, but we have not yet used it as a quantitative test of the Standard Model (for which we could quantify how likely our likelihood fit is). Next iterations of the analysis will also investigate explicit searches for new physics. The current results under collaboration review at CDF and will be submitted for publication in Physical Review Letters.

Appendix A

WW production anomalous coupling interaction Lagrangian

The most general effective Lagrangian describing the WWV coupling (V=γ or Z) is [71]:

$$\begin{aligned} L_{WWV}/g_{WWV} &= ig_1^V(W_{\mu\nu}^\dagger W^\mu V^\nu - W_\mu^\dagger V_\nu W^{\mu\nu}) \\ &+ i\kappa_V W_\mu^\dagger W_\nu V^{\mu\nu} \\ &+ \frac{i\lambda_V}{M_W^2} W_{\lambda\mu}^\dagger W_\nu^\mu V^{\nu\lambda} \\ &- g_4^V W_\mu^\dagger W_\nu(\partial^\mu V^\nu + \partial^\nu V^\mu) \\ &+ g_5^V \epsilon^{\mu\nu\rho\sigma}(W_\mu^\dagger \partial_\rho^{\Longleftrightarrow} W_\nu)V_\sigma \\ &+ i\bar{\kappa}_V W_\mu^\dagger W_\nu \bar{V}^{\mu\nu} \\ &+ \frac{ilam\bar{b}da_V}{M_W^2} W_{\lambda\mu}^\dagger W_\nu^\mu \bar{V}^{\nu\lambda} \end{aligned} \tag{A.1}$$

The $W^\pm$ is given by W^μ and V represents Z^0 or γ. Further we have that:

$$W_{\mu\nu} = \partial_\mu W_\nu - \partial_\nu W_\mu$$

$$V_{\mu\nu} = \partial_\mu V_\nu - \partial_\nu V_\mu$$

$$\bar{V}^{\mu\nu} = \frac{1}{2}\epsilon_{\mu\nu\rho\sigma} V^{\rho\sigma}$$

$$(A\partial_\mu^{\Longleftrightarrow} B) = A(\partial_\mu B) - (\partial_\mu A)B$$

$$g_{WWV} = -e\ cot(\theta_W) g_{WW\gamma} = -e \tag{A.2}$$

where θ_W is the weak mixing angle and e is the charge of the electron. Many of the coupling constants can be related to physical properties of the bosons, for example, g_1^γ is related to the charge of $W^\pm$ by $charge = cg_1^\gamma$. The constants κ_λ and λ_γ are related to the magnetic dipole moment (μ_W) of the W, $\mu_W = \frac{e}{2M_W}(1 + \kappa_\lambda + \lambda_\gamma)$, and the electric dipole moment (Q_W) by $Q_W = \frac{-e}{M_W}(\kappa_\gamma - \lambda_\gamma)$. The constants $\bar{\kappa}_\gamma$ and $\bar{\lambda}_\gamma$ are related to the electric dipole moment(d_W) by $d_W = \frac{e}{2M_W}(\bar{\kappa}_\gamma + \bar{\lambda}_\gamma)$ and the magnetic quadrupole $(\bar{Q}_W)$ by $\bar{Q}_W = \frac{-e}{M_W}(\kappa_g a\bar{m}ma - bar\lambda_\gamma)$

By setting the κ_γ, κ_Z, g_1^γ and g_1^Z to 1 and all others to zero the Standard Model interaction Lagrangian is recovered. Deviations from the Standard Model can be parametrized with the values of the coupling constants.

Appendix B

Kinematic Distributions of the CDF 2 Data - 360 pb^{-1}

In this appendix we show a number of kinematical variables plots, which help us understand the behaviour of our data when compared with the standard model. The list of the plots is below;

- Figure B.1: The number of jets for ee, $e\mu$ and $\mu\mu$ channels.
- Figure B.2: The missing energy for ee, $e\mu$ and $\mu\mu$ channels.
- Figure B.3: The missing energy for 0 jet events, for ee, $e\mu$ and $\mu\mu$ channels.
- Figure B.4: The missing energy for 1 jet events, for ee, $e\mu$ and $\mu\mu$ channels.
- Figure B.5: The missing energy for 2 jet events, for ee, $e\mu$ and $\mu\mu$ channels.
- Figure B.6: The invariant mass for ee, $e\mu$ and $\mu\mu$ channels.
- Figure B.7: The lepton transverse momentum for electrons and muons.
- Figure B.8: The leptons ϕ and η distributions, for electrons and muons.

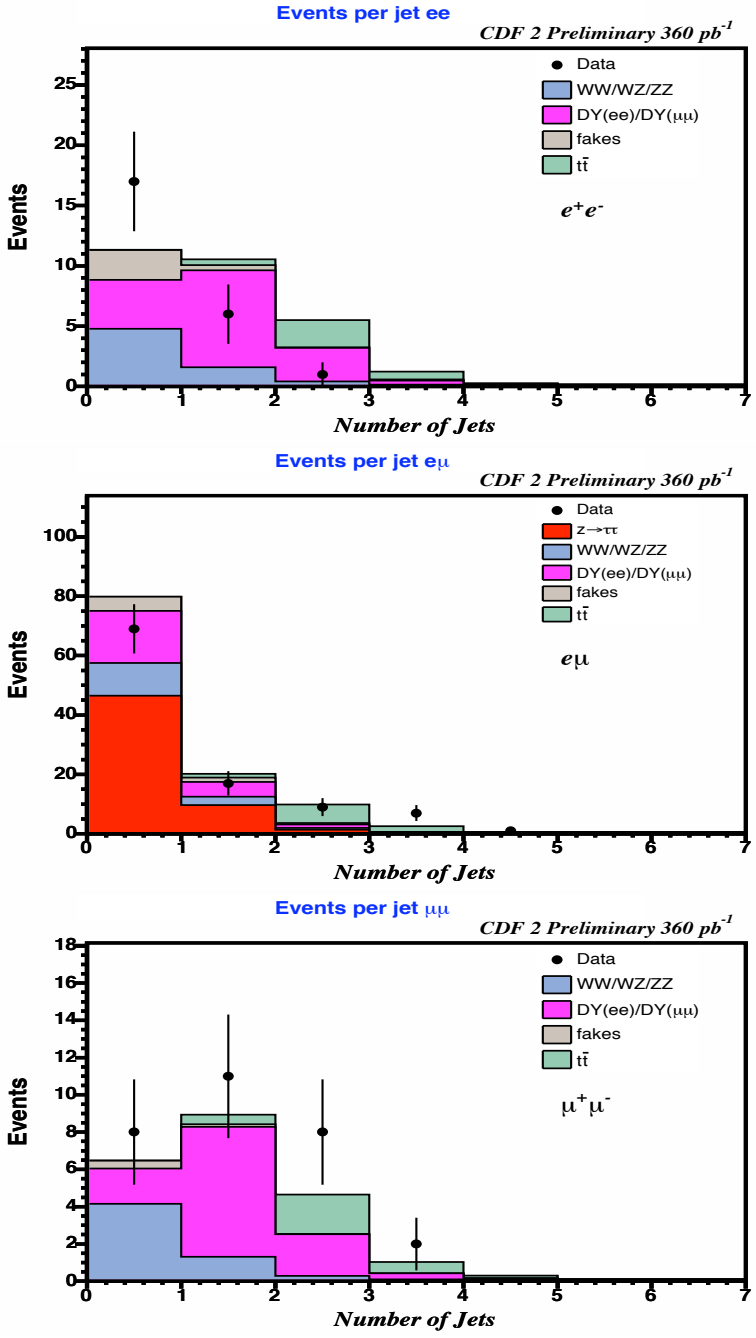

Figure B.1: The number of jets for ee, $e\mu$ and $\mu\mu$ channels.

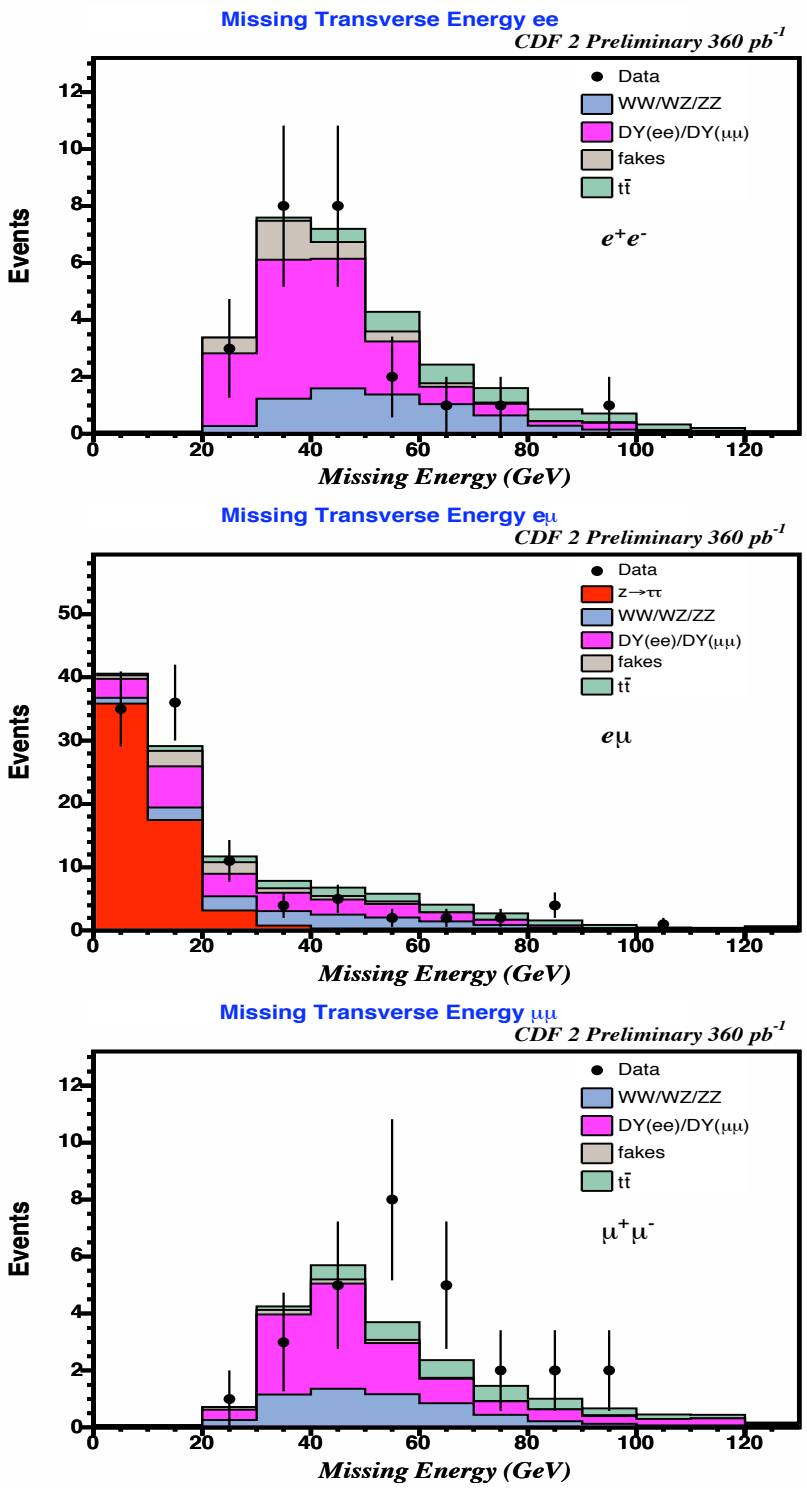

Figure B.2: The missing energy for ee, $e\mu$ and $\mu\mu$ channels.

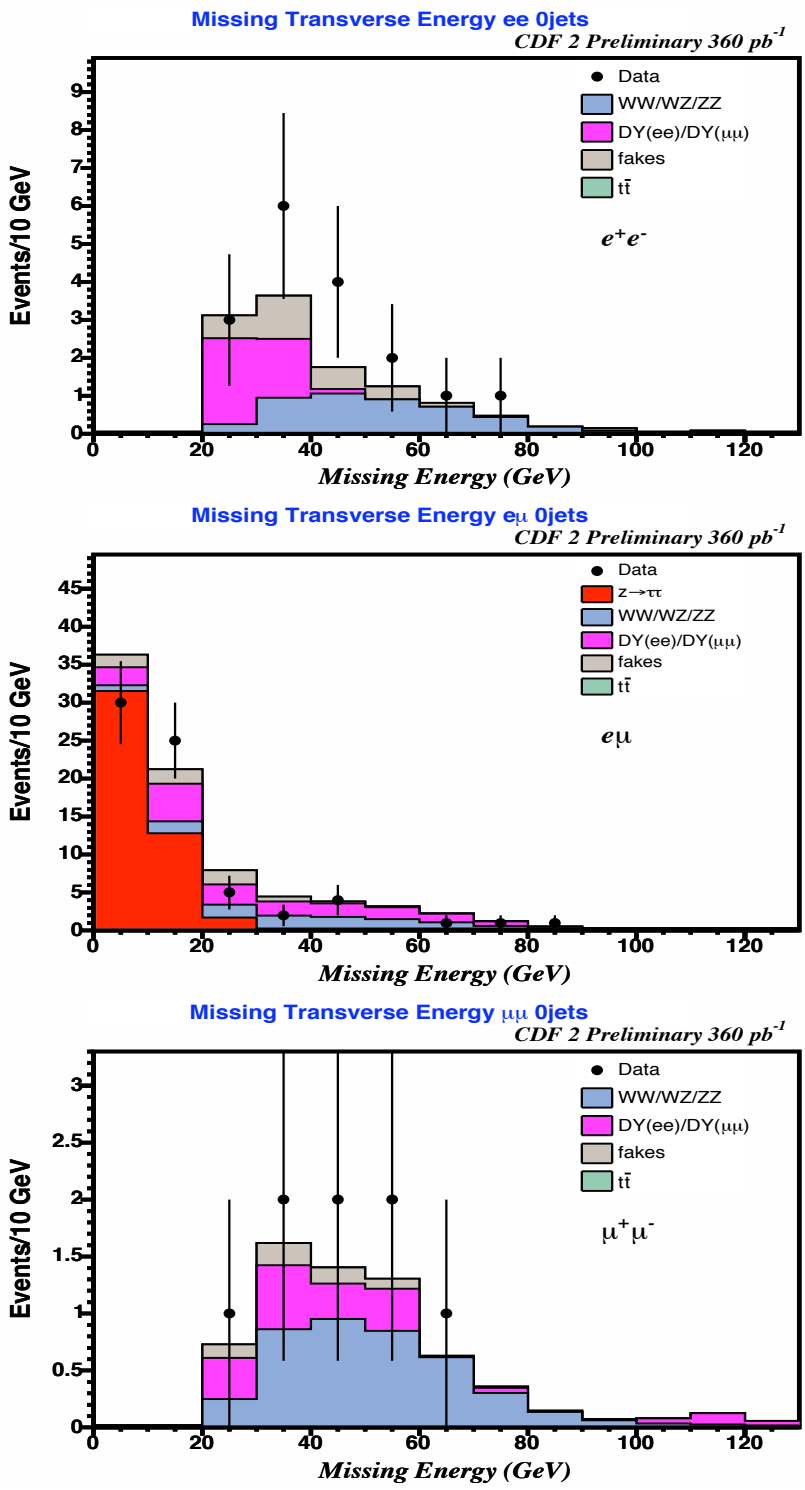

Figure B.3: The missing energy for 0 jet events, for ee, $e\mu$ and $\mu\mu$ channels.

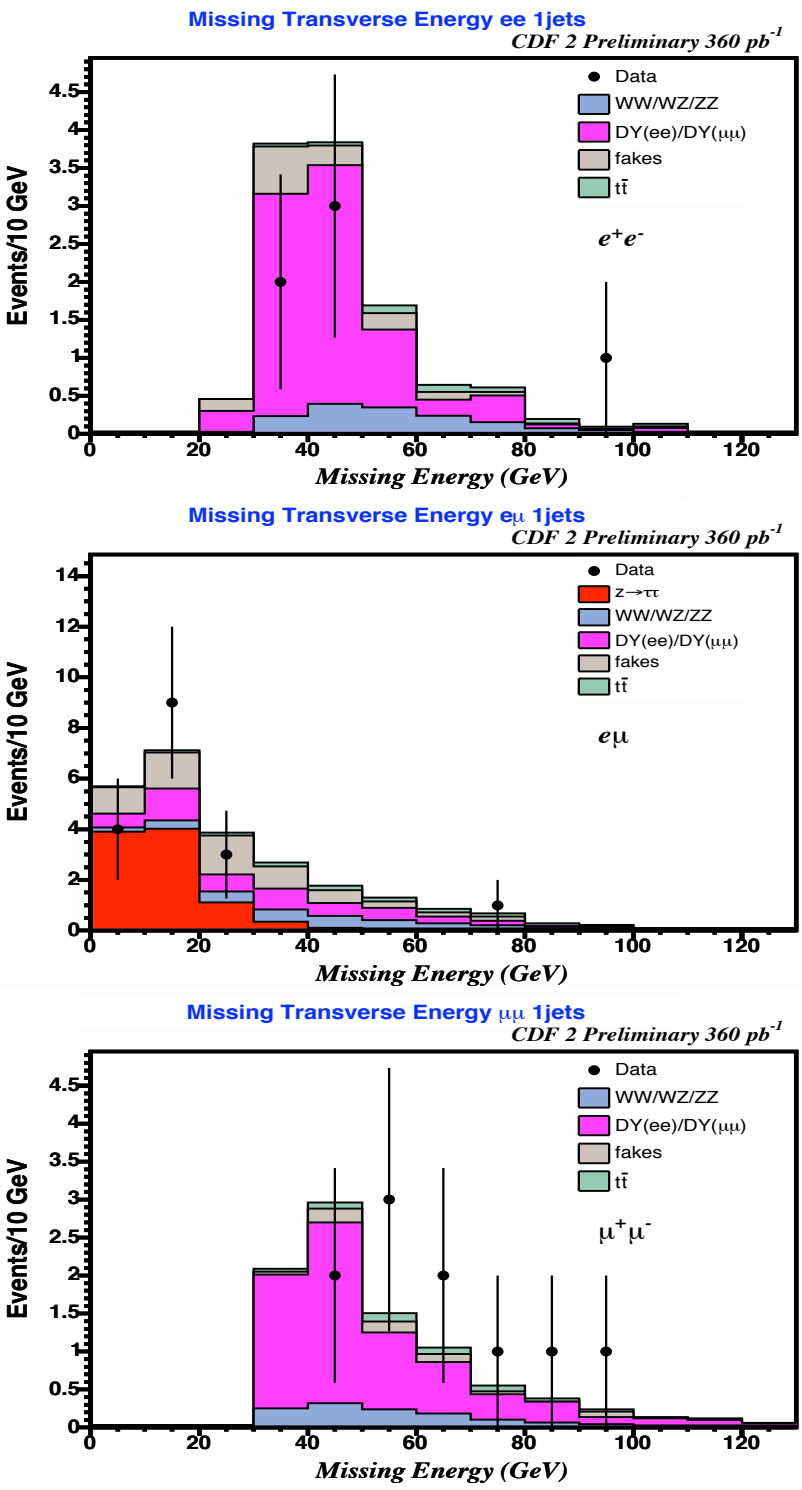

Figure B.4: The missing energy for 1 jet events, for ee, $e\mu$ and $\mu\mu$ channels.

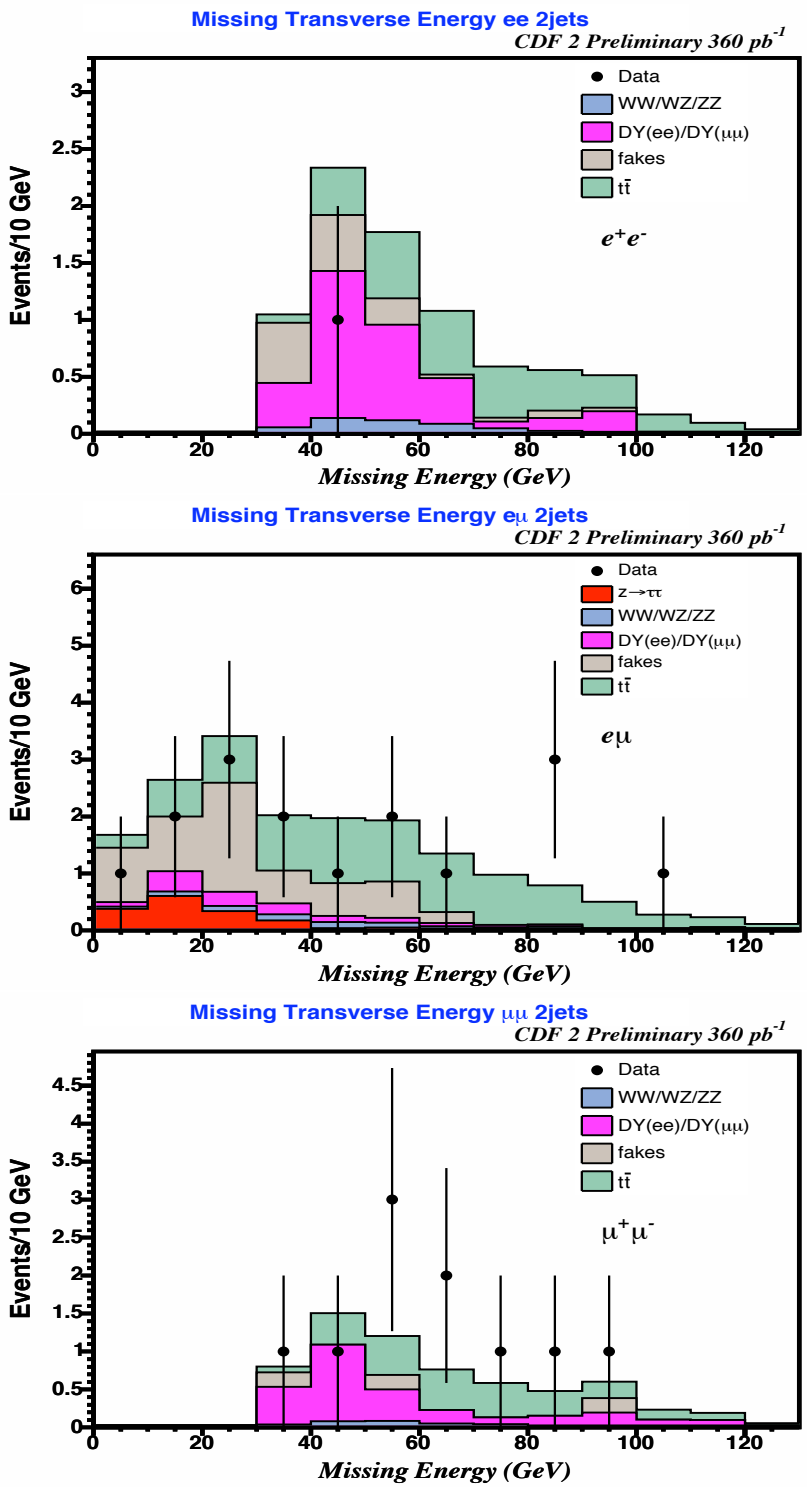

Figure B.5: The missing energy for 2 jet events, for ee, $e\mu$ and $\mu\mu$ channels.

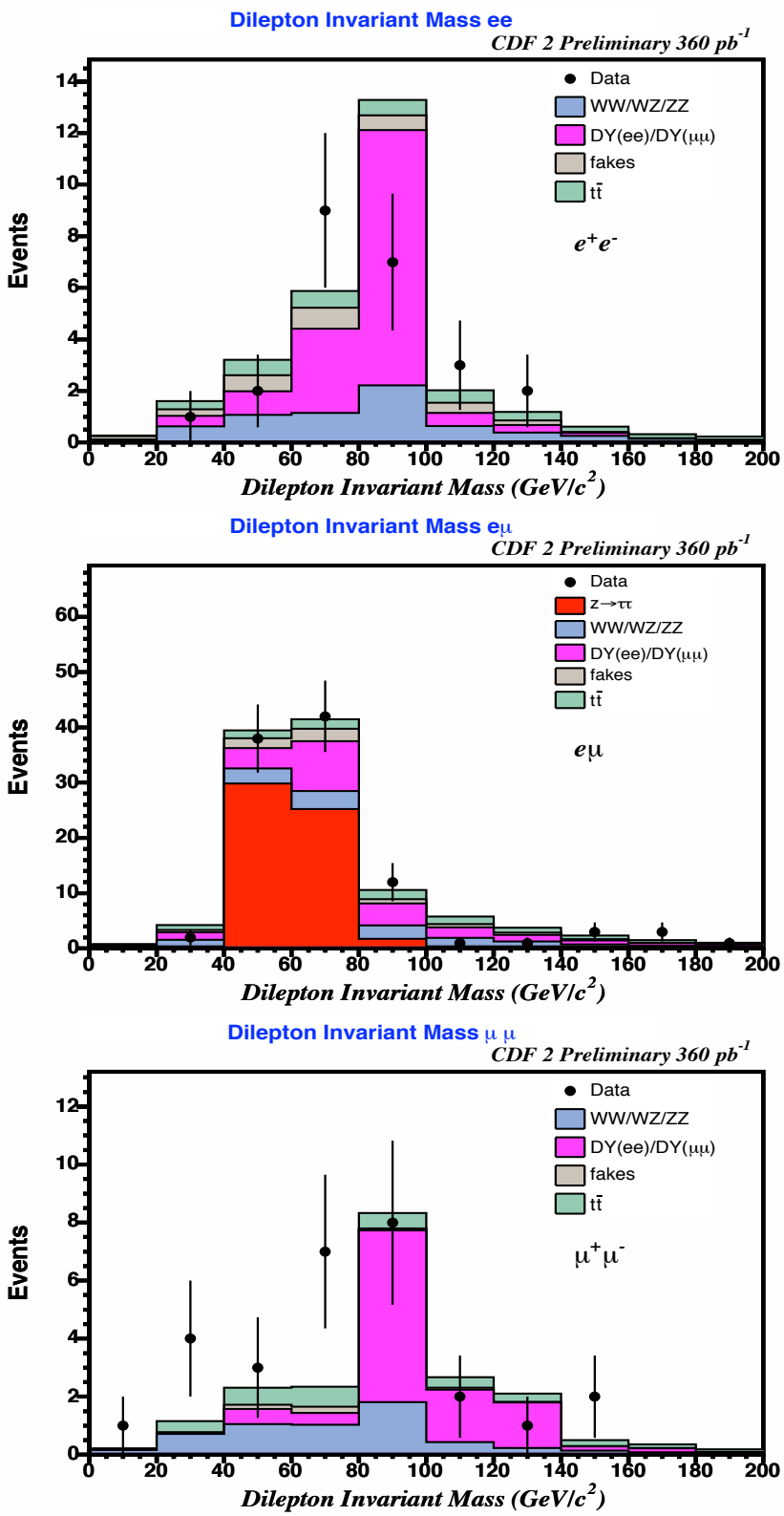

Figure B.6: The invariant mass for ee, $e\mu$ and $\mu\mu$ channels.

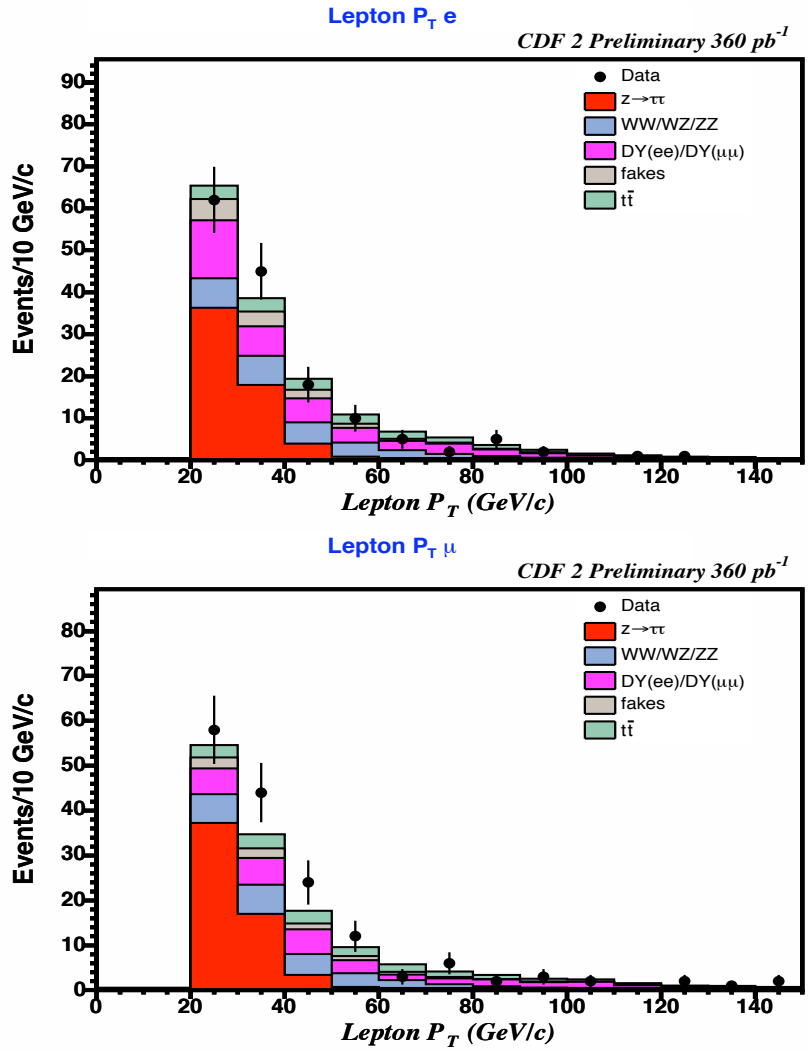

Figure B.7: The lepton transverse momentum for electrons and muons.

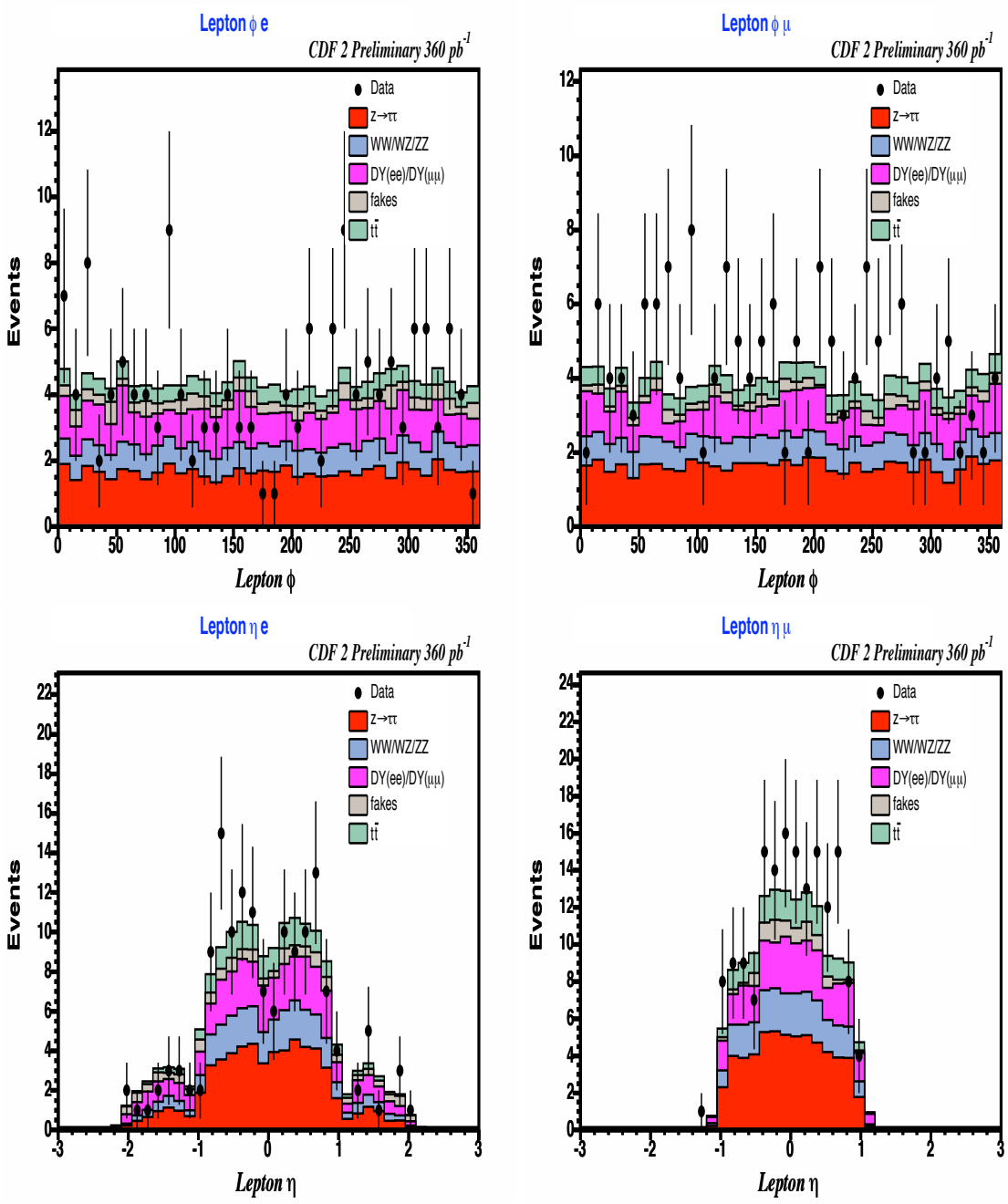

Figure B.8: The leptons ϕ and η distributions, for electrons and muons.

Appendix C

Missing Energy vs Number of Jets for CDF 2 Data - 360 pb^{-1}

In this appendix we show scatter plots of $\not\!\!E_T$ vs. Number of Jets distributions containing our signal processes and our data. These serve to better visualize the regions the different signal process lie on and the composition of the data that is fitted. the list of figures is given below;

- Figure C.1: 3 figures for the ee channel signal processes, data and total expected events.
- Figure C.2: 3 figures for the $e\mu$ channel signal processes, data and total expected events.
- Figure C.3: 3 figures for the $\mu\mu$ channel signal processes, data and total expected events.

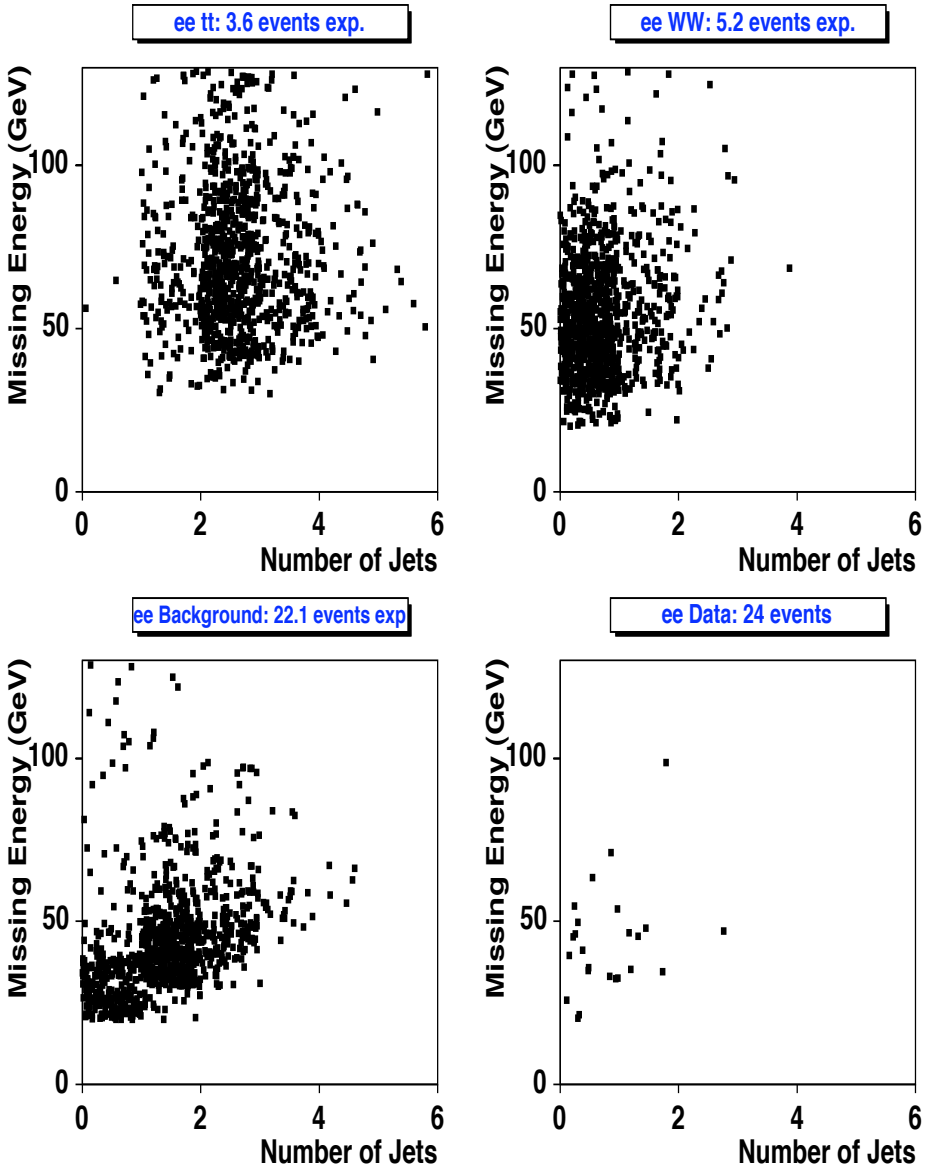

Figure C.1: The missing energy vs number of jets for *ee* channel.

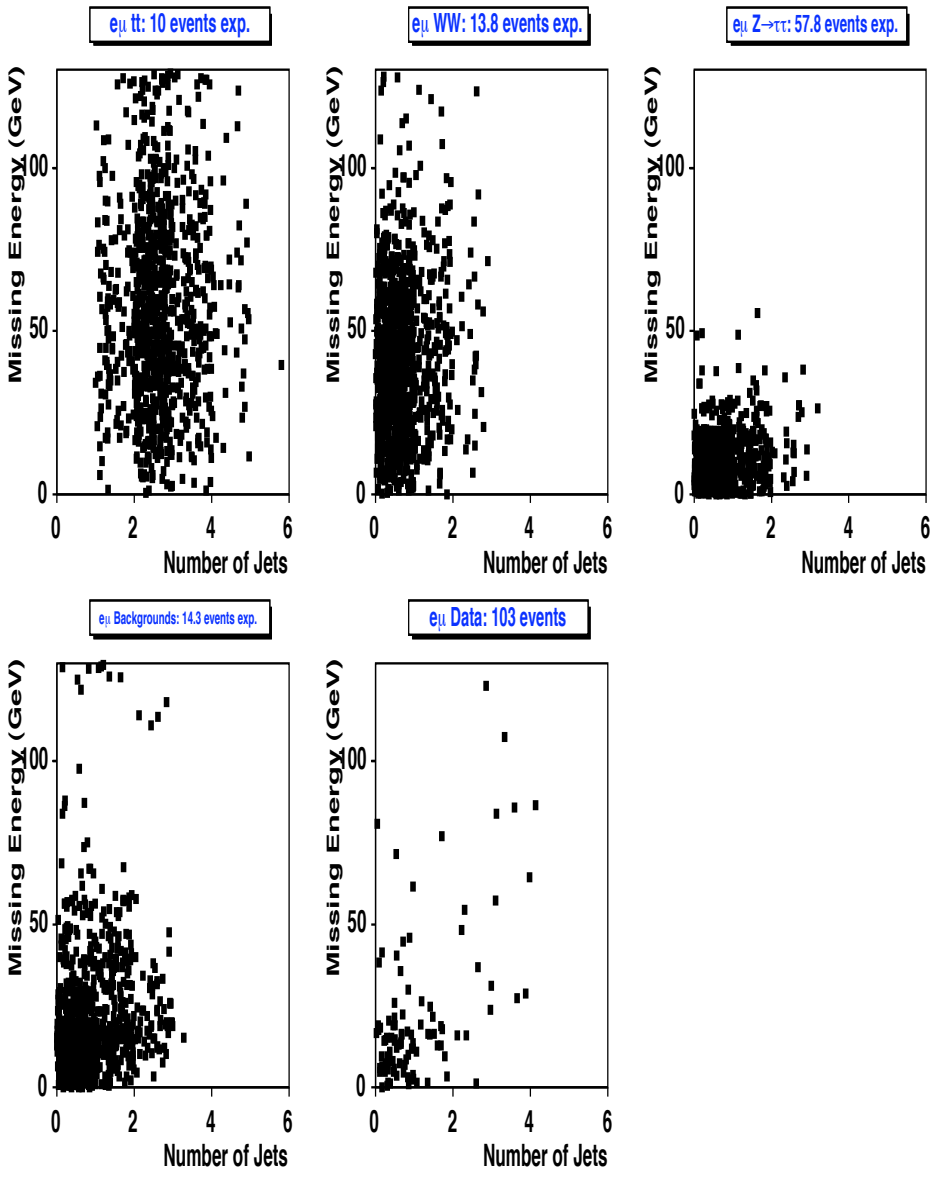

Figure C.2: The missing energy vs number of jets for $e\mu$ channel.

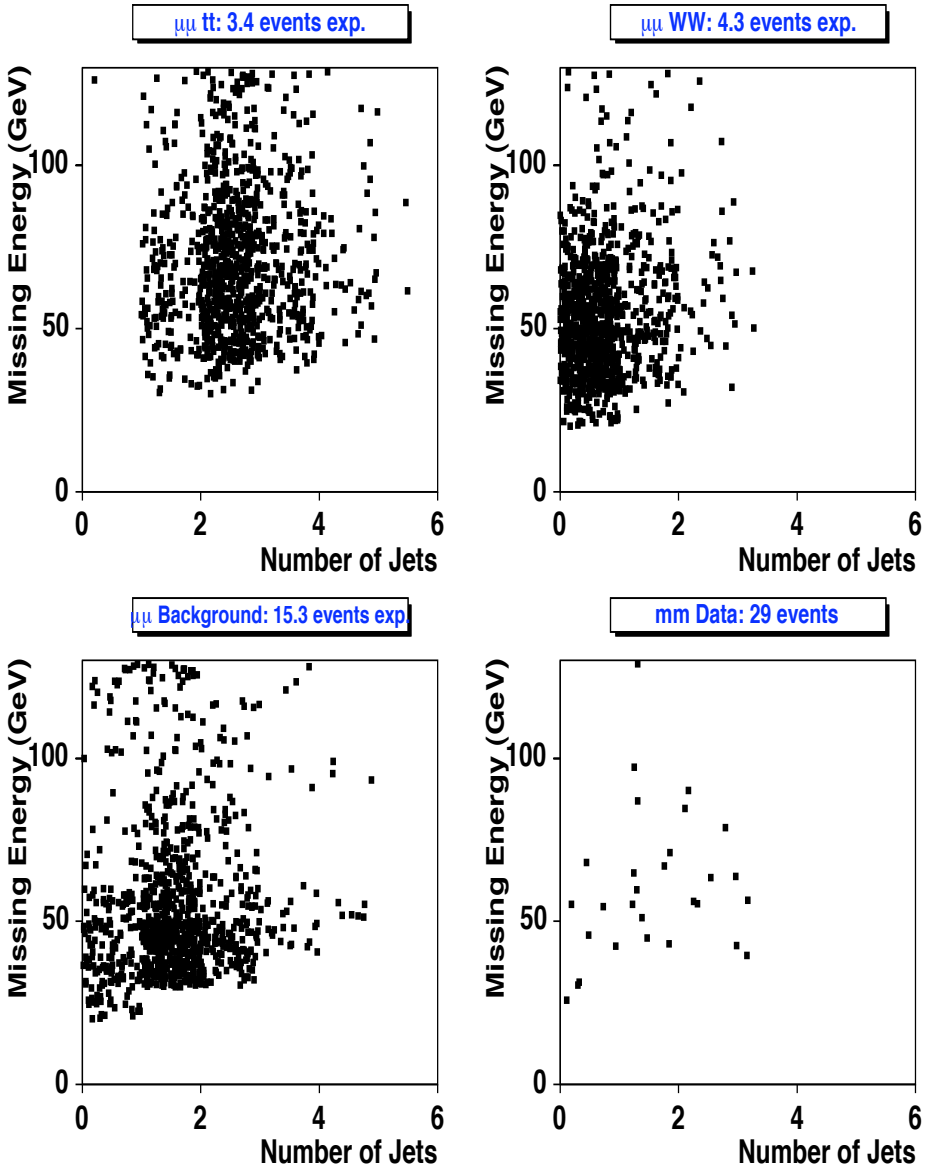

Figure C.3: The missing energy vs number of jets for $\mu\mu$ channel.

Appendix D

Detailed Acceptance Tables

In this appendix we show the detailed expected of events surviving after each cut for each of the physics process, by sub-category. This helps understand the subcategory composition differences in our signal and background physics processes.

Tables D.1, D.2 and D.3 show the signal expected number of events after our 2 opposite-sign high-P_T lepton requirement (plus $\not\!\!E_T^{sig}$ for ee and $\mu\mu$), from the Monte Carlo samples. The rest of the tables are for background processes.

Category	ID+ISO	Conv+Cosm	metsig	OS
TCE-TCE	4.63 ± 0.10	3.84 ± 0.09	2.60 ± 0.08	2.59 ± 0.08
TCE-PHX	1.87 ± 0.06	1.70 ± 0.06	1.15 ± 0.05	1.02 ± 0.05
ee	6.49 ± 0.01	5.54 ± 0.01	3.75 ± 0.01	3.61 ± 0.01
Category	ID+ISO	Conv+Cosm	metsig	OS
TCE-CMUP	4.67 ± 0.10	4.16 ± 0.10	4.16 ± 0.10	4.16 ± 0.10
TCE-CMU	0.98 ± 0.05	0.87 ± 0.04	0.87 ± 0.04	0.87 ± 0.04
TCE-CMP	1.37 ± 0.05	1.20 ± 0.05	1.20 ± 0.05	1.20 ± 0.05
TCE-CMX	1.61 ± 0.06	1.44 ± 0.06	1.44 ± 0.06	1.44 ± 0.06
TCE-CMIO	1.33 ± 0.05	1.20 ± 0.05	1.20 ± 0.05	1.19 ± 0.05
PHX-CMUP	0.93 ± 0.05	0.92 ± 0.04	0.92 ± 0.04	0.82 ± 0.04
PHX-CMX	0.35 ± 0.03	0.35 ± 0.03	0.35 ± 0.03	0.32 ± 0.03
$e\mu$	11.25 ± 0.01	10.14 ± 0.01	10.14 ± 0.01	10.00 ± 0.01
Category	ID+ISO	Connv+Cosm	metsig	OS
CMUP-CMUP	1.33 ± 0.05	1.27 ± 0.05	0.81 ± 0.04	0.80 ± 0.04
CMUP-CMU	0.52 ± 0.03	0.50 ± 0.03	0.34 ± 0.03	0.34 ± 0.03
CMUP-CMP	0.66 ± 0.04	0.63 ± 0.04	0.43 ± 0.03	0.43 ± 0.03
CMUP-CMX	0.85 ± 0.04	0.82 ± 0.04	0.57 ± 0.04	0.57 ± 0.04
CMUP-CMIO	0.98 ± 0.05	0.95 ± 0.05	0.66 ± 0.04	0.66 ± 0.04
CMX-CMX	0.15 ± 0.02	0.14 ± 0.02	0.08 ± 0.01	0.08 ± 0.01
CMX-CMU	0.18 ± 0.02	0.18 ± 0.02	0.12 ± 0.02	0.12 ± 0.02
CMX-CMP	0.28 ± 0.02	0.27 ± 0.02	0.18 ± 0.02	0.18 ± 0.02
CMX-CMIO	0.35 ± 0.03	0.34 ± 0.03	0.24 ± 0.02	0.24 ± 0.02
$\mu\mu$	5.30 ± 0.01	5.10 ± 0.01	3.42 ± 0.01	3.42 ± 0.01
Total	23	20.8	17.3	17

Table D.1: Expected number of events breakdown for $t\bar{t}$, for each dilepton subcategory after each of the analysis cuts. The sample dataset ID is *ttopel*.

Category	ID+ISO	Conv+Cosm	metsig	OS
TCE-TCE	5.84 ± 0.03	5.05 ± 0.03	3.25 ± 0.02	3.25 ± 0.02
TCE-PHX	3.65 ± 0.02	3.39 ± 0.02	2.20 ± 0.02	1.97 ± 0.02
ee	9.49 ± 0.00	8.44 ± 0.00	5.45 ± 0.00	5.22 ± 0.00
Category	ID+ISO	Conv+Cosm	metsig	OS
TCE-CMUP	5.66 ± 0.03	5.22 ± 0.03	5.22 ± 0.03	5.22 ± 0.03
TCE-CMU	1.23 ± 0.01	1.12 ± 0.01	1.12 ± 0.01	1.12 ± 0.01
TCE-CMP	1.67 ± 0.02	1.54 ± 0.01	1.54 ± 0.01	1.54 ± 0.01
TCE-CMX	2.30 ± 0.02	2.11 ± 0.02	2.11 ± 0.02	2.11 ± 0.02
TCE-CMIO	1.71 ± 0.02	1.57 ± 0.02	1.57 ± 0.02	1.57 ± 0.02
PHX-CMUP	1.68 ± 0.02	1.67 ± 0.02	1.67 ± 0.02	1.50 ± 0.01
PHX-CMX	0.81 ± 0.01	0.81 ± 0.01	0.81 ± 0.01	0.71 ± 0.01
$e\mu$	15.06 ± 0.00	14.04 ± 0.00	14.04 ± 0.00	13.77 ± 0.00
Category	ID+ISO	Connv+Cosm	metsig	OS
CMUP-CMUP	1.50 ± 0.01	1.45 ± 0.01	0.93 ± 0.01	0.93 ± 0.01
CMUP-CMU	0.61 ± 0.01	0.60 ± 0.01	0.39 ± 0.01	0.39 ± 0.01
CMUP-CMP	0.84 ± 0.01	0.82 ± 0.01	0.52 ± 0.01	0.52 ± 0.01
CMUP-CMX	1.19 ± 0.01	1.17 ± 0.01	0.76 ± 0.01	0.76 ± 0.01
CMUP-CMIO	1.31 ± 0.01	1.28 ± 0.01	0.83 ± 0.01	0.83 ± 0.01
CMX-CMX	0.29 ± 0.01	0.28 ± 0.01	0.17 ± 0.00	0.17 ± 0.00
CMX-CMU	0.26 ± 0.01	0.25 ± 0.01	0.16 ± 0.00	0.16 ± 0.00
CMX-CMP	0.34 ± 0.01	0.33 ± 0.01	0.22 ± 0.01	0.22 ± 0.01
CMX-CMIO	0.61 ± 0.01	0.59 ± 0.01	0.39 ± 0.01	0.39 ± 0.01
$\mu\mu$	6.95 ± 0.00	6.78 ± 0.00	4.37 ± 0.00	4.37 ± 0.00
Total	31.5	29.3	23.9	23.4

Table D.2: Expected number of events breakdown for WW for each dilepton subcategory after each of the analysis cuts. The sample dataset id is *wewk5d*.

Category	ID+ISO	Conv+Cosm	metsig	OS
TCE-TCE	24.80 ± 0.40	20.35 ± 0.37	0.78 ± 0.07	0.76 ± 0.07
TCE-PHX	16.21 ± 0.33	14.67 ± 0.31	0.35 ± 0.05	0.29 ± 0.04
ee	41.01 ± 0.04	35.02 ± 0.04	1.13 ± 0.01	1.06 ± 0.01
Category	ID+ISO	Conv+Cosm	metsig	OS
TCE-CMUP	24.89 ± 0.41	22.06 ± 0.38	22.06 ± 0.38	22.04 ± 0.38
TCE-CMU	5.33 ± 0.19	4.79 ± 0.18	4.79 ± 0.18	4.78 ± 0.18
TCE-CMP	7.27 ± 0.22	6.47 ± 0.21	6.47 ± 0.21	6.47 ± 0.21
TCE-CMX	9.89 ± 0.26	8.78 ± 0.24	8.78 ± 0.24	8.77 ± 0.24
TCE-CMIO	7.47 ± 0.22	6.74 ± 0.21	6.74 ± 0.21	6.73 ± 0.21
PHX-CMUP	6.34 ± 0.20	6.21 ± 0.20	6.21 ± 0.20	5.47 ± 0.19
PHX-CMX	4.13 ± 0.17	4.06 ± 0.16	4.06 ± 0.16	3.58 ± 0.15
$e\mu$	65.32 ± 0.05	59.12 ± 0.05	59.12 ± 0.05	57.84 ± 0.05
Category	ID+ISO	Connv+Cosm	metsig	OS
CMUP-CMUP	6.04 ± 0.20	5.92 ± 0.20	0.18 ± 0.03	0.18 ± 0.03
CMUP-CMU	2.43 ± 0.13	2.35 ± 0.12	0.05 ± 0.02	0.05 ± 0.02
CMUP-CMP	3.54 ± 0.15	3.44 ± 0.15	0.07 ± 0.02	0.07 ± 0.02
CMUP-CMX	4.88 ± 0.18	4.77 ± 0.18	0.12 ± 0.03	0.12 ± 0.03
CMUP-CMIO	5.93 ± 0.20	5.74 ± 0.19	0.10 ± 0.03	0.09 ± 0.02
CMX-CMX	1.17 ± 0.09	1.14 ± 0.09	0.00 ± 0.00	0.00 ± 0.00
CMX-CMU	1.20 ± 0.09	1.17 ± 0.09	0.01 ± 0.01	0.01 ± 0.01
CMX-CMP	1.43 ± 0.10	1.39 ± 0.10	0.02 ± 0.01	0.02 ± 0.01
CMX-CMIO	2.22 ± 0.12	2.11 ± 0.12	0.07 ± 0.02	0.07 ± 0.02
$\mu\mu$	28.84 ± 0.03	28.05 ± 0.03	0.62 ± 0.00	0.61 ± 0.00
Total	135	122	60.9	59.5

Table D.3: Expected number of events breakdown for $Z \rightarrow \tau\tau$ for each dilepton subcategory after each analysis cut. The sample dataset ids are *ztop4i* and *ztop5i*, merged.

Category	ID+ISO	Conv+Cosm	metsig	OS
TCE-TCE	0.00 ± 0.00	0.00 ± 0.00	0.00 ± 0.00	0.00 ± 0.00
TCE-PHX	0.00 ± 0.00	0.00 ± 0.00	0.00 ± 0.00	0.00 ± 0.00
ee	0.00 ± 0.00	0.00 ± 0.00	0.00 ± 0.00	0.00 ± 0.00
Category	ID+ISO	Conv+Cosm	metsig	OS
TCE-CMUP	11.65 ± 0.83	2.14 ± 0.35	2.14 ± 0.35	1.94 ± 0.34
TCE-CMU	2.63 ± 0.39	0.34 ± 0.14	0.34 ± 0.14	0.29 ± 0.13
TCE-CMP	3.19 ± 0.43	0.89 ± 0.23	0.89 ± 0.23	0.89 ± 0.23
TCE-CMX	5.04 ± 0.54	1.03 ± 0.25	1.03 ± 0.25	0.87 ± 0.23
TCE-CMIO	2.89 ± 0.41	0.38 ± 0.15	0.38 ± 0.15	0.38 ± 0.15
PHX-CMUP	6.01 ± 0.59	5.97 ± 0.59	5.97 ± 0.59	3.04 ± 0.42
PHX-CMX	3.31 ± 0.44	3.26 ± 0.44	3.26 ± 0.44	1.83 ± 0.33
$e\mu$	34.71 ± 0.11	14.02 ± 0.07	14.02 ± 0.07	9.25 ± 0.06
Category	ID+ISO	Connv+Cosm	metsig	OS
CMUP-CMUP	1854.94 ± 10.38	1833.22 ± 10.32	1.84 ± 0.33	1.84 ± 0.33
CMUP-CMU	758.86 ± 6.66	750.34 ± 6.62	0.75 ± 0.21	0.75 ± 0.21
CMUP-CMP	982.83 ± 7.57	970.90 ± 7.53	1.49 ± 0.30	1.49 ± 0.30
CMUP-CMX	1655.95 ± 9.81	1632.86 ± 9.74	1.97 ± 0.34	1.97 ± 0.34
CMUP-CMIO	1928.92 ± 10.58	1901.39 ± 10.51	2.10 ± 0.35	2.10 ± 0.35
CMX-CMX	501.40 ± 5.42	493.36 ± 5.37	0.52 ± 0.17	0.52 ± 0.17
CMX-CMU	418.71 ± 4.95	413.17 ± 4.92	0.50 ± 0.17	0.50 ± 0.17
CMX-CMP	468.44 ± 5.23	462.27 ± 5.20	0.97 ± 0.24	0.97 ± 0.24
CMX-CMIO	832.29 ± 6.97	818.81 ± 6.91	1.46 ± 0.29	1.46 ± 0.29
$\mu\mu$	9402.35 ± 1.79	9276.34 ± 1.78	11.59 ± 0.06	11.59 ± 0.06
Total	$9.44e+03$	$9.29e+03$	25.6	20.8

Table D.4: Expected number of events breakdown for $Z \rightarrow \mu\mu$ for each dilepton subcategory after each analysis cut. The sample dataset id is *zewk6m*

Category	ID+ISO	Conv+Cosm	metsig	OS
TCE-TCE	7938.26 ± 21.48	6880.90 ± 20.06	10.46 ± 0.80	10.40 ± 0.79
TCE-PHX	7948.30 ± 21.50	7389.94 ± 20.76	5.84 ± 0.60	4.98 ± 0.55
ee	15886.56 ± 2.56	14270.84 ± 2.42	16.30 ± 0.08	15.38 ± 0.08
Category	ID+ISO	Conv+Cosm	metsig	OS
TCE-CMUP	0.10 ± 0.08	0.00 ± 0.00	0.00 ± 0.00	0.00 ± 0.00
TCE-CMU	0.00 ± 0.00	0.00 ± 0.00	0.00 ± 0.00	0.00 ± 0.00
TCE-CMP	0.00 ± 0.00	0.00 ± 0.00	0.00 ± 0.00	0.00 ± 0.00
TCE-CMX	0.00 ± 0.00	0.00 ± 0.00	0.00 ± 0.00	0.00 ± 0.00
TCE-CMIO	0.06 ± 0.06	0.00 ± 0.00	0.00 ± 0.00	0.00 ± 0.00
PHX-CMUP	0.00 ± 0.00	0.00 ± 0.00	0.00 ± 0.00	0.00 ± 0.00
PHX-CMX	0.00 ± 0.00	0.00 ± 0.00	0.00 ± 0.00	0.00 ± 0.00
$e\mu$	0.16 ± 0.01	0.00 ± 0.00	0.00 ± 0.00	0.00 ± 0.00
Category	ID+ISO	Connv+Cosm	metsig	OS
CMUP-CMUP	0.00 ± 0.00	0.00 ± 0.00	0.00 ± 0.00	0.00 ± 0.00
CMUP-CMU	0.00 ± 0.00	0.00 ± 0.00	0.00 ± 0.00	0.00 ± 0.00
CMUP-CMP	0.00 ± 0.00	0.00 ± 0.00	0.00 ± 0.00	0.00 ± 0.00
CMUP-CMX	0.00 ± 0.00	0.00 ± 0.00	0.00 ± 0.00	0.00 ± 0.00
CMUP-CMIO	0.00 ± 0.00	0.00 ± 0.00	0.00 ± 0.00	0.00 ± 0.00
CMX-CMX	0.00 ± 0.00	0.00 ± 0.00	0.00 ± 0.00	0.00 ± 0.00
CMX-CMU	0.00 ± 0.00	0.00 ± 0.00	0.00 ± 0.00	0.00 ± 0.00
CMX-CMP	0.00 ± 0.00	0.00 ± 0.00	0.00 ± 0.00	0.00 ± 0.00
CMX-CMIO	0.00 ± 0.00	0.00 ± 0.00	0.00 ± 0.00	0.00 ± 0.00
$\mu\mu$	0.00 ± 0.00	0.00 ± 0.00	0.00 ± 0.00	0.00 ± 0.00
Total	$1.59e+04$	$1.43e+04$	16.3	15.4

Table D.5: Expected number of events breakdown for $Z \rightarrow ee$ for each dilepton subcategory after each analysis cut. The sample dataset id is *zewk6d*

Category	ID+ISO	Conv+Cosm	metsig	OS
TCE-TCE	4.25 ± 0.12	3.58 ± 0.11	0.86 ± 0.05	0.72 ± 0.05
TCE-PHX	3.46 ± 0.11	3.19 ± 0.10	0.70 ± 0.05	0.54 ± 0.04
ee	7.71 ± 0.01	6.77 ± 0.01	1.56 ± 0.01	1.26 ± 0.01
Category	ID+ISO	Conv+Cosm	metsig	OS
TCE-CMUP	0.53 ± 0.04	0.46 ± 0.04	0.46 ± 0.04	0.27 ± 0.03
TCE-CMU	0.10 ± 0.02	0.09 ± 0.02	0.09 ± 0.02	0.05 ± 0.01
TCE-CMP	0.14 ± 0.02	0.12 ± 0.02	0.12 ± 0.02	0.06 ± 0.01
TCE-CMX	0.25 ± 0.03	0.21 ± 0.03	0.21 ± 0.03	0.10 ± 0.02
TCE-CMIO	0.17 ± 0.02	0.17 ± 0.02	0.17 ± 0.02	0.08 ± 0.02
PHX-CMUP	0.23 ± 0.03	0.22 ± 0.03	0.22 ± 0.03	0.08 ± 0.02
PHX-CMX	0.12 ± 0.02	0.12 ± 0.02	0.12 ± 0.02	0.06 ± 0.01
$e\mu$	1.53 ± 0.01	1.40 ± 0.01	1.40 ± 0.01	0.70 ± 0.00
Category	ID+ISO	Connv+Cosm	metsig	OS
CMUP-CMUP	1.10 ± 0.06	1.08 ± 0.06	0.25 ± 0.03	0.22 ± 0.03
CMUP-CMU	0.46 ± 0.04	0.45 ± 0.04	0.13 ± 0.02	0.12 ± 0.02
CMUP-CMP	0.63 ± 0.05	0.62 ± 0.05	0.15 ± 0.02	0.12 ± 0.02
CMUP-CMX	0.87 ± 0.05	0.85 ± 0.05	0.19 ± 0.03	0.16 ± 0.02
CMUP-CMIO	1.12 ± 0.06	1.08 ± 0.06	0.27 ± 0.03	0.23 ± 0.03
CMX-CMX	0.20 ± 0.03	0.19 ± 0.03	0.06 ± 0.01	0.06 ± 0.01
CMX-CMU	0.19 ± 0.03	0.19 ± 0.03	0.05 ± 0.01	0.04 ± 0.01
CMX-CMP	0.27 ± 0.03	0.27 ± 0.03	0.08 ± 0.02	0.06 ± 0.01
CMX-CMIO	0.49 ± 0.04	0.48 ± 0.04	0.14 ± 0.02	0.11 ± 0.02
$\mu\mu$	5.34 ± 0.01	5.20 ± 0.01	1.32 ± 0.01	1.11 ± 0.00
Total	14.6	13.4	4.28	3.07

Table D.6: Expected number of events breakdown for WZ for each dilepton subcategory after each analysis cut. The sample dataset id is *wtop1z*

Category	ID+ISO	Conv+Cosm	metsig	OS
TCE-TCE	1.95 ± 0.05	1.63 ± 0.05	0.30 ± 0.02	0.29 ± 0.02
TCE-PHX	1.31 ± 0.04	1.21 ± 0.04	0.19 ± 0.02	0.17 ± 0.01
ee	3.26 ± 0.01	2.84 ± 0.00	0.49 ± 0.00	0.47 ± 0.00
Category	ID+ISO	Conv+Cosm	metsig	OS
TCE-CMUP	0.09 ± 0.01	0.07 ± 0.01	0.07 ± 0.01	0.04 ± 0.01
TCE-CMU	0.01 ± 0.00	0.01 ± 0.00	0.01 ± 0.00	0.01 ± 0.00
TCE-CMP	0.01 ± 0.00	0.01 ± 0.00	0.01 ± 0.00	0.01 ± 0.00
TCE-CMX	0.03 ± 0.01	0.02 ± 0.01	0.02 ± 0.01	0.01 ± 0.00
TCE-CMIO	0.02 ± 0.00	0.01 ± 0.00	0.01 ± 0.00	0.00 ± 0.00
PHX-CMUP	0.02 ± 0.00	0.01 ± 0.00	0.01 ± 0.00	0.00 ± 0.00
PHX-CMX	0.01 ± 0.00	0.01 ± 0.00	0.01 ± 0.00	0.00 ± 0.00
$e\mu$	0.19 ± 0.00	0.13 ± 0.00	0.13 ± 0.00	0.07 ± 0.00
Category	ID+ISO	Connv+Cosm	metsig	OS
CMUP-CMUP	0.51 ± 0.03	0.47 ± 0.02	0.09 ± 0.01	0.09 ± 0.01
CMUP-CMU	0.21 ± 0.02	0.20 ± 0.02	0.05 ± 0.01	0.04 ± 0.01
CMUP-CMP	0.29 ± 0.02	0.28 ± 0.02	0.05 ± 0.01	0.05 ± 0.01
CMUP-CMX	0.37 ± 0.02	0.35 ± 0.02	0.07 ± 0.01	0.07 ± 0.01
CMUP-CMIO	0.48 ± 0.02	0.46 ± 0.02	0.07 ± 0.01	0.07 ± 0.01
CMX-CMX	0.12 ± 0.01	0.10 ± 0.01	0.02 ± 0.00	0.02 ± 0.00
CMX-CMU	0.09 ± 0.01	0.09 ± 0.01	0.02 ± 0.00	0.01 ± 0.00
CMX-CMP	0.12 ± 0.01	0.11 ± 0.01	0.03 ± 0.01	0.02 ± 0.01
CMX-CMIO	0.20 ± 0.02	0.19 ± 0.02	0.04 ± 0.01	0.04 ± 0.01
$\mu\mu$	2.39 ± 0.00	2.25 ± 0.00	0.43 ± 0.00	0.42 ± 0.00
Total	5.84	5.22	1.06	0.956

Table D.7: Expected number of events breakdown for ZZ for each dilepton subcategory after each analysis cut. The sample dataset id is *ztopcz*

Bibliography

[1] F. Abe et al. (The CDF Collaboration). Measurement of the top quark mass and t anti-t production cross-section from dilepton events at the collider detector at fermilab. *Phys. Rev. Lett.*, 80:2779, 1998.

[2] R. M. Barnett and L. J. Hall. Squarks in tevatron dilepton events?. hep-ph/:9609313.

[3] D. Acosta et al. (CDF Collaboration). Measurement of the t anti-t producitons cross section in p anti-p collisions at s**(1/2)=1.96-tev using dilepton events. *Phys. Rev. Lett.*, 93:142001, 2004.

[4] D. Acosta et al. (CDF Collaboration). Measurement of the w+w- production cross section in p anti-p collisions at s**(1/2)=1.96 tev using dilepton events. *Phys. Rev. Lett,*, 94:211801, 2005.

[5] S. F. Novaes. Standard model: An introduction. hep-ph/:0001283.

[6] J. C. Maxwell. *A Treatsie on Electricity and Magnetism*. Clarendon Press, Oxford, 1865.

[7] A. Salam J. Goldstone and S. Weinberg. Broken symmetries. *Phys. Rev.*, 127:965, 1962.

[8] P. A. M. Dirac. *Proc. R. Soc.*, A112:661, 1926.

[9] P. A. M. Dirac. The quantum theory of electrons. *Proc. R. Soc.*, A117:610, 1928.

[10] J. J. Thompson. Cathode rays. *Phil. Mag.*, 44:293, 1897.

[11] J. J. Thompson. On the masses of the ions in gases at low pressures. *Phil. Mag.*, 48:295, 1899.

[12] C. D. Anderson. The positive electron. *Phys. Rev.*, 43:491, 1933.

[13] S. H. Neddermeyer and C. D. Anderson. Note on the nature of cosmic-ray particles. *Phys. Rev.*, 51:884, 1937.

[14] H. Yukawa. On the interaction of elementary particles. *Proc. Phys. Math. Soc. Jap.*, 17:48, 1935.

[15] G.P.S.Occhialini C.M.G.Lattes, H.Muirhead and C.F.Powell. Processes involving charged mesons. *Nature*, 159:694, 1947.

[16] S. Eidelman et al. The review of particle physics. *Physics Letters.*, B592:1, 2004.

[17] M. L. Perl et al. Evidence for anomalous lepton production in e+e- annihilation. *Phys. Rev. Lett.*, 35:1489, 1975.

[18] E. Fermi. An attempt of a theory of beta radiation. *Z. Phys*, 88:161, 1934.

[19] Y. Fukuda et al. (Super-Kamiokande Collaboration). Evidence for oscilation of atmospheric neutrinos. *Phys. Rev. Lett.*, 81:1562, 1998.

[20] M. Gell-Mann. A schematic model of baryons and mesons. *Phys. Lett.*, 8:214, 1964.

[21] M. Kobayashi and K. Maskawa. Cp violation in the renormalizable theory of weak interaction. *Prog. Theor. Phys*, 49:652, 1973.

[22] G. S. Abrams et al. The discovery of a second narrow resonance in e+e- anihilation. *Phys. Rev. Lett.*, 33:1453, 1974.

[23] S. W. Herb et al. Observation of a dimuon resonance at 9.5-gev in 400-gev proton-nucleus collisions. *Phys. Rev. Lett.*, 39:252, 1977.

[24] F. Abe et al. (CDF Collaboration). Observation of top quark production in anti-p p collisions. *Phys. Rev. Lett.*, 74:2626, 1995.

[25] S. Abachi et al. (D0 Collaboration). Observation of the top quark. *Phys. Rev. Lett.*, 74:2632, 1995.

[26] O. Greenberg and C. Nelson. Color models of hadrons. *Phys. Rept.*, 32:69, 1977.

[27] G. Arnison et al. (UA1 Collaboration). Experimental observation of isolated large transverse energy electrons with associated missing energy at s**(1/2)=540 gev. *Phys. Lett.*, B122:103, 1983.

[28] H. Politzer. Asymptotic freedom: An approach to strong interactions. *Phys. Rept.*, 14:129, 1974.

[29] B. Anderson et al. Parton fragmentation and string dynamics. *Phys. Rep.*, 97:31, 1983.

[30] E. Noether. Invariante varlationsprobleme. *Nachr. v. d. Ges. d. Wiss. zu Gottingen*, S:235, 1918.

[31] R. Feynman. Mathematical formulation of the quantum theory of electromagnetic interaction. *Phys. Rev.*, 80:440, 1950.

[32] N. Cabbibo. *Phys. Rev. Lett.*, 10:531, 1950.

[33] R. P. Feynman. Very high-energy collisions of hadrons. *Phys. Rev. Lett.*, 23:1415, 1969.

[34] Jon Pumplin et al. Parton distributions and the strong coupling: Cteq6ab pdfs. hep-ph/:0512167.

[35] D0 Collaboration CDF Collaboration and Tevatron Ewk. Working Group. Combination of cdf and d0 results on the top-quark mass. hep-ex/:0404010.

[36] N Kidonakis and R. Vogt. Next-to-next-to-leading order soft gluon corrections in top quark hadroproduction. *Phys. Rev.*, D68:114014, 2003.

[37] I. Bigi et al. Production and decay properties of ultra-heavy quarks. *Phys. Lett.*, B181:157, 1986.

[38] R. K. Ellis J. M. Campbell. An update on vector boson pair production at hadron colliders. *Phys. Rev.*, D60:113006, 1999.

[39] W. L. Van Neerved R. Hamberg and T. Matsuura. A complete calculation of the order alpha**2 correction to the drell-yan k-factor. *Nucl. Phys.*, B359:343, 1991.

[40] F. Abe et al. (The CDF Collaboration). Measurement of the t anti-t production cross-section in p anti-p collisions at s**(1/2) = 1.8-tev. *Phys. Rev. Lett.*, 80:2773, 1998.

[41] D. Acosta et al. (CDF Collaboration). Measurement of the t anti-t producitons cross section in p anti-p collisions at s**(1/2)=1.96-tev using lepton + jets events with secondary vertex b-tagging. *Phys. Rev.*, D71:052003, 2005.

[42] V. M. Abazov et al. (D0 Collaboration). Measurement of the t anti-t production cross section in p anti-p collistions at s**(1/2) = 1.96-tev in dilepton final states. *Phys. Lett.*, B626:55, 2005.

[43] V. M. Abazov et al. (D0 Collaboration). Measurement of the t anti-t production cross section in p anti-p collisions at s**(1/2) = 1.96-tev using lepton + jets events with lifetime b-tagging. *Phys. Lett.*, B626:35, 2005.

[44] V. M. Abazov et al. (D0 Collaboration). Measurement of the ww production cross section in p anti-p collisions at s**(1/2) = 1.96-tev. *Phys. Rev. Lett.*, 94:151801, 2005.

[45] S. Baroiant et al. Measurement of the t anti-t production cross section in p anti-p collisions at s**(1/2) = 1.96-tev using lepton + jets events with lifetime b-tagging. *CDF Internal Note*, 8132:1, 2006.

[46] C. H. O. behalf of the CDF Collaboration. Operational experiance and performance of the cdfii silicon detector. *Nucl. Instrum. Metch.*, 530:1, 2004.

[47] D. A. et al. The cdf intermediate silicon detector at cdfii: Design and progress. *Nucl. Instrum. Metch.*, 435:44, 1999.

[48] T. A. et al. Cdf central outer tracker. *Nucl. Instrum. Metch.*, A267:301, 1988.

[49] L. B. et al. Cdf central electromagnetic calorimenter. *Nucl. Instrum. Metch.*, A267:272, 1988.

[50] L. B. et al. Cdf central hadronic calorimenter. *Nucl. Instrum. Metch.*, A526:249, 2004.

[51] A. A. et al. Cdf central muon detector. *Prog. Part. Nucl. Phys.*, 114:25, 2002.

[52] S. Mrenna T. Sjostrand and P. Skands. Pythia 6.4 physics and manual. hep-ph/:063175.

[53] G. Corcella et al. Herwig 6.5. hep-ph/:0210213.

[54] Geant 4. *Nuclear Instruments and Methods in Physics Research*, A(506):250, 2003.

[55] Joint physics meeting high-pt lepton id. *http://www-cdf.fnal.gov/internal /physics/joint_physics/index.html.*

[56] V. Martin. High-pt muon id cuts and efficiencies for use with 5.3.1 data and 5.3.3 mc. *CDF Internal Note*, 7367:1, 2005.

[57] D. Glenzinski et al. Results from the top dilepton analysis of the tight lepton and isolated track sample. *CDF Internal Note*, 6562:1, 2003.

[58] M. Coca et al. A measurement of the $t\bar{t}$ cross-section using dileptons. *CDF Internal Note*, 6830:1, 2003.

[59] S. Carron et al. Ww production in the dilepton channel with $200\,\mathrm{pb}^{-1}$. *CDF Internal Note*, 6909:1, 2003.

[60] D. Glenzinski et al. Ww cross section measurement in the tight lepton and isolated track sample. *CDF Internal Note*, 6872:1, 2004.

[61] F. Abe et al. (CDF Collaboration). *Phys. Rev. Lett.*, (78):4536, 1997.

[62] C.Mills C.Hill, J.Incandela. Electron identification in offline release 5.3. *CDF Internal Note*, 7309:1, 2004.

[63] J. Nielsen Y. Ishizawa. Trigger efficiencies for high et electron. *CDF Internal Note*, 7401:1, 2004.

[64] J-F Arguin et al. Systematic uncertainties associated with jet corrections for winter 2003 conferences. *CDF Internal Note*, 6419:1, 2003.

[65] U. Yang Y.K. Kim. Initial state gluon radiation studies on drell-yan data for top-pair production in hadron collider. *CDF Internal Note*, 6804:1, 2004.

[66] J. Boudreau et al. Systematic studies on lifetimes of b mesons using the exclusive jpsi decay modes. *CDF Internal Note*, 7796:1, 2005.

[67] C. Blocker. Maximum likelihood primer. *CDF Internal Note*, 6507:1, 2003.

[68] Minuit reference manual, version 94.1. *http://wwwasdoc.web.cern.ch/wwwasdoc /WWW/minuit/minmain/minmain.html.*

[69] S. Carron et al. A global analysis of the high-p_t dilepton sample using 200 pb^{-1} of run 2 data. *CDF Internal Note*, 6870:1, 2004.

[70] D. Amidei et al. Measurements of sigma* b(w→enu), sigma * b(z→ee) and the ratio r using cdf run ii data. *CDF Internal Note*, 6681:1, 2004.

[71] D. Zeppenfeld K. Hagiwara, R. D. Peccei and K. Hikasa. Probing the weak boson sector in e+e- to w+w-. *Nucl. Phys.*, B282:253, 1987.

Biography

The author attended the Universidade de Sao Paulo in Brazil and graduated with a Bachelors Degree in Physics; Licenciatura em Fisica, in 1997. He came to Duke University in the Fall of 1999 and began graduate studies in Phyisics, recieved a Masters degree from Duke University in 2004. He pursued his graduate research in Physics under the direction of Professor Mark Kruse.